ACOUSTIC WAVE BIOSENSORS FOR BIOMECHANICAL AND BIOLOGICAL CHARACTERIZATION OF CELLS

by

Huiyan Wu

B.E., Xi'an Jiaotong University, P. R. China, 2008

M.E., Xi'an Jiaotong University, P. R. China, 2011

Submitted to the Graduate Faculty of

Swanson School of Engineering in partial fulfillment

of the requirements for the degree of

Doctor of Philosophy

University of Pittsburgh

2017

UNIVERSITY OF PITTSBURGH

SWANSON SCHOOL OF ENGINEERING

This dissertation was presented

by

Huiyan Wu

It was defended on

June 22, 2017

and approved by

Dissertation Co-Advisor: James H.-C. Wang, Ph.D., Professor,

Departments of Orthopaedic Surgery & Mechanical Engineering and Materials Science

William S. Slaughter, Ph.D., Associate Professor,

Department of Mechanical Engineering and Materials Science

Patrick Smolinski, Ph.D., Associate Professor,

Department of Mechanical Engineering and Materials Science

Dissertation Advisor: Qing-Ming Wang, Ph.D., Professor,

Department of Mechanical Engineering and Materials Science

ACOUSTIC WAVE BIOSENSORS FOR BIOMECHANICAL AND BIOLOGICAL CHARACTERIZATION OF CELLS

Huiyan Wu, PhD

University of Pittsburgh, 2017

During past decades, interest in development of cell-based biosensors has increased considerably. In this study, two kinds of acoustic wave sensors are adopted as the cell-based biosensors to investigate the biomechanical and biological behaviors of cells, the quartz thickness shear mode (TSM) resonator and Love wave sensor. For the first part, the quartz TSM resonator is applied to detect the structural and mechanical properties of tendon stem/progenitor cells (TSCs), which are one kind of newly discovered adult cells in tendons, and the platelets from blood. Through the TSM resonator, the related viscoelastic properties of cells are extracted, which could indicate the state of cells in different physiological conditions. The TSM resonator sensor is utilized to characterize the aging-related viscoelasticity differences between the aging and young TSCs, and also to monitor the dynamic activation process of platelets. For the second part, a 36° *YX*-$LiTaO_3$ Love wave sensor with a parylene-C wave guiding layer is proposed as a cell-based biosensor. A theoretical model is derived, to describe the Love wave propagation in the wave guiding layer, the adherent cell layer, and penetration into the liquid medium. The Love wave sensor is used to monitor the adhesion process of cells. Compared with TSM resonator, the response of Love wave sensor to the cell adhesion is primarily induced by the formation of bonds between cells and the substrate. The numerical results indicate that the adherent cell layer of

various storage or loss shear modulus in certain range can cause evident, characteristic variations in propagation velocity and propagation loss, revealing the potential of Love wave sensors in providing useful quantitative measures on cellular mechanical properties. In addition, a Love wave sensor with a phononic wave guiding layer is introduced for non-operation signal filtering and sensor sensitivity improvement. Both two kinds of acoustic wave sensors present their own advantages as the cell-based biosensors, indicating advisable techniques for investigating cell biology in general and certain physiological processes in particular.

TABLE OF CONTENTS

LIST OF TABLES

LIST OF FIGURES

LIST OF ABBREVIATIONS

AFM	Atomic Force Microscopy
BAW	Bulk Acoustic Wave
BVK	Butterworth-Van Dyke
ECIS	Electric Cell-Substrate Impedance Sensor
ECM	Extracellular Matrix
FWHM	Full Width at Half Maximum
IDT	Interdigital Transducer
MBM	Magnetic Bead Microrheometry
PBS	Phosphate-Buffered Saline
PPP	Platelet-Poor Plasma
PRP	Platelet-Rich Plasma
PDMS	Poly(dimethylsiloxane)
PMMA	Ploy(methyl methacrylate)
QCM	Quartz Crystal Microbalance
QCM-D	Quartz Crystal Microbalance with Dissipation Monitoring
SAW	Surface Acoustic Wave
SEM	Scanning Electronic Microscopy
SH-SAW	Shear-Horizontal Surface Acoustic Wave

SPR	Surface Plasmon Resonance
TEG	Thromboelastography
TLM	Transmission Line Model
TSC	Tendon Stem Cell
TSM	Thickness Shear Mode
UV	Ultraviolet

LIST OF SYMBOLS

$\boldsymbol{T}$	Stress Tensor
$\boldsymbol{S}$	Surface Acoustic Wave
$\boldsymbol{c}$	Elastic Stiffness Constant Tensor
$\boldsymbol{E}$	Electric Field Vector
$\boldsymbol{D}$	Electrical Displacement Vector
$\boldsymbol{\varepsilon}$	Permittivity Constant Tensor
$\boldsymbol{\beta}$	Reciprocal Permittivity Constant Tensor
$\boldsymbol{e}$, $\boldsymbol{h}$, $\boldsymbol{d}$, $\boldsymbol{g}$	Piezoelectric Constant Tensor
$\boldsymbol{u}$	Particle Displacement Vector
$\boldsymbol{v}$	Particle Velocity Vector
ρ	Density
ω	Angular Frequency
v	Phase Velocity
k	Wave Number
K	Electromechanical Coupling Coefficient
Q	Mechanical Quality Factor
E	Young's Modulus (Elastic Modulus)
G	Shear Modulus

V	Electric Potential
I	Electric Current
Z	Electric Impedance
Y	Electric Admittance
F	Elastic Force
A	Contact Area

PREFACE

I wish to take this opportunity to thank everyone who has provided me immense help during the course of my graduate study in the Department of Mechanical Engineering & Materials Science at University of Pittsburgh.

First and foremost, I would like to thank my advisers, Dr. Qing-Ming Wang and Dr. James H.-C. Wang, for offering me such a great multidisciplinary project and unique training in the fields of mechanical engineering and cell mechano-biology. They always supported my academic work by closely following my research progress. It was really a fruitful experience to work under their eminent professional guidance. I would like to thank my other distinguished committee members, Dr. William S. Slaughter and Dr. Patrick Smolinski, for their support, comments and suggestions as committee members. I also would like to thank Dr. Minking K. Chyu and Dr. Jeffrey S. Vipperman for their support and advising in my job searches.

I am very grateful to my collaborators, Dr. Fang Li, Dr. Lifeng Qin, Dr. Yizhong Wang, Dr. Hongfei Zu, Qiuyan Li, Zheng Min, Mohammad Gudarzi, Yingying Sun, Wenbin Luo, Rongjie Liang, Xuande Zhang, Shijing Luo in Microsensor and Microactuator Laboratory, and Dr. Jianying Zhang, Dr. Ting Yuan, Dr. Yiqin Zhou, Dr. Daibang Nie, Dr. Jinsong Yang, Dr. Chunyue Ma, Dr. Biao Chen, Dr. Guangyi Zhao in Mechanobiology Laboratory, for providing me so much help in my research work. I would like to specially mention the help and support of Dr. Hongfei Zu and Dr. Guangyi Zhao, who provided not only professional suggestions in my

research, but also emotional support in my life. I would like to thank Matthew France, Dr. Susheng Tan from Nanoscale Fabrication and Characterization Facility, Cole Van Ormer from Department of Mechanical Engineering and Materials Science, and Dr. Lawrence A. Vernetti from Drug Discovery Institute, for their help with my experiments for my research project. In addition, I would like to express my gratitude to Dr. Xiaotian Li from Wuhan University, who has given me tremendous academic help since her visit at the University of Pittsburgh, and who has become one of my best friends. I am also grateful to Dr. Xiangming Xiong from University of Shenzhen for his professional advising in my theoretical research.

I have befriended many during my graduate study in Pittsburgh and I would like to thank them for their wonderful, unfailing friendship.

Finally, I would like to thank my parents, parents in law and my husband Zhiyuan, for all the joy and courage they brought to me. I am extremely grateful to my dear little daughter Emma, who is the best thing that ever happened to me.

Many thanks!

1.0 INTRODUCTION

A sensor is essentially considered as a transducer that can provide an output signal in response to some input quantities [1]. Fig. 1 schematically presents the basic structure of a sensor. The output signal is usually electrical, for example, a series of digital voltage pulses, an analog voltage or current, or an oscillation voltage or current with specific frequency. The input quantities on the other hand can be a variety of characteristic parameters of an object or surrounding environment. They can be physical (velocity, acceleration, temperature, etc.), chemical (pH, toxicity, catalytic property, etc.) and biological (viability, senescence, stemness, etc.). In general a circuitry is connected with a sensor, and even sometimes is integrated as a part of it. What a sensor does is to transduce various input quantities into intermediate signals (acoustic, optical, electrical, etc.), and then these intermediate signals are converted into an electrical signal through signal processing and controlling circuits. Attributed to the development of sensors, a series of complicated measurement can be conducted in an easy, direct way, providing a great convenience to our normal life. For example, with a gas sensor attached to the outlet of exhaust pipe, the hazard NO_x gas in waste gas of a vehicle is detected before emission. And, with a temperature sensor mounted in a high-temperature furnace, heating/cooling state is monitored *in-situ*. Sensors have been widely applied in many different fields, such as robotics, automobiles, energy and power, aerospace and aeronautics. Sensors in robotics can be used as a signal receptor to detect the obstacle within a certain distance away, assisting the robotic move

around the obstacle, or to detect the distance between the robotic and the target object, directing the robotic to adjust the moving direction to grab the object successfully. When we drive a car, the tire pressure sensor can tell us if the tire pressure is good or not, and the fuel sensor can tell if there is any need to go to a gasoline station. Also, there are many extreme cases in power plant and aeronautics industry, like high pressure or high temperature, and sensors which can be functional in the harsh conditions are required.

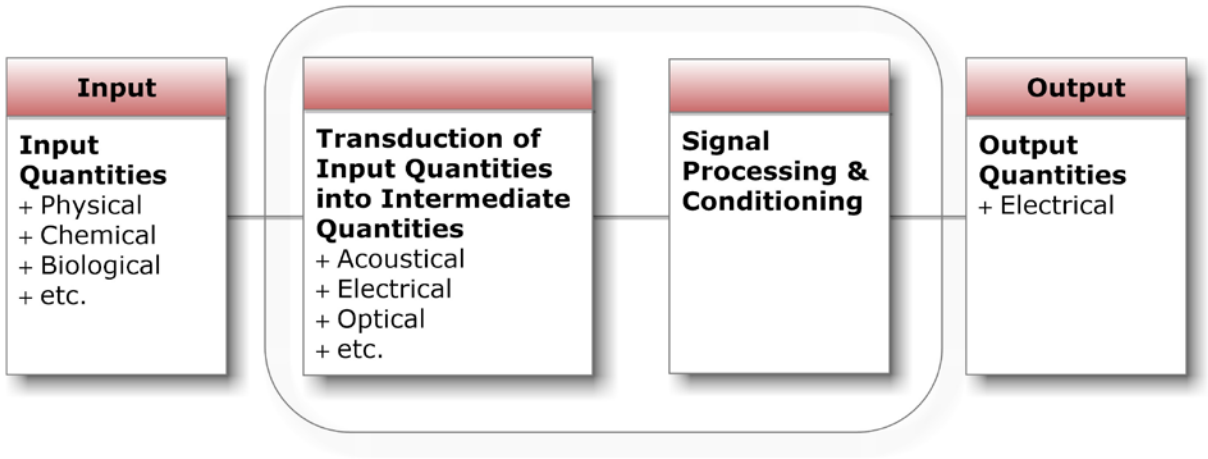

Figure 1. Schematic diagram of a sensor that produces an electrical output in response to an input quantity

A sensor can be characterized by a variety of parameters: range, resolution/threshold, sensitivity, selectivity, stability, linearity, durability and so on. Resolution is a measure of the magnitude change of an input quantity that induce one unit variation in output signal, which in other words provides the detectable minimum change of an input quantity. Sensitivity of a sensor is a measure of the magnitude of output electrical signal in response to an input quantity of given magnitude. Depending on different input quantities, the units for both sensitivity and resolution are varied. Besides, if a sensor is applied to distinguish one input quantity from another,

selectivity is proposed to characterize the degree in which it can complete an unambiguous measurement of the specific input quantity. When a sensor is used in harsh environment, as mentioned above, its functional stability under varied pressure or temperature should be evaluated. In fact, under different circumstances, these criteria are emphasized in different degrees, and some others might be adopted, such as repeatability and reversibility. All these relevant parameters provide an explicit, straightforward way to evaluate the performance of sensors in service condition.

1.1 MOTIVATIONS AND OBJECTIVES

During the past decades, there is an extraordinary growth in research on sensors in general and on biosensors in particular. The miniaturization, low cost and essentially real-time measurements in a variety of biological and biomedical applications has generated intense commercial interest. The multidisciplinary expertise underpins successful research and development in biosensors. Such life sciences as pharmacology, immunology, genetic engineering and protein chemistry are involved; and from the physical sciences side, mechanical vibration, materials science, nanotechnology, electronics, and so on [2]. The magnitude of the research effort in biosensors is also a reflection of the diverse applications and types of biosensors.

1.1.1 Cell-based Biosensors

The general definition of “biosensor” includes two parts: (1) The detected object is a biological element (tissue, cell, enzyme, etc.), biologically derived material or biomimetic component. In

other words, the input quantities contain some biological information; (2) The sensing part is a biological element, biologically derived material or biomimetic component, leading to an interaction between the detected object and biological sensing part during measurement process. In this case, as the primary transducer, the biological sensing part is usually connected with a secondary transducer, an acoustic, optical or electrical sensor. A sensor with either of the above two characteristics can be called as a biosensor. Sometimes, both of these two characteristics are included in one sensor, leading to an unnecessary to distinguish one from the other. For example, a surface plasmon resonator coated with antibody HC10 was applied to detect influenza virus [3]. In this case, both detected object and sensing part are biological elements. Thus, in following sessions, if no particular need sensors with either of these two characteristics will be called as biosensors uniformly.

Based on this, the definition of cell-based biosensor is quite evident. The significant feature of cell-based biosensor is to use living cells as the detected objects or receptors to other stimulus from the surrounding environment [4]. In the latter case, living cells as the first transducer are usually connected with the secondary transducer, converting physiological signals to electrical signals. It is known that every organism either consists of cells or itself is a single cell, whether it is an animal, a plant or a microorganism [5]. As a basic unit of living organisms, cells from different species, even from identical specie can possess their own characteristics, ranging from morphology, architecture to physiological function and reaction. The demand for specific functions can be suggested by cellular morphology and intrinsic structure, which leads to desirable optimization of the corresponding properties of cells. Thus, to observe and understand cell behaviors plays an important role in both biological and biomedical fields, no matter for cells themselves or interactions between cells and other surrounding stimulus. A variety of

sensors have been applied as cell-based biosensors, and in particular, some of them have been proven a great success and put into commercial production. Depending on types of intermediate signals, these biosensors can be classified into acoustic, optical or some other kinds. The nature of intermediate signals determines the corresponding properties of cells which are extracted or monitored by cell-based biosensors. An acoustic biosensor can detect mass or mechanical property variations during cell activities, when an optical or electrical impedance biosensor focuses on changes of fluorescence type, intensity or resistance, capacitance of cells. Using cell-based biosensors, a series of cell activities can be traced, including cell proliferation, migration, and differentiation and so on. Meanwhile, with cells as a sensing element, the basic physiological reactions to different external stimulus are observed, which would be widely applied in drug development, quality control and environment monitoring.

Different from other industrial sensors, cell-based biosensors need to support living cells as a part of itself, which leads to a natural environmental condition required by alive cells [4]. The related physical and chemical parameters of service condition should be controlled strictly, including 37ºC, 5% CO_2 and nutrition supply, and so the normal metabolism of living cells can be maintained for a long period. Furthermore, it is an essential part to seed and culture cells on the sensor surface. For most industrial sensors, the substrate is made of metals or ceramics, but not glass or polymeric plastic as a slide or petri dish. Living cells should be immobilized around the surface without any limitations on their biological functions, thus providing comparable references for their reactions in real natural environments. So, relevant evaluations on cells are necessary before and after cell-based biosensor measurements, such as viability and stemness.

So far, due to their high sensitivity, excellent selectivity, rapid response and flexible applicability, interest in research and development of cell-based biosensors has increased

considerably. Cell-based biosensors have been used not only in fundamental biological and biomedical studies, but also in many other related application fields, such as toxicity testing, contamination testing, pharmaceutical screening and environmental monitoring. Currently, a series of sensors have been developed as cell-based biosensors, including the thickness shear mode (TSM) resonator (also called as quartz crystal microbalance, QCM), surface plasmon resonance (SPR), light addressable potentiometric sensor (LAPS), microelectrodes array (MEA), field-effect transistor (FET) and electric cell-substrate impedance sensor (ECIS) [4]. Most of them (MEA, FET and ECIS) are based on electrical properties of cells with varied circuit design. The TSM resonator or QCM is a well-known acoustic wave sensor, when SPR and LAPS are based on optical techniques.

1.1.2 Cell-based Acoustic Wave Biosensors

As discussed above, the cell is the basic component unit of every organism. Cells exist in a wide variety of shapes and sizes and in a vast diversity of cellular functions as well [5]. For example, cells distributed in muscle tissue or tendon tissue need be subject to frequent mechanical stress. This tension-bearing role asks for an improved mechanical property of cells, resulting in an elongated shape for both myocytes and tenocytes. Cells require appropriate structural and mechanical properties when playing certain functions. In this case, quantitative measurement of cellular mechanical properties provides advantages in evaluating their functions in complex environment. Although these cellular performance indicators are relatively stable in a normal physiological state, significant changes might occur in them when previous equilibrium is disrupted, such as PH change, oxygen concentration reduction or environmental temperature increase. For example, it is reported that cancer cells presented quite different biomechanical

properties compared with normal ones, such as stiffness or viscoelasticity [6]. For some certain kinds of cells, like the tendon or muscle cells, their primary function is to bear the external mechanical loading. Thus, structural and mechanical properties of cells can be considered as a useful biophysical marker to indicate the cellular biomechanical status in cell activities.

By far, a series of measurement methods have been developed for detection of cellular mechanical properties, from conventional mechanical methods such as atomic force microscopy (AFM) [7-10] and microplate manipulation [11-13], to some biomechanics techniques such as thromboelastography (TEG) [14-16] and magnetic bead microrheometry (MBM) [17-19]. Most of them (except TEG) need to apply an external force on individual cell in an invasive manner. For MBM, the diameter of ferrimagnetic microbead is approximately 1~5 μm, while the normal radius of AFM probe is even under 1 μm. As a result, it is difficult for these methods to present statistical results, although local measurement can be conducted on some specific parts of cells. TEG on the other hand is specifically used to measure platelet contribution during coagulation process. In addition, measurement process of these methods is time-consuming, and cannot be conducted *in-situ*. As discussed in previous session, an acoustic wave biosensor can detect mass or mechanical property variations of cells during a series of physiological processes. Due to its intrinsic non-invasive, real-time, long-time stable and easy connectable features, cell-based acoustic wave biosensor possesses considerable advantages compared with other measurements.

As the most widely used acoustic wave sensor, TSM resonator or QCM consists of a thin disk of AT-cut quartz with circular Au or Pt electrodes deposited on both sides, which can be electrically excited in a number of resonant thickness-shear modes. When its surface loading condition varies, for example cell monolayer adhering on the surface, the electrically excited acoustic wave propagation can change accordingly through entire quartz crystal, allowing a

simple, quantitative and non-invasive method to extract the complex shear modulus of the attached cells. Currently, TSM resonator has been applied as a cell-based biosensor in some studies on different types of cells [4, 20-26]. However, in most cases the applications are only based on mass changes on the electrode surface, indicating its high sensitivity over a wide detection range from small molecules to complex arrays of cells bound to the surface. Recently, as development of quartz crystal microbalance with dissipation monitoring (QCM-D), both resonance frequency f and dissipation D can be acquired at the same time, providing a strong tool to monitor complicated cell behaviors [27-30]. Nevertheless, interpretations to specific variations in f and D are still lacking, leading to an ambiguous relation between cell behaviors and the corresponding sensor electrical response. TSM resonator has been studied for characterization of viscoelastic properties of a thin soft layer coated on its surface [31-34]. Based on this model, an explicit relation between cellular states and electrical response can be established via characterization of cellular viscoelastic properties. TSM resonator is proven an advisable and reliable tool to extract the viscoelasticity of cells as a biophysical marker, which is the first part of research work in this study.

More recently, the Love wave sensor is considered as one of the most promising probing methods in both fundamental biology and biomedical engineering, detecting behaviors of cells on their surface in an easy, non-invasive, and quantitative manner [1, 35-41]. The shear-horizontal surface acoustic waves (SH-SAWs) can be generated by delay line inter-digital transducers (IDTs) on the piezoelectric substrate, in which the propagating waves have a shear horizontal polarization along the propagation direction. A Love wave sensor is composed of a SH-SAW device with an additional thin film layer that has a lower shear wave velocity than the substrate to guide these waves along the surface. Compared with the traditional TSM resonator,

the Love wave sensor can be simply applied in liquid, avoiding direct contact between electrodes and liquid medium, and leading to an extensive application prospect in complex liquid or multiphase circumstances [1, 35]. Furthermore, Love waves can perform extreme sensitivity to certain surface perturbations as well as favorable inertness to other surrounding factors, especially to the number of bonds formed within the relatively short distance of ~50 *nm* from the surface [1, 36, 42]. Compared with sensitivity limitation of TSM resonator in the longitudinal direction, Love wave sensor can provide specific information on the interactions between cells and substrate in a variety of physiological processes, when the effect of environmental interferences is eliminated. In other words, sensitivity of cell-based Love wave biosensor to bonds between cells and the substrate can be significantly increased when mechanical properties of entire cell monolayer is extracted in TSM resonator biosensor measurements. As the key part of Love wave sensor, wave guiding layer plays a crucial role in improving sensor performance. Various kinds of piezoelectric and nonpiezoelectric materials have been adopted as wave guiding layer, including ZnO, SiO_2 and PMMA [43-46]. With a lack of proper bio-interface, most studies on Love wave biosensors pay no attention to their potential and much more innovative applications as cell-based biosensors. Recently, relevant experimental research reported some biocompatible polymer guiding layers, such as PMMA [43, 44], polyimide [47] and novolac [48, 49]. Parylene-C (poly(2-chloro-p-xylylene)) has been proven as an ideal wave guiding layer due to its good uniformity, compactness and adhesion to substrate [50]. More importantly, parytlene-C film possesses comparable cell and protein compatibility to the standard tissue culture substrate, indicating its great potential as a biocompatible interface [51]. In the second part of this study, the Love wave sensor with a parylene-C wave guiding layer is proposed as a new kind of cell-based biosensor to detect cell activities. So far studies in theoretical analysis of electrical

response of Love wave sensor are still quite limited, and few of them presented strong correlations with experimental results [52-55]. In this study, both analytical and numerical analysis is conducted, providing the theoretical support for parameter selection and design optimization of Love wave sensors.

1.2 SPECIFIC TASKS

In this study, two kinds of acoustic wave sensors, the TSM resonator and Love wave sensor are adopted as cell-based biosensors to evaluate and monitor cell activities.

1.2.1 Task I: Aging-related Viscoelasticity Characterization of Tendon Stem/Progenitor Cells by a Thickness Shear Mode Resonator

Aging not only affects the whole body performance but also alters cellular biological properties, including cell proliferation and differentiation. This task is designed to determine the effect of aging on mechanical properties of tendon stem/progenitor cells (TSCs), a newly discovered cell type in tendons, using quartz TSM resonators. TSCs are isolated from both old and young rats, and allowed to grow to confluency on the surface of TSM resonators. The admittance spectrums of TSM resonators with TSC monolayer are acquired, and a series of complex shear modulus $G'+jG''$ as well as average thickness h_{TSC} are calculated based on a two-layer-loading transmission line model (TLM) for TSM resonator. The results show an overall increase in G', G'' and h_{TSC} during aging process. Specifically, the storage modulus G' of aging TSCs is over ten times than that of young, revealing an important increase in stiffness of aging TSCs. In addition,

through phase-contrast and scanning electronic microscopy, it is shown that aging TSCs are large, flat and heterogeneous in morphologies while young TSCs are uniformly elongated. Increased cell size and irregular cell shape might be associated with the dense cytoskeleton organization, which could lead to an increase in both stiffness and viscosity. These results are in agreement with previously published data using different measurement methods, indicating TSM resonator as a promising tool to measure the mechanical properties of cells.

1.2.2 Task II: Real-time Monitoring the Activation Process of Platelets Using a Thickness Shear Mode Resonator

Platelets play a critical role in a number of pathophysiological processes, including hemostasis, hemorrhage, inflammation and cancer. However, it is important to analyze the states of platelets prior to use in clinical treatment to avoid inadvertent platelet activation by plasma proteins or other uncertainties. Due to its high sensitivity, repeatability, and easy connection with electronic measurement systems, the TSM resonator is adopted to monitor the process of platelet activation in this task. Resting platelets adhering to fibrinogen-coated electrodes are activated by different concentrations of thrombin (1 *U/ml*, 10 *U/ml* and 100 *U/ml*), and the corresponding electrical admittance spectrums of TSM resonators during this process are recorded. Based on a two-layer-loading transmission line model (TLM) of TSM resonators, complex shear modulus $G' + jG''$ and average thickness h_{PL} of platelet monolayer at a series of time points are obtained. Decrease in thrombin concentration from 100 *U/ml* to 1 *U/ml* shift all peaks and plateaus in G', G'' and h_{PL} to higher time points, which could be attributed to the partial activation of platelets by low concentrations of thrombin. The peak value of h_{PL} is acquired when platelets present their typical spherical shape as the first transformation in activation process. The G' peak appear 10 ~ 20 *min*

after h_{PL} peak, when some filopods are observed along the periphery of platelets but without obvious cell spreading. As platelet spreading begins and continues, G', G'' and h_{PL} decrease, leading to a steady rise of resonance frequency shift of TSM resonators. The results show high reliability and stability of TSM resonators in monitoring the process of platelet activation, revealing an effective method to real-time measure platelet activities under multiple experimental conditions. The G', G'' and h_{PL} values could provide useful quantitative measures on platelet structure variations in activation process, indicating potential of TSM resonators in characterization of cells during their transformation.

1.2.3 Task III: A Cell-based Love-mode Acoustic Wave Biosensor with a Viscoelastic Wave Guiding Layer

The Love mode surface acoustic wave (SAW) sensor is considered as one of the most promising probing methods in biomedical research and diagnosis. Recent studies have reported the structural and functional optimization of Love wave sensors for reducing propagation loss and improving sensitivity; however, the relevant device performance need be analyzed in depth in terms of device structure, electromechanical properties of piezoelectric crystal substrates, viscoelastic properties of wave guiding layers, and the effect of liquid loading. A 36° *YX*-$LiTaO_3$ based Love wave sensor with a parylene-C wave guiding layer is considered as a cell-based biosensor in this task. A theoretical model is proposed to describe the Love wave propagation in the wave guiding layer and adherent cell layer, and penetration in the liquid medium. The effects of viscoelastic wave guiding layer and liquid medium on the effective electromechanical coupling coefficient K^2 of the sensor, the propagation loss *PL*, and sensor response to mass loading (mass sensitivity) are investigated. The numerical results indicate that the maximum

propagation velocity is found at $h/\lambda = 0$, where h is the thickness of wave guiding layer and λ is the wavelength; and the optimal coupling coefficient and mass sensitivity can be obtained at $h/\lambda = 0.045$ and $h/\lambda = \sim 0.06$ in vacuum, or ~0.058 in water, respectively. For a good combination of these device performance parameters, it is suggested that the optimal wave guiding layer thickness in a Love wave biosensor is at the vicinity of $h/\lambda = \sim 0.05$ in vacuum, and ~0.048 in liquid (water). The Love wave sensor with a parylene-C wave guiding layer is applied to monitor the adhesion process of cells. The effects of viscoelastic cell layer and wave guiding layer on the propagation velocity υ and propagation loss PL are analyzed. The numerical results indicate that the adherent cell layer of various storage or loss shear modulus in certain range can induce evident, characteristic variations in υ and PL, revealing the potential of Love wave sensors in providing useful quantitative measures on cellular mechanical properties. Compared with TSM resonator, the response of Love wave sensor to the cell adhesion is primarily induced by the formation of bonds between cells and the substrate. The Love wave biosensor is considered an advisable tool for investigating cell activities in multiple physiological conditions.

1.2.4 Task IV: A Sensitivity-enhanced Love-mode Acoustic Wave Biosensor with a Phononic Wave Guiding Layer

Phononic crystals are periodic composite materials with an important structural feature, periodic scattering centers whose elastic property is different from a homogeneous matrix surrounding these scattering centers. Similar to optical properties in photonic crystals, acoustic waves in certain frequencies cannot propagate through this kind of frequency band structure (stop band), providing an innovative platform for noise signal filtering. In this task, a Love mode surface acoustic wave (SAW) sensor with phononic parylene-C wave guiding layer is introduced, where

arrays of filling materials are fabricated on the surface of parylene-C films. The stop band of the Love wave sensor is investigated in terms of the structural design parameters (period length and period number) and filling material's properties (density and elasticity). With specific combination of related parameters, only the acoustic waves in 120~125 *MHz* can propagate through the sensing area of Love wave sensor, when those non-operation frequencies are stopped by phononic patterns. The numerical results from both analytical solution and finite element method (FEM) reach good agreement with each other, indicating a potential design with high sensitivity and reliability in cell biology applications.

2.0 BACKGROUND

In this chapter, the basic principles and applications of piezoelectric devices, especially the acoustic wave sensors are presented. From the theoretical perspective, the piezoelectric constitutive equations and equivalent circuit analysis method, which is a basis of the following theoretical analysis of electrical response of devices, are introduced, On the other hand, the applications of piezoelectric devices and acoustic wave sensors are introduced extensively, especially the acoustic wave sensors used in biological and biomedical fields. Two kinds of acoustic wave sensors applied in this study, the TSM resonator and the Love mode SAW sensor are focused in detail. Most examples in theoretical analysis and practical applications are related to these two kinds of sensors, including the acoustic wave generation and propagation, the corresponding electrical response, and immunosensors. Based on this, the four tasks proposed in Chapter 1 can be discussed preliminarily.

2.1 PIEZOELECTRICITY

In this session, the basic principles concerning piezoelectric devices are introduced firstly, including the piezoelectric constitutive equations, the equivalent circuit method, the typical piezoelectric materials and some common piezoelectric devices in various application fields.

2.1.1 Piezoelectric Effect

Piezoelectric effect is a combined effect of the mechanical and electrical behaviors of materials. When a crystal lacks a center of inversion symmetry, the exertion of strain can change the distribution of electrical charges on the atoms and bonds in crystal, leading to a net, macroscopic, electrical polarization of the crystal [1]. This phenomenon is defined as the direct piezoelectric effect. Crystals exhibiting this direct piezoelectric effect always exhibit the converse effect as well, in which the crystal is strained by the application of an electric field.

For normal elastic materials, the elastic constitutive relation between stress and strain can be defined as that

$$\boldsymbol{T} = \boldsymbol{c}\boldsymbol{S}, T_{ij} = c_{ijkl} S_{kl} \tag{1}$$

where $\boldsymbol{T}$, $\boldsymbol{S}$ are the stress tensor and strain tensor respectively, $\boldsymbol{c}$ is the elastic stiffness constant tensor, which is a fourth-order tensor as an intrinsic characteristic of elastic materials. Since only six parameters in stress tensor $\boldsymbol{T}$ and strain tensor $\boldsymbol{S}$ are independent, the elastic constitutive relation can be simplified as follows:

$$\boldsymbol{T} = \boldsymbol{c}\boldsymbol{S}, T_I = c_{IJ} S_J \tag{2}$$

where $S_4 = S_{23}$, $S_5 = S_{13}$ and $S_6 = S_{12}$ ($T_4 = T_{23}$, $T_5 = T_{13}$ and $T_6 = T_{12}$ accordingly), and $\boldsymbol{c}$ is simplified as a 6×6 two-order tensor. Based on Newton's second law, the expression of acoustic wave propagation in normal elastic materials can be obtained as that

$$\begin{aligned} &\nabla \cdot \boldsymbol{T} = \rho \frac{\partial^2 \boldsymbol{u}}{\partial t^2}, \frac{\partial T_{ij}}{\partial x_j} = c_{ijkl} \frac{\partial S_{kl}}{\partial x_j} = c_{ijkl} \frac{\partial^2 u_l}{\partial x_j \partial x_k} = \rho \frac{\partial^2 u_i}{\partial t^2} \\ &\Rightarrow u_i(x,t) = u_{i0} e^{j(\omega t - kx)} \end{aligned} \tag{3}$$

where ρ is the density of elastic materials, and $\boldsymbol{u}$ is the particle displacement vector. Defining the equivalent elastic stiffness c, the wave number k and wave velocity υ have

$$\upsilon = \omega / k = \sqrt{c / \rho}$$
$$\rho\omega^2 = ck^2 \tag{4}$$

Meanwhile, for normal dielectric materials, the electric constitutive relation between electric displacement and electric field intensity can be defined as that

$$\boldsymbol{D} = \boldsymbol{\varepsilon E}, D_i = \varepsilon_{ij} E_j$$
$$\boldsymbol{E} = \boldsymbol{\beta D}, E_i = \beta_{ij} D_j \tag{5}$$

where $\boldsymbol{D}$, $\boldsymbol{E}$ are the electric displacement tensor and electric field intensity tensor respectively, $\boldsymbol{\varepsilon}$ and $\boldsymbol{\beta}$ are the permittivity constant and reciprocal permittivity constant. Vacuum permittivity ε_0 is $8.85 \times 10^{-12}\ Fm^{-1}$.

For piezoelectric effect is the coupling of the mechanical and electrical effects, the piezoelectric constitutive relations (***e***-type) can be described by simultaneous equations composed of the elastic constitutive relation and the electric constitutive relation, with an additional piezoelectric coupling term:

$$\boldsymbol{T} = \boldsymbol{cS} - \boldsymbol{e}^{\boldsymbol{T}} \boldsymbol{E}, T_I = c_{IJ}^E S_J - e_{Ij} E_j$$
$$\boldsymbol{D} = \boldsymbol{\varepsilon E} + \boldsymbol{eS}, D_i = \varepsilon_{ij}^S E_j + e_{iJ} S_J \tag{6}$$

where $\boldsymbol{e}$ is called as the piezoelectric constant. The piezoelectric constitutive relations can be rewritten in other forms as well (***h***-type, ***d***-type and ***g***-type), and the corresponding piezoelectric constant tensors $\boldsymbol{h}$, $\boldsymbol{d}$, $\boldsymbol{g}$ are adopted. In the ***e***-type piezoelectric constitutive relations, the equivalent elastic stiffness constant tensor of piezoelectric materials can be calculated by eliminating $\boldsymbol{E}$,

$$T_I = \dot{c}_{IJ} S_J = c_{IJ}(1 + K^2) S_J$$
$$\dot{c}_{IJ} = c_{IJ}(1 + K^2) \tag{7}$$

where K is called as the electromechanical coupling coefficient, which is determined by $\boldsymbol{c}$, $\boldsymbol{e}$ and $\boldsymbol{\varepsilon}$.

Accordingly, the acoustic wave propagation equation in piezoelectric materials follows the same form as (3) (4) in normal elastic materials:

$$u_i(x,t) = u_{i0}e^{j(\omega t - kx)}$$
$$\rho\omega^2 = \dot{c}k^2 \tag{8}$$

2.1.2 Piezoelectric Materials

In general, the basic piezoelectric materials can be classified into piezoelectric single crystals, piezoelectric ceramics and piezoelectric polymers (electroactive polymers). By far, a variety of piezoelectric materials have been widely applied in the related fields, including α-quartz (silicon dioxide, SiO_2), lithium niobate (LiNbO3), lithium tantalite ($LiTaO_3$), lead magnesium niobate-lead titanate solid solution (PMN-PT), barium titanate ($BaTiO_3$), lead zirconate titanate (PZT), aluminum nitride (AlN), zinc oxide (ZnO), polyvinylidene difluoride (PVDF), etc. Among them, $BaTiO_3$, PZT series are typical piezoelectric ceramics, when α-quartz, $LiNbO_3$ and PMN-PT are usually applied in single crystal structure. In comparison with piezoelectric single crystals and ceramics, piezoelectric polymers, such as PVDF, have their own advantages in the light weight and soft elasticity, which leads to a good acoustic impedance matching with liquid medium or the human body. In addition, they usually have a low mechanical quality factor *Q*, allowing for a broad resonance band width. Because of these advantages, small piezoelectric ceramic particles can be embedded into the polymer matrix to form the 0-3 type or 1-3 type composites, in which the related piezoelectric properties can be improved significantly. Recently, along with the development of microelectromechanical systems (MEMS), like micro-transducers and micro-actuators, interest in piezoelectric thin films has increased considerably, and applications of ZnO, AlN and PZT films have been extensively reported.

In this study, two kinds of piezoelectric single crystals are focused: α-quartz as the substrate of TSM resonator and $LiTaO_3$ as the substrate of Love mode SAW sensor. So, in this session, the related piezoelectric properties of these two kinds of single crystals are introduced in detail.

A. α-Quartz

Quartz is the earliest and the most widely used piezoelectric crystal. It undergoes the α-β phase transition at about 573˚C, when the piezoelectric constant d_{11} vanishes [56]. Quartz is usually found in polycrystalline or amorphous states in the earth's crust. For the piezoelectric applications, the relatively large α-quartz single crystals are synthesized, which is free from twinning and flaws. The point group of α-quartz crystal is 32, $D_3^4\,P3_12$ in Schoenfiles symbol. Its elastic stiffness constant tensor $\boldsymbol{c}$, permittivity constant tensor $\boldsymbol{\varepsilon}$ and piezoelectric constant tensor $\boldsymbol{e}$ are as follows [57]:

$$
\begin{aligned}
c &= \begin{bmatrix} 86.74 & 6.97 & 11.90 & 17.91 & 0 & 0 \\ 6.97 & 86.74 & 11.90 & -17.91 & 0 & 0 \\ 11.90 & 11.90 & 107.20 & 0 & 0 & 0 \\ 17.91 & -17.91 & 0 & 57.93 & 0 & 0 \\ 0 & 0 & 0 & 0 & 57.93 & 17.91 \\ 0 & 0 & 0 & 0 & 17.91 & 19.89 \end{bmatrix} GPa \\
\varepsilon &= \begin{bmatrix} 39.97 & 0 & 0 \\ 0 & 39.97 & 0 \\ 0 & 0 & 41.03 \end{bmatrix} \times 10^{-12} F/m \\
e &= \begin{bmatrix} 0.171 & -0.171 & 0 & 0.0406 & 0 & 0 \\ 0 & 0 & 0 & 0 & -0.0406 & -0.171 \\ 0 & 0 & 0 & 0 & 0 & 0 \end{bmatrix} Cm^{-2}
\end{aligned}
\tag{9}
$$

Quartz possesses a high mechanical quality factor Q (defined as the ratio of the stored energy and dissipated energy in an oscillating system with every oscillation), a high electric resistivity and a low temperature coefficient, which make it widely applied in frequency control of oscillators and filters [58]. Different cuts of α-quartz crystals have their specific applications: for example, the substrate of the TSM resonator is AT-cut (35.25˚ rotated Y-cut) α-quartz; and

ST-cut (42.25˚ *Y*-rotated, *X*-propagating) α-quartz can be used in a Love mode SAW device. In the former case of AT-cut, the rotated x_2-axis is normal to the substrate surface, and the converted $\boldsymbol{c}$, $\boldsymbol{\varepsilon}$ and $\boldsymbol{e}$ in a new Cartesian coordinate system are

$$
\begin{aligned}
c &= \begin{bmatrix} 86.74 & -8.27 & 27.14 & 3.650 & 0 & 0 \\ -8.27 & 129.75 & -7.42 & -5.70 & 0 & 0 \\ 27.14 & -7.42 & 102.82 & -9.93 & 0 & 0 \\ 3.650 & -5.70 & -9.93 & 38.61 & 0 & 0 \\ 0 & 0 & 0 & 0 & 68.80 & -2.52 \\ 0 & 0 & 0 & 0 & -2.52 & 29.02 \end{bmatrix} GPa \\
\varepsilon &= \begin{bmatrix} 39.97 & 0 & 0 \\ 0 & 40.32 & -0.50 \\ 0 & -0.50 & 40.68 \end{bmatrix} \times 10^{-12} F/m \\
e &= \begin{bmatrix} 0.1710 & -0.1523 & -0.0187 & -0.0670 & 0 & 0 \\ 0 & 0 & 0 & 0 & -0.1077 & -0.0949 \\ 0 & 0 & 0 & 0 & -0.0761 & -0.0671 \end{bmatrix} Cm^{-2}
\end{aligned}
\tag{10}
$$

And in the latter case of ST-cut, the converted $\boldsymbol{c}$, $\boldsymbol{\varepsilon}$ and $\boldsymbol{e}$ are:

$$
\begin{aligned}
c &= \begin{bmatrix} 96.90 & 27.49 & -4.96 & 0 & 13.34 & 0 \\ 27.49 & 86.74 & -8.62 & 0 & 0.86 & 0 \\ -4.96 & -8.62 & 130.76 & 0 & -1.56 & 0 \\ 0 & 0 & 0 & 30.27 & 0 & 7.39 \\ 13.34 & 0.86 & -1.56 & 0 & 41.07 & 0 \\ 0 & 0 & 0 & 7.39 & 0 & 67.55 \end{bmatrix} GPa \\
\varepsilon &= \begin{bmatrix} 40.55 & 0 & 0.53 \\ 0 & 39.97 & 0 \\ 0.53 & 0 & 40.45 \end{bmatrix} \times 10^{-12} F/m \\
e &= \begin{bmatrix} 0 & 0 & 0 & -0.0670 & 0 & 0.0981 \\ 0.0375 & -0.1710 & 0.1335 & 0 & -0.0816 & 0 \\ 0 & 0 & 0 & 0.0729 & 0 & -0.1073 \end{bmatrix} Cm^{-2}
\end{aligned}
\tag{11}
$$

With the ideal elastic and piezoelectric matrix form, pure SH-SAWs can be generated in the surface of the ST-cut quartz substrate, and an additional thin film can guide these waves along the surface to form the Love wave propagation [59]. Related details will be discussed in the following sessions.

B. Lithium Tantalate

The point group of $LiTaO_3$ crystal is 3m, C_{3V} R3c in Schoenfiles symbol. Its elastic stiffness constant tensor $\boldsymbol{c}$, permittivity constant tensor $\boldsymbol{\varepsilon}$ and piezoelectric constant tensor $\boldsymbol{e}$ are as follows [60]:

$$
\begin{aligned}
c &= \begin{bmatrix} 229.8 & 44.0 & 81.2 & -10.4 & 0 & 0 \\ 44.0 & 229.8 & 81.2 & 10.4 & 0 & 0 \\ 81.2 & 81.2 & 279.8 & 0 & 0 & 0 \\ -10.4 & 10.4 & 0 & 96.8 & 0 & 0 \\ 0 & 0 & 0 & 0 & 96.8 & -10.4 \\ 0 & 0 & 0 & 0 & -10.4 & 92.9 \end{bmatrix} GPa \\
\varepsilon &= \begin{bmatrix} 377 & 0 & 0 \\ 0 & 377 & 0 \\ 0 & 0 & 379 \end{bmatrix} \times 10^{-12} F/m \\
e &= \begin{bmatrix} 0 & 0 & 0 & 0 & 2.72 & -1.67 \\ -1.67 & 1.67 & 0 & 2.72 & 0 & 0 \\ -0.38 & -0.38 & 1.09 & 0 & 0 & 0 \end{bmatrix} Cm^{-2}
\end{aligned}
\tag{12}
$$

$LiTaO_3$ crystal exhibits excellent optical, piezoelectric and pyroelectric properties. Compared with α-quartz crystal, the low acoustic loss and large electromechanical coupling coefficient provide $LiTaO_3$ advantages in piezoelectric sensor applications [47]. $LiTaO_3$ is considered to be an ideal substrate material in high-loss applications, for example, a Love mode SAW device in liquid with a viscoelastic polymer wave guiding layer [48]. The main shortcoming of the $LiTaO_3$ crystal substrate is that it does not generate the pure SH-SAWs, which may lead to increased damping in a liquid medium [61]. The substrate of the Love mode SAW sensor in this study is 36º *Y*-rotated, *X*-propagating $LiTaO_3$, in which rotated x_2-axis is perpendicular to the substrate surface, and acoustic waves propagate along x_1-axis. The corresponding $\boldsymbol{c}$, $\boldsymbol{\varepsilon}$ and $\boldsymbol{e}$ in a new Cartesian coordinate system are:

$$
\begin{aligned}
c &= \begin{bmatrix} 233.0 & 57.80 & 69.20 & 19.00 & 0 & 0 \\ 57.80 & 273.99 & 76.67 & 1.92 & 0 & 0 \\ 69.20 & 76.67 & 240.67 & 14.95 & 0 & 0 \\ 19.00 & 1.92 & 14.95 & 90.67 & 0 & 0 \\ 0 & 0 & 0 & 0 & 103.87 & 3.69 \\ 0 & 0 & 0 & 0 & 3.69 & 83.13 \end{bmatrix} GPa \\
\varepsilon &= \begin{bmatrix} 363.0 & 0 & 0 \\ 0 & 374.0 & 8.1 \\ 0 & 8.1 & 369.0 \end{bmatrix} \times 10^{-12} F/m \\
e &= \begin{bmatrix} 0 & 0 & 0 & 0 & -2.8327 & -1.1383 \\ 0.9517 & -2.8026 & 0.3236 & 0.1769 & 0 & 0 \\ -1.2862 & 1.7235 & -1.5675 & -1.7664 & 0 & 0 \end{bmatrix} Cm^{-2}
\end{aligned}
\tag{13}
$$

In the following sessions, the SH-SAW generation and propagation in both two kinds of piezoelectric crystal substrates, the α-quartz and $LiTaO_3$, will be calculated and compared in depth, and the corresponding cuts for these substrates will be obtained theoretically.

2.1.3 Equivalent Circuit Method for Piezoelectric Transducers

The basic piezoelectric constitutive relations for piezoelectric materials have been provided in Session 2.1.1. Based on these relations, in this session, an equivalent circuit method is introduced to analyze the electric response of piezoelectric devices. The equivalent circuit method is a mechanical-electric analogy of mechanical and electric quantities, which has been used extensively in electromechanical conversion and transducer modeling. It was firstly created by K. S. Van Dyke [62], and then developed by W. P. Mason [63]. There are three basic assumptions for equivalent circuits: (1) Linearity, the output of transducer is substantially a linear function of the input; (2) Passive, the out energy is obtained from the input energy; (3) Reversibility, the ability of the transducer to convert energy is in either direction. Depending on the application fields, equivalent circuits can be classified into a variety of transducer types, including piezoelectric transducers, magnetostrictive transducers, magneto-electric transducers

and so on. For the electric field type transducers, the impedance analogy is adopted as the electric and mechanical quantities have the similar form of differential equations as follows:

$$L_e \frac{dI}{dt} + R_e I + \frac{1}{C_e}\int I dt = V_e e^{jwt}$$
$$\Rightarrow (j\omega L_e + R_e + \frac{1}{j\omega C_e}) I = V \tag{14}$$

$$M_m \frac{d\boldsymbol{v}}{dt} + C_m \boldsymbol{v} + K_m \int \boldsymbol{v} dt = F e^{jwt}$$
$$M_m \frac{d^2\boldsymbol{u}}{dt^2} + C_m \frac{d\boldsymbol{u}}{dt} + K_m \boldsymbol{u} = F e^{jwt} \tag{15}$$

where L_e, R_e and C_e are the electric inductance, resistance and capacitance, and M_m, C_m and K_m are the mass, viscous/dissipation coefficient and elastic coefficient, respectively. Thus, for piezoelectric devices, the corresponding impedance analog relations between mechanical and electric quantities are described in Table 1.

Table 1. Equivalent parameters in impedance analogy of equivalent circuits

Mechanical Quantity	**Electrical Quantity**
Force $\boldsymbol{F}$	Potential V
Velocity $\boldsymbol{v}$	Current I
Displacement $\boldsymbol{u}$	Charge Q
Mass M	Inductance L_e
Viscous Coefficient C_m	Resistance R_e
Elastic Coefficient K_m	Reciprocal of Capacitance C_e

The establishment of equivalent circuits for a quartz TSM resonator is taken as an analysis example. A Cartesian coordinate system (x_1, x_2, x_3) is set up accordingly, in which x_1-axis is parallel to the particle displacement direction, and x_2-axis is normal to the substrate surface, parallel to the wave propagation direction. The quartz crystal substrate occupies the

domain of $0 \le x_2 \le h_q$. In this case, ***h***-type piezoelectric constitutive equations are adopted for AT-cut quartz crystal substrate,

$$\begin{aligned} T_6 &= c_{66}^D S_6 - h_{26} D_2 \\ E_2 &= \beta_{22}^S D_2 - h_{26} S_6 \end{aligned} \tag{16}$$

Firstly, from the second equation of (16),

$$\begin{aligned} &\frac{\partial E_2}{\partial x_2} = \frac{\partial(\beta_{22}^S D_2)}{\partial x_2} - \frac{\partial(h_{26} S_6)}{\partial x_2} = -h_{26}\frac{\partial S_6}{\partial x_2} = -h_{26}\frac{\partial^2 u_1}{\partial x_2^2} \\ &\Rightarrow E_2 = -h_{26}\frac{\partial u_1}{\partial x_2} + C \end{aligned} \tag{17}$$

Thus, the electric potential V through the entire quartz crystal is obtained as

$$\begin{aligned} &V = \int_0^{h_q} E_2 dx_2 = \int_0^{h_q} (-h_{26}\frac{\partial u_1}{\partial x_2} + C) dy = -h_{26}(-\zeta_1' - \zeta_1) + Ch_q \\ &\Rightarrow C = \frac{V}{h_q} - \frac{h_{26}}{h_q}(\zeta_1 + \zeta_1') \\ &\Rightarrow E_2 = -h_{26}\frac{\partial u_1}{\partial y} + \frac{V}{h_q} - \frac{h_{26}}{h_q}(\zeta_1 + \zeta_1') \\ &\Rightarrow D_2 = \frac{E_2}{\beta_{22}^S} + \frac{h_{26} S_6}{\beta_{22}^S} = \frac{V}{h_q \beta_{22}^S} - \frac{h_{26}}{h_q \beta_{22}^S}(\zeta_1 + \zeta_1') \end{aligned} \tag{18}$$

where ζ_1 and ζ_1' are the particle displacement along x_1-axis on the two sides of quartz crystal. Defining the electric current I and surface area of quartz crystal substrate A,

$$I = \frac{\partial}{\partial t}(D_2 A) = j\omega D_2 A = \frac{j\omega A V}{h_q \beta_{22}^S} - \frac{A h_{26}}{h_q \beta_{22}^S}(\upsilon_1 + \upsilon_1') \tag{19}$$

where υ_1 and υ_1' are the corresponding linear velocity on the quartz crystal surface. With

$$C_0 = \frac{A}{h_q \beta_{22}^S}, N = h_{26} C_0 = \frac{A h_{26}}{h_q \beta_{22}^S} \tag{20}$$

the first relation between the electric potential V and υ_1, υ_1', I can be obtained as

$$\begin{aligned} &I = j\omega D_2 A = j\omega C_0 V - N(\upsilon_1 + \upsilon_1') \\ &\Rightarrow \frac{h_{26}}{j\omega} I = h_{26} D_2 A = NV - \frac{N^2}{j\omega C_0}(\upsilon_1 + \upsilon_1') \\ &\Rightarrow V = \frac{N}{j\omega C_0}(\upsilon_1 + \upsilon_1') + \frac{1}{j\omega C_0} I = \frac{h_{26}}{j\omega}(\upsilon_1 + \upsilon_1') + \frac{1}{j\omega C_0} I \end{aligned} \tag{21}$$

In the meantime, from the first equation of (16),

$$
\begin{aligned}
&T_6 = c_{66}^D S_6 - h_{26} D_2 \\
&\Rightarrow \frac{\partial T_6}{\partial x_2} = \rho \frac{\partial^2 u_1}{\partial t^2} = \frac{\partial (c_{66}^D S_6)}{\partial x_2} - \frac{\partial (h_{26} D_2)}{\partial x_2} = \frac{c_{66}^D}{\rho} \frac{\partial^2 u_1}{\partial x_2^2} = \upsilon^2 \frac{\partial^2 u_1}{\partial x_2^2} \\
&\Rightarrow \upsilon^2 \frac{\partial^2 u_1}{\partial x_2^2} + \omega^2 u_1 = 0 \\
&\Rightarrow u_1 = \frac{\zeta_1 \sin(k(h_q - y)) - \zeta_1 ' \sin(ky)}{\sin(kh_q)}, k = \omega / \upsilon
\end{aligned}
\tag{22}
$$

where υ equal to $(c_{66}{}^D/\rho)^{1/2}$ is the phase velocity of acoustic waves through the entire quartz crystal. The other two equations between the external forces on the substrate surface F_1, F_1' and υ_1, υ_1', I can be obtained as well,

$$
\begin{aligned}
&-F_1 = c_{66}^D (\frac{\partial u_1}{\partial x_2})_{x_2=0} A - h_{26} D_2 A = -c_{66}^D Ak \frac{\zeta_1 \cos(kh_q) + \zeta_1 '}{\sin(kh_q)} - h_{26} D_2 A \\
&-F_1 ' = c_{66}^D (\frac{\partial u_1}{\partial x_2})_{x_2=h_q} A - h_{26} D_2 A = -c_{66}^D Ak \frac{\zeta_1 + \zeta_1 ' \cos(kh_q)}{\sin(kh_q)} - h_{26} D_2 A \\
&\Rightarrow F_1 = \frac{c_{66}^D Ak}{j\omega} \frac{\upsilon_1 \cos(kh_q) + \upsilon_1 '}{\sin(kh_q)} - \frac{N^2}{j\omega C_0} (\upsilon_1 + \upsilon_1 ') + NV = \rho \upsilon A \frac{\upsilon_1 \cos(kh_q) + \upsilon_1 '}{j \sin(kh_q)} + \frac{h_{26}}{j\omega} I \\
&\Rightarrow F_1 ' = \frac{c_{66}^D Ak}{j\omega} \frac{\upsilon_1 + \upsilon_1 ' \cos(kh_q)}{\sin(kh_q)} - \frac{N^2}{j\omega C_0} (\upsilon_1 + \upsilon_1 ') + NV = \rho \upsilon A \frac{\upsilon_1 + \upsilon_1 ' \cos(kh_q)}{j \sin(kh_q)} + \frac{h_{26}}{j\omega} I
\end{aligned}
\tag{23}
$$

Therefore, an acoustic-electrical analogy for a quartz TSM resonator can be defined in the following matrix form, which establishes an explicit relation between mechanical parameters and the corresponding electrical response of the resonator:

$$
\begin{bmatrix} F_1 \\ F_1 ' \\ V \end{bmatrix} = -j \begin{bmatrix} Z_C \cot \alpha_q & Z_C (\sin \alpha_q)^{-1} & h/\omega \\ Z_C (\sin \alpha_q)^{-1} & Z_C \cot \alpha_q & h/\omega \\ h/\omega & h/\omega & 1/\omega C_0 \end{bmatrix} \begin{bmatrix} \upsilon_1 \\ \upsilon_1 ' \\ I \end{bmatrix}
\tag{24}
$$

where Z_C, α_q, h and C_0 are defined as follows:

$$
\begin{aligned}
&Z_C = AZ_q = A\sqrt{\rho c_{66}^D} \\
&\alpha_q = \omega h_q \sqrt{\rho / c_{66}^D} \\
&h = e_{26} / \varepsilon_{22} \\
&C_0 = \varepsilon_{22} A / h_q
\end{aligned}
\tag{25}
$$

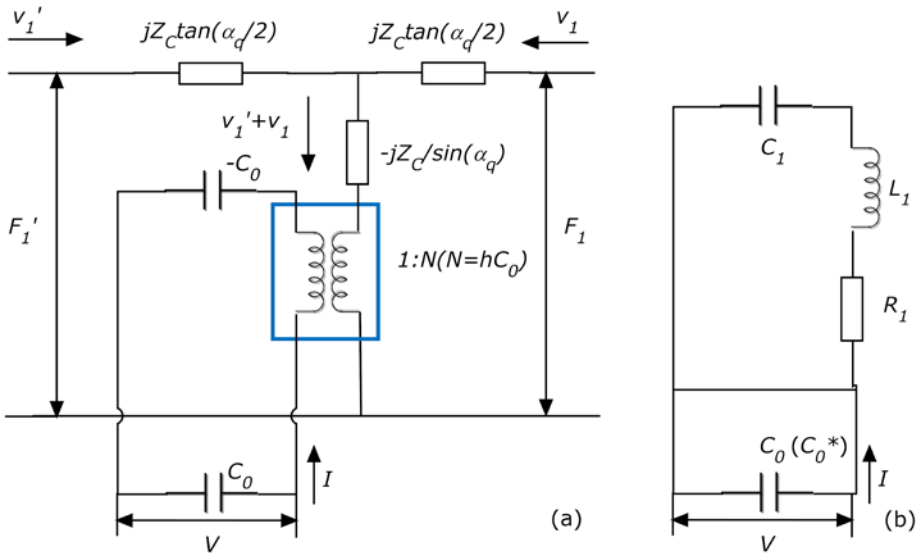

Figure 2. Equivalent circuit of a thickness shear mode resonator

Fig. 2(a) presents the distributed equivalent circuit diagram of the quartz TSM resonator based on (24), in which all related parameters have the same meanings with the calculation above. Fig. 2(b) is the lumped-element (also called as Butterworth-Van Dyke) equivalent circuit diagram. This circuit is composed of two branches, one static branch (C_0) and one motional branch (C_1, L_1 and R_1). As a simplified model of the distributed circuit, the lump-element circuit can be used to describe the electrical characteristics of the resonator over a range of frequency near resonance (only the fundamental resonance is considered). Besides C_0, the other elements of this circuit are given by [1]:

$$\begin{aligned} c_{66}^{D} &= \mu_q + j\omega\eta_q \\ C_1 &= 8e_{26}^2 C_0 / \pi^2 \varepsilon_{22}\mu_q \\ L_1 &= 1/\omega_0^2 C_1 \\ R_1 &= \eta_q / \mu_q C_1 \end{aligned} \tag{26}$$

where μ_q, η_q are the shear stiffness and viscosity of quartz crystal respectively; ω is the angular velocity, and ω_0 is the fundamental resonance angular velocity.

2.1.4 Piezoelectric Devices

On a basis of direct and converse piezoelectric effects, a number of applications have been developed in the forms of different piezoelectric devices [64]. According to the principles of work, piezoelectric devices can be classified into generators, sensors, transducers and actuators. Among them, generators and sensors utilize the direct piezoelectric effect, converting the mechanical energy into electric signals, when actuators work based on the converse effect. Both direct and converse effects are employed in transducers.

Generators are an application of direct piezoelectric effect, and one of the basic generators is a gas igniter. Under applied mechanical stress, either by a rapid, pulsed force or a more gradual, continuous increased one, a very high voltage generated in the piezoelectric ceramic can cause sparking and ignite the flammable gas.

Based on the direct piezoelectric effect, piezoelectric sensors can be utilized to detect the stress, pressure, acceleration or velocity/angular velocity of the objects, in one word, all strain/stress related. Taking a stress sensor as an example, when a force along the normal direct is exerted on a certain surface, an output voltage can be acquired accordingly. Through combining an appropriate number of piezoelectric plates (extensional and shear types), the multilayer sensor can detect 3-dimensional (3D) stresses. Piezoelectric devices are termed as acoustic wave devices specifically when mechanical vibration is electrically excited in them, such as resonators (oscillators) or filters. For these acoustic devices, varied vibration modes and piezoelectric materials will be chosen in different application fields, and the corresponding device structure, the size or the shape need be designed. For example, for speakers or buzzers, a rather low resonance frequency (~*kHz*) is required to make them audible by humans. The resonance frequency of bending mode (flexural mode) in a centimeter-size sample ranges from

100 to 1000 *Hz*, which is suitable for a piezoelectric buzzer. In comparison, the resonance frequency of thickness mode is much higher (~100 *kHz*). Currently, ultrasonic waves are used extensively. For these vibration applications, especially at high frequencies, the piezoelectric materials should have a high mechanical quality factor *Q* rather than a large piezoelectric coefficient ***d***, and as a result, hard piezoelectric materials with a high *Q* are preferable. Acoustic wave resonators or passive devices can be employed as sensors, which will be discussed in detail in following sessions. Besides, vibration at resonant frequency enables the piezoelectric materials to be used as a wave filter, which is required to pass a certain selected frequency band or to block a given band.

With use of both direct and converse piezoelectric effects, ultrasonic transducers can convert electrical energy into a mechanical loading when generating an acoustic pulse, or convert mechanical energy into an electrical signal when detecting its echo. By transferring the acoustic energy from the piezoelectric materials to other surrounding medium, a series of ultrasonic instruments, such as ultrasonic cleaning, ultrasonic welding, ultrasonic humidifier, and ultrasonic microphones, are developed. In the meantime, when transmitted waves propagate into an object and are reflected, the so-called echoes are received by the same transducer. In this case, depending on the states of object the characteristics of echoes will be varied, which can be applied in remote control and detection, such as ultrasound diagnosis, sonars, nondestructive testing, and so on. In fact, ultrasonic scanning detectors are very useful in medical electronics for clinical applications, not only in diagnosis nut also in therapy and surgery. Furthermore, when the input and output terminals are fabricated on a piezoelectric substrate and the input/output voltage is changed through the vibration energy transfer, the device is called a piezoelectric transformer as another type of piezoelectric transducers. Because of their compact size in

comparison with the conventional electromagnetic coil-type transformers, piezoelectric transformers can be widely used in televisions or lap-top computers.

Last but not least, based on the converse piezoelectric effect, piezoelectric actuators have become the crucial component in smart actuator systems, such as precision positioners, miniature ultrasonic motors, and adaptive mechanical dampers. The specific application fields of piezoelectric actuators can be classified into three categories: positioners, motors and vibration suppressors. In manufacturing of some precision optical instruments such as lasers and cameras, the positioning accuracy of semiconductor chips are generally at the order of 0.1 millimeter (*mm*), which must be adjusted by solid-state actuators. In similarity with the piezoelectric transformers, the ultrasonic motors own the advantage that their efficiency is insensitive to size. For conventional electromagnetic motors, it is rather difficult to fabricate a tiny motor smaller than 1 cm^3 with sufficient energy efficiency. Therefore, a new type of motors, ultrasonic motors with compact size, light weight and high energy efficiency, is considered as an advisable choice in the mini-motor area. Compared with conventional motors, the drive of ultrasonic motors is through a frictional force, which is direct and quiet. In addition, piezoelectric vibration suppression is also promising in space structures and military vehicles.

2.2 ACOUSTIC WAVE SENSORS

From a perspective of engineering applications, some important conceptions on acoustic wave sensors are introduced in this session. The basic vibrations modes of acoustic wave devices, as well as their own practical applications are discussed, especially the thickness shear mode and shear-horizontal mode (Love mode). Through the theoretical calculation, the relations between

vibration modes and specific piezoelectric crystal cuts are established further. In addition, this session presents details on the sensor selection and design for various applications, from the traditional applications as a mass sensor or a pressure sensor to the innovative applications as a cell-based biosensor.

2.2.1 Vibration in Piezoelectric Substrate

As shown in Session 2.1.3, with the varied electric loading on piezoelectric materials, a series of different acoustic wave modes can be excited. Table 2 presents the basic vibration modes in piezoelectric devices and their corresponding frequency range. Due to its low frequency range, the flexural mode is usually applied in piezoelectric buzzers. In Table 2, from top to bottom, as the applicable frequency band is increased, the other modes can be used in *kHz*, *MHz* and even high frequency (HF) devices.

A. Thickness Shear Mode Acoustic Waves

The typical working frequency of thickness shear (torsion) mode is usually between 1 ~ 10 *MHz,* which is primarily determined by the fabrication techniques of piezoelectric materials. As a result, this mode can be found in a series of *MHz* filters and resonators. A similar Cartesian coordinate system (x_1, x_2, x_3) is set up as in Session 2.1.3, in which x_1-axis is parallel to the particle displacement direction, and x_2-axis is parallel to the wave propagation direction. The thickness of quartz crystal along x_2-axis is h_q. Starting with the ***e***-type piezoelectric constitutive equations for AT-cut quartz crystal substrate,

$$\begin{aligned} T_6 &= c_{66}S_6 - e_{26}E_2 \\ D_2 &= \varepsilon_{22}^S E_2 + e_{26}S_6 \end{aligned} \tag{26}$$

Following Newton's second law,

$$\frac{\partial T_6}{\partial x_2} = c_{66}\frac{\partial^2 u_1}{\partial x_2^2} + e_{26}\frac{\partial^2 \varphi}{\partial x_2^2} = \rho\frac{\partial^2 u_1}{\partial t^2}$$
$$\frac{\partial D_2}{\partial x_2} = -\varepsilon_{22}^S\frac{\partial^2 \varphi}{\partial x_2^2} + e_{26}\frac{\partial^2 u_1}{\partial x_2^2} = 0 \tag{27}$$

Assuming the general solution of u_1 and φ as that

$$u_1 = Ue^{i\omega t} = (U_1 e^{ikx_2} + U_2 e^{-ikx_2})e^{i\omega t}$$
$$\varphi = \Phi e^{i\omega t} = (\Phi_1 e^{ikx_2} + \Phi_2 e^{-ikx_2})e^{i\omega t} \tag{28}$$

where the wave number $k = \omega/\upsilon$, υ is the phase velocity. Substituting (28) into (27), a linear homogeneous equation set with respect to U and Φ is obtained:

$$\begin{bmatrix} c_{66} - \rho\upsilon^2 & e_{26} \\ e_{26} & -\varepsilon_{22}^S \end{bmatrix}\begin{bmatrix} U \\ \Phi \end{bmatrix} = 0 \tag{29}$$

For an effective nontrivial solution, the determinant of coefficient matrix should be zero, which results in

$$\upsilon = \sqrt{\frac{1}{\rho}(c_{66} + \frac{e_{26}^2}{\varepsilon_{22}^S})} = \sqrt{c_{66}^D / \rho} \tag{30}$$

The phase velocity υ has the same expression as in Session 2.1.3, indicating the validity of the general solution assumption. Considering the boundary conditions that the both sides of quartz crystal substrate are free surface in series resonance states,

$$x = 0, T_6 = ik(c_{66} + \frac{e_{26}^2}{\varepsilon_{22}^S})(U_1 - U_2)e^{i\omega t} = 0$$
$$x = h_q, T_6 = ik(c_{66} + \frac{e_{26}^2}{\varepsilon_{22}^S})(U_1 e^{ikh_q} - U_2 e^{-ikh_q})e^{i\omega t} = 0 \tag{31}$$

Thus, the fundamental resonance condition for the quartz TSM resonator can be obtained as that

$$U_1 = U_2 = U_0, kh_q = \pi$$
$$\Rightarrow u_1 = (e^{ikx_2} + e^{-ikx_2})U_0 e^{i\omega t}, \omega_0 = \upsilon\pi / h_q \tag{32}$$

Table 2. Basic vibration modes in piezoelectric devices

Vibrating Mode	Vibration Direction & Propagation	Frequency Range/*Hz*
Flexural Mode	Vibration in bending directions.	< 30 *k*
Length/Radial Mode	Length vibration that expands or contracts a thin plate.	30 *k* ~ 1 *M*
Area Expansion Mode	Area expansion vibration over a surface of a thin plate.	100 *k* ~ 3 *M*
Thickness Shear/Torsion Mode	Thickness shear vibration over a surface of a thin plate (when the electric field is perpendicular to the direction of polarization).	1 *M* ~ 10 *M*
Thickness Expansion Mode	Vibration in the thickness direction of a thin plate.	3 *M* ~ 100 *M*
Rayleigh Mode SAW	Surface wave that conveys energy over the board surface with both longitudinal and transverse waves, and exponentially reduces energy in the board thickness direction.	> 6 *M*
Shear-Horizontal SAW	Surface wave that conveys energy over the board surface only with transverse waves, and exponentially reduces energy in the board thickness direction as Rayleigh mode SAWs.	10 *M* ~ 150 *M*

B. Shear-Horizontal Surface Acoustic Waves (Love Mode)

Shear-horizontal SAW (SH-SAW) mode is usually adopted in the HF applications, whose typical working frequency is between 10 ~ 150 *MHz*. The working frequency for a SH-SAW sensor depends on the design of inter-digital transducer (IDT) electrodes. For the same piezoelectric substrate, a smaller period length of IDT finger space can result in a higher working frequency. This mode can be found in a series of HF traps, filters and resonators. SH-SAWs can be generated in some specific piezoelectric materials, including α-quartz and $LiTaO_3$. In Session 2.1.2, the basic properties of these two piezoelectric crystals are presented. In this session, through the analysis of acoustic propagation equations, the characteristics of SH-SAWs in the different substrates are discussed. For analysis purpose, a Cartesian coordinate system x_1, x_2, and x_3 is established firstly, where x_1-axis is parallel to the direction of SH-SAW propagation, x_2-axis

is in the polarization direction and x_3-axis is perpendicular to the surface of piezoelectric crystal substrate. The substrate occupies the domain of $x_3 \leq 0$, which is considered semi-infinite.

The ***e***-type constitutive equations for a piezoelectric crystal substrate are given in (6):

$$\begin{aligned} \boldsymbol{T} &= \boldsymbol{cS} - \boldsymbol{e}^T \boldsymbol{E} \\ \boldsymbol{D} &= \boldsymbol{\varepsilon E} + \boldsymbol{eS} \end{aligned} \tag{6}$$

With

$$\boldsymbol{S} = \nabla \boldsymbol{u} \tag{33}$$

$$\boldsymbol{E} = -\nabla \varphi \tag{34}$$

where $\boldsymbol{u}$ and φ are respectively the particle displacement and electric potential, $\boldsymbol{S}$ and $\boldsymbol{E}$ can be eliminated from the constitutive equations (6). Meanwhile, neglecting gravity and other internal forces, the particle motion follows Newton's second law in (3):

$$\nabla \cdot \boldsymbol{T} = \rho \frac{\partial^2 \boldsymbol{u}}{\partial t^2} \tag{3}$$

Divergence of the electric displacement is zero when there are no external electric charges,

$$\nabla \cdot \boldsymbol{D} = 0 \tag{35}$$

Replacing (6) with (3), (35), the constitutive equations with respect to $\boldsymbol{u}$ and φ are rewritten as follows:

$$\begin{aligned} c_{ijkl} \frac{\partial^2 u_l}{\partial x_j \partial x_k} + e_{kij} \frac{\partial^2 \varphi}{\partial x_j \partial x_k} &= \rho \frac{\partial^2 u_i}{\partial t^2} \\ -\varepsilon_{ij}^S \frac{\partial^2 \varphi}{\partial x_i \partial x_j} + e_{ijk} \frac{\partial^2 u_k}{\partial x_i \partial x_j} &= 0 \end{aligned} \tag{36}$$

Pure shear-horizontal particle motion can be excited electrically for materials with specific elastic stiffness and piezoelectric coefficient matrices, such as ST-cut quartz crystal [54, 65]. The elastic stiffness and piezoelectric coefficient matrices of ST-cut quartz crystal take the following form:

$$\boldsymbol{c}=\begin{bmatrix} c_{11} & c_{12} & c_{13} & 0 & c_{15} & 0 \\ c_{12} & c_{22} & c_{23} & c_{24} & c_{25} & c_{26} \\ c_{13} & c_{23} & c_{33} & 0 & c_{35} & 0 \\ 0 & c_{24} & 0 & c_{44} & 0 & c_{46} \\ c_{15} & c_{25} & c_{35} & 0 & c_{55} & 0 \\ 0 & c_{26} & 0 & c_{46} & 0 & c_{66} \end{bmatrix} \tag{37}$$

$$\boldsymbol{e}=\begin{bmatrix} 0 & e_{12} & 0 & e_{14} & 0 & e_{16} \\ e_{21} & e_{22} & e_{23} & e_{24} & e_{25} & e_{26} \\ 0 & e_{32} & 0 & e_{34} & 0 & e_{36} \end{bmatrix}$$

In this case, the particle motion along x_2-axis u_2 and electric potential φ can be solved independently by eliminating the related terms including u_1 and u_3:

$$\begin{aligned} &c_{66}\frac{\partial^2 u_2}{\partial x_1 \partial x_1}+2c_{46}\frac{\partial^2 u_2}{\partial x_1 \partial x_3}+c_{44}\frac{\partial^2 u_2}{\partial x_3 \partial x_3}+e_{16}\frac{\partial^2 \varphi}{\partial x_1 \partial x_1}+e_{36}\frac{\partial^2 \varphi}{\partial x_1 \partial x_3}+e_{14}\frac{\partial^2 \varphi}{\partial x_3 \partial x_1}+e_{34}\frac{\partial^2 \varphi}{\partial x_3 \partial x_3}=\rho\frac{\partial^2 u_2}{\partial t^2} \\ &-\varepsilon_{11}^S\frac{\partial^2 \varphi}{\partial x_1 \partial x_1}-2\varepsilon_{13}^S\frac{\partial^2 \varphi}{\partial x_1 \partial x_3}-\varepsilon_{33}^S\frac{\partial^2 \varphi}{\partial x_3 \partial x_3}+e_{16}\frac{\partial^2 u_2}{\partial x_1 \partial x_1}+e_{14}\frac{\partial^2 u_2}{\partial x_1 \partial x_3}+e_{36}\frac{\partial^2 u_2}{\partial x_3 \partial x_1}+e_{34}\frac{\partial^2 u_2}{\partial x_3 \partial x_3}=0 \end{aligned} \tag{38}$$

Assuming the general solution of u_2 and φ in piezoelectric crystal substrate as that

$$\begin{aligned} u_2 &= Ue^{-k\beta x_3}e^{j(\omega t-kx_1)} \\ \varphi &= \Phi e^{-k\beta x_3}e^{j(\omega t-kx_1)} \end{aligned} \tag{39}$$

where the wave number $k = \omega/\upsilon$, υ is the propagation velocity. Substituting (39) into (38), a linear homogeneous equation set with respect to U and Φ is obtained:

$$\begin{bmatrix} c_{44}\beta^2-2ic_{46}\beta-c_{66}+\rho\upsilon^2 & e_{34}\beta^2-ie_{36}\beta-ie_{14}\beta-e_{16} \\ e_{34}\beta^2-ie_{36}\beta-ie_{14}\beta-e_{16} & -\varepsilon_{33}^S\beta^2+2i\varepsilon_{13}^S\beta+\varepsilon_{11}^S \end{bmatrix}\begin{bmatrix} U \\ \Phi \end{bmatrix}=0 \tag{40}$$

For an effective nontrivial solution, the determinant of coefficient matrix should be zero, which results in an four-order polynomial equation of β. Part of the surface waves are propagating along the negative direction of x_3, and when $x_3 \rightarrow -\infty$, the particle displacement u_2 and the electric potential φ tend to vanish. Thus, for complex solutions of β, only roots with negative real parts should be adopted. In this case, two of the four roots of β are chosen, and the solution of u_2 and φ is in this form,

$$\begin{aligned} u_2 &= (U_1e^{-k\beta_1 x_3}+U_2e^{-k\beta_2 x_3})e^{j(\omega t-kx_1)} \\ \varphi &= (\Phi_1e^{-k\beta_1 x_3}+\Phi_2e^{-k\beta_2 x_3})e^{j(\omega t-kx_1)} \end{aligned} \tag{41}$$

where

$$\frac{U_1}{\Phi_1}=\frac{U_2}{\Phi_2}=\frac{\varepsilon_{33}^S\beta^2-2i\varepsilon_{13}^S\beta-\varepsilon_{11}^S}{e_{34}k^2\beta^2-ie_{36}k^2\beta-ie_{14}k^2\beta-e_{16}k^2} \tag{42}$$

Different from ST-cut quartz crystal, for $LiTaO_3$ of a 3*m* point group, the elastic stiffness and piezoelectric coefficient matrices are in a different form [60],

$$\boldsymbol{c}=\begin{bmatrix} c_{11} & c_{12} & c_{13} & c_{14} & 0 & 0 \\ c_{12} & c_{22} & c_{23} & c_{24} & 0 & 0 \\ c_{13} & c_{23} & c_{33} & c_{34} & 0 & 0 \\ c_{14} & c_{24} & c_{34} & c_{44} & 0 & 0 \\ 0 & 0 & 0 & 0 & c_{55} & c_{56} \\ 0 & 0 & 0 & 0 & c_{56} & c_{66} \end{bmatrix}$$
$$\boldsymbol{e}=\begin{bmatrix} 0 & 0 & 0 & 0 & e_{15} & e_{16} \\ e_{21} & e_{22} & e_{23} & e_{24} & 0 & 0 \\ e_{31} & e_{32} & e_{33} & e_{34} & 0 & 0 \end{bmatrix} \tag{43}$$

With the nonzero elements in matrices, the particle motion along x_2-axis u_2 and electric potential φ cannot be solved independently. Since the acoustic wave equations are not varied with x_2, the general solution of $\boldsymbol{u}$ and φ in piezoelectric crystal substrate is assumed as that

$$\begin{aligned} u_i &= U_i e^{-k\beta x_3} e^{j(\omega t-kx_1)}, i=1,2,3 \\ \varphi &= \Phi e^{-k\beta x_3} e^{j(\omega t-kx_1)} \end{aligned} \tag{44}$$

where the wave number $k = \omega/\upsilon$, υ is the propagation velocity. Substituting (44) into (36), linear homogeneous equations with respect to U_1, U_2, U_3 and Φ can be obtained with a 4×4 coefficient matrix. For an effective nontrivial solution, the determinant of coefficient matrix should be zero, which results in an eighth-order polynomial equation of β. Part of the surface waves are propagating along the negative direction of x_3, and when $x_3 \rightarrow -\infty$, the particle displacement $\boldsymbol{u}$ and the electric potential φ tend to vanish. Thus, 1) for complex solutions of β, roots with negative real parts are rational; 2) for pure imaginary solutions of β, roots with negative imaginary parts should be adopted. In this case, four of the eight roots of β are chosen, and the solution of $\boldsymbol{u}$ and φ is in this form:

$$
\begin{aligned}
u_i &= (M_1 A_{i1} e^{-k\beta_1 x_3} + M_2 A_{i2} e^{-k\beta_2 x_3} + M_3 A_{i3} e^{-k\beta_3 x_3} + M_4 A_{i4} e^{-k\beta_4 x_3}) e^{j(\omega t - k x_1)}, i = 1,2,3 \\
\varphi &= (M_1 A_{41} e^{-k\beta_1 x_3} + M_2 A_{42} e^{-k\beta_2 x_3} + M_3 A_{43} e^{-k\beta_3 x_3} + M_4 A_{44} e^{-k\beta_4 x_3}) e^{j(\omega t - k x_1)}
\end{aligned} \tag{45}
$$

where $[A_{1j}, A_{2j}, A_{3j}, A_{4j}]$ is the corresponding nontrivial solution of the linear homogeneous equations with β_j (j = 1,2,3,4). $M_{1\sim4}$ are the coefficients to be determined by boundary conditions. It can be seen that the acoustic waves generated in $LiTaO_3$ is not pure SH-SAWs, but with the particle motion components along x_1- and x_3-axises. For the certain piezoelectric crystal cuts like 36° *YX*-$LiTaO_3$, attenuation due to the leaky waves can be minimized and the predominant component of surface particle motion is shear horizontal. The SH-SAWs are generated by IDTs, and an additional wave guiding layer on the surface guides these waves along the surface (Love waves). With the general solution into constitutive relations (36), the shear stress on x_1–x_2 plane and the electric potential along x_3 direction in piezoelectric crystal substrate can be calculated as follows:

$$
\begin{aligned}
T_{13} &= -k(M_1 R_1 e^{-k\beta_1 x_3} + M_2 R_2 e^{-k\beta_2 x_3} + M_3 R_3 e^{-k\beta_3 x_3} + M_4 R_4 e^{-k\beta_4 x_3}) e^{j(\omega t - k x_1)}, \\
R_i &= c_{55}\beta_i A_{1i} + j c_{56} A_{2i} + j c_{55} A_{3i} + j e_{15} A_{4i}, i = 1,2,3,4 \\
T_{23} &= -k(M_1 S_1 e^{-k\beta_1 x_3} + M_2 S_2 e^{-k\beta_2 x_3} + M_3 S_3 e^{-k\beta_3 x_3} + M_4 S_4 e^{-k\beta_4 x_3}) e^{j(\omega t - k x_1)}, \\
S_i &= j c_{41} A_{1i} + c_{44}\beta_i A_{2i} + c_{43}\beta_i A_{3i} + e_{34}\beta_i A_{4i}, i = 1,2,3,4 \\
T_{33} &= -k(M_1 T_1 e^{-k\beta_1 x_3} + M_2 T_2 e^{-k\beta_2 x_3} + M_3 T_3 e^{-k\beta_3 x_3} + M_4 T_4 e^{-k\beta_4 x_3}) e^{j(\omega t - k x_1)}, \\
T_i &= j c_{31} A_{1i} + c_{34}\beta_i A_{2i} + c_{33}\beta_i A_{3i} + e_{33}\beta_i A_{4i}, i = 1,2,3,4 \\
D_3 &= -k(M_1 W_1 e^{-k\beta_1 x_3} + M_2 W_2 e^{-k\beta_2 x_3} + M_3 W_3 e^{-k\beta_3 x_3} + M_4 W_4 e^{-k\beta_4 x_3}) e^{j(\omega t - k x_1)}, \\
W_i &= j e_{31} A_{1i} + e_{34}\beta_i A_{2i} + e_{33}\beta_i A_{3i} - \varepsilon_{33}\beta_i A_{4i}, i = 1,2,3,4
\end{aligned} \tag{46}
$$

There are two possible surface conditions for the $LiTaO_3$ crystal substrate in a vacuum, free surface or metalized surface. In case of free surface, the corresponding boundary conditions are as follows:

$$
\begin{aligned}
&x_3 = 0, T_{13} = 0 \Rightarrow M_1 R_1 + M_2 R_2 + M_3 R_3 + M_4 R_4 = 0 \\
&x_3 = 0, T_{23} = 0 \Rightarrow M_1 S_1 + M_2 S_2 + M_3 S_3 + M_4 S_4 = 0 \\
&x_3 = 0, T_{33} = 0 \Rightarrow M_1 T_1 + M_2 T_2 + M_3 T_3 + M_4 T_4 = 0 \\
&x_3 = 0, \varphi = 0 \Rightarrow M_1 + M_2 + M_3 + M_4 = 0
\end{aligned} \tag{47}
$$

And in case of metalized surface, the boundary conditions are modified as that

$$
\begin{aligned}
&x_3 = 0, T_{13} = 0 \Rightarrow M_1 R_1 + M_2 R_2 + M_3 R_3 + M_4 R_4 = 0 \\
&x_3 = 0, T_{23} = 0 \Rightarrow M_1 S_1 + M_2 S_2 + M_3 S_3 + M_4 S_4 = 0 \\
&x_3 = 0, T_{33} = 0 \Rightarrow M_1 T_1 + M_2 T_2 + M_3 T_3 + M_4 T_4 = 0 \\
&x_3 = 0, D_3 = 0 \Rightarrow M_1 D_1 + M_2 D_2 + M_3 D_3 + M_4 D_4 = 0
\end{aligned}
\tag{48}
$$

The boundary conditions provide two sets of linear homogeneous equations with respect to undetermined coefficients $M_{1\sim4}$. For an effective nontrivial solution of $M_{1\sim4}$, the determinant of the 4×4 coefficient matrix should be zero. However, since the leaky waves, an approximate calculation need be performed instead, in which the propagation velocity v is determined to minimize the determinant of coefficient matrix. Fig. 3 shows determinant curves of the 4×4 coefficient matrix with respect to propagation velocity v. The propagation velocity v found in the minimum values of determinant curves are 4212 *m/s* (free surface) and 4113 *m/s* (metalized surface).

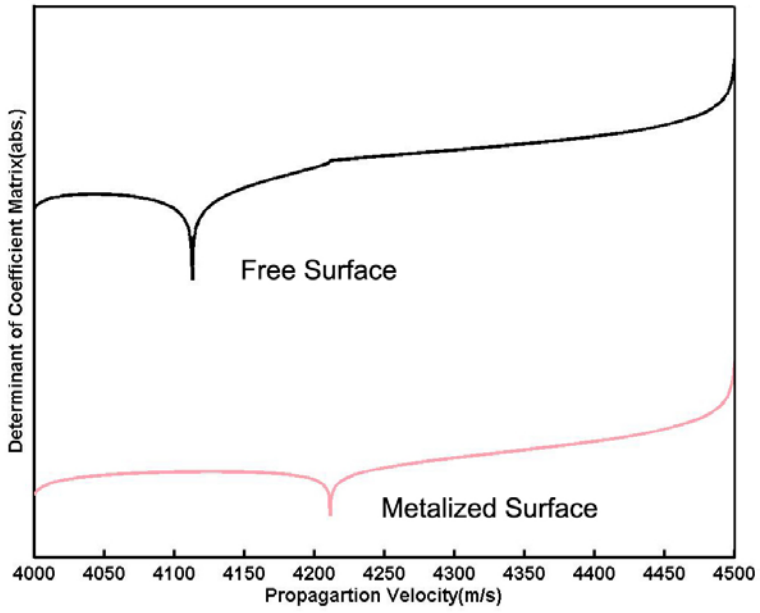

Figure 3. Determinant of coefficient matrix for 36˚ *YX*-$LiTaO_3$ substrate in vacuum

2.2.2 Classification and Comparison of Acoustic Wave Sensors

According to the characteristics of acoustic wave propagation, there is a series of classification methods for acoustic waves [1]:

(1) Depending on the direction of particle displacement with respect to the wave propagation direction, acoustic waves can be classified into parallel (longitudinal) and transverse acoustic waves. In some cases, these two types of acoustic waves exist at the same time. For example, the Raleigh waves have both the longitudinal and transverse components.

(2) Depending on the orientation of particle displacement with respect to the substrate surface, acoustic waves can be called shear-horizontal or shear-vertical acoustic waves.

(3) Depending on the wave guiding mechanism, acoustic waves can be classified into bulk, surface and plate acoustic waves. For example, the thickness shear mode and thickness expansion mode introduced in previous session belong to bulk acoustic waves, and the Raleigh waves and Love waves are both surface acoustic waves.

Using the relatively strict classification method in (3), acoustic wave sensors can be classified into bulk, surface and plate acoustic wave sensors. The typical bulk acoustic wave (BAW) sensor is the thickness shear mode (TSM) resonator (or quartz crystal microbalance, QCM). Due to its high mass sensitivity, simple structure, and easy interconnection with electronic measurement systems, quartz TSM resonator has been applied extensively. Surface acoustic wave (SAW) sensors have also been studied for many semi-quantitative and quantitative measurements due to their non-invasive, highly sensitive, real-time and long-term stable measurement features [66, 67]. Through appropriate selection of piezoelectric crystal substrates and their crystalline orientations, wave propagation directions, and structural design of the delay line IDTs, a variety of SAW sensors have be developed for sensing applications, including

Rayleigh type SAW, Leaky SAW, surface transverse wave (STW), shear-horizontal SAW (SH-SAW), and Love mode SAW sensors, etc. The shear-horizontal surface acoustic waves can be generated by delay line inter-digital transducers on, for example, a 36^{o} *YX*-$LiTaO_3$ substrate, in which the propagating waves have a shear horizontal polarization along the propagation direction. The shear horizontal polarization minimizes attenuation of the surface acoustic waves into viscous media, thus permitting detection in fluids. A Love mode SAW sensor is composed of a SH-SAW device with an additional thin film layer, which has a lower shear wave velocity than the substrate to guide these waves along the surface [68, 69]. And plate wave sensors have the acoustic plate mode (APM) and flexural plate wave (FPW) sensor. In addition, as shown in Fig. 4, according to the characteristics of acoustic wave propagation in sensors, acoustic wave sensors can be classified into the delay line device and resonator (transducer); and according to the response pattern, they can be classified into feedback oscillator and passive device then. The delay line device has two ports for separate signal input and output, such as the Love wave sensor. The resonator has only one port for both electric signal input and output, such as the TSM resonator (or QCM).

Depending on the types of acoustic waves, the working frequencies of acoustic wave sensors are varied. In general, the sensitivity of sensors is proportional to the amount of energy that is in propagation path where the perturbation takes place. For bulk acoustic wave sensors, the acoustic energy is dispersed from the surface to the other surface through the entire bulk material, thus minimizing the energy density on the sensing surface. In comparison, the surface acoustic wave sensors would concentrate the acoustic energy in the thin layer close to the sensing surface, leading to a higher sensitivity in applications. As introduced previously, the working frequency of TSM resonator is usually between 1 ~ 10 *MHz*, while the typical working

frequency of SAW sensors ranges from 10 to 150 *MHz*. If evaluating the sensitivity by $Hz/MHz/(ng/cm^2)$, the sensitivity of the TSM resonator and APM sensor are ~0.014 and ~0.019, respectively, when the Rayleigh mode and Love mode SAW sensors have quite a high sensitivity around 0.18 ~ 0.20 [70]. As the most widely used acoustic wave sensor, the TSM resonator owns the simplest geometry; however, its sensitivity is not as high as those SAW sensors [71]. With the longitudinal partial motion, the Rayleigh mode SAW sensor cannot be applied in a liquid medium. A large part of acoustic energy would penetrate into the liquid, and thus the acoustic waves are easily damped. The Love wave sensors have recently become an attractive choice in a series of applications as Love waves can occur in many common piezoelectric materials.

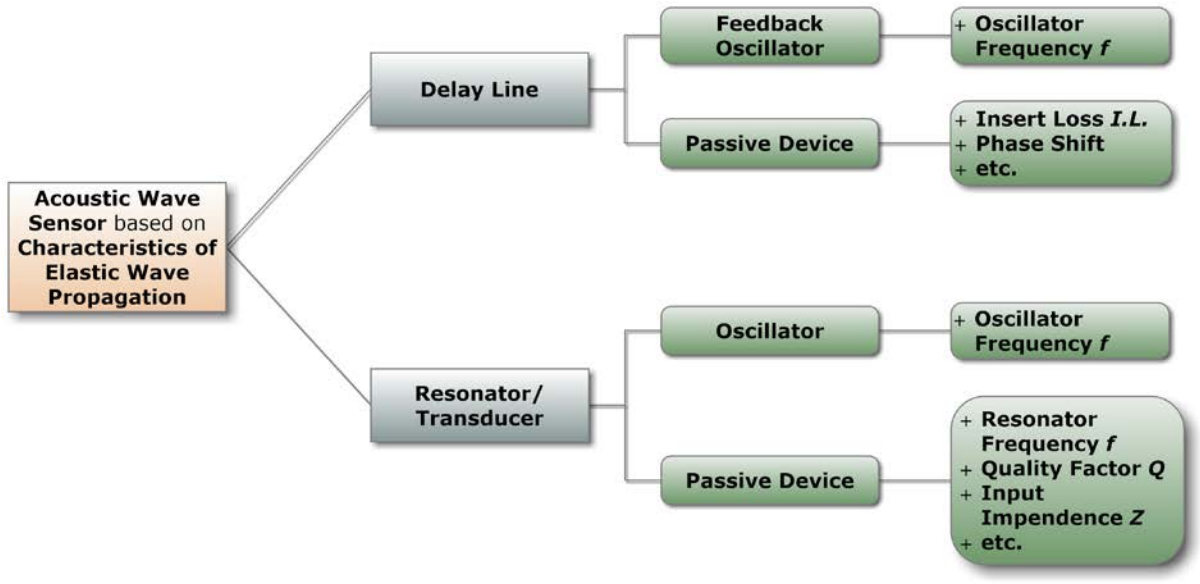

Figure 4. Classification of acoustic wave sensors based on elastic wave propagation characteristics

2.2.3 Applications of Acoustic Wave Sensors

The piezoelectric sensors are discussed in Session 2.1.4. Acoustic wave sensors are one specific kind of piezoelectric sensors, in which acoustic waves can generate and propagate. Based on the detected target parameters, the acoustic wave sensors can be used as the mass sensor, pressure sensor, temperature sensor, humidity sensor, vapor chemical sensor, biosensor and so on. Depending on different acoustic wave types, acoustic wave sensors are sensitive to the perturbation at varied degrees.

The acoustic wave sensors are ideally suited to thin film characterization to their extreme sensitivity to the thin film properties, such as mass density, viscoelasticity and conductivity. As the most widely used acoustic wave sensor, TSM resonator is widely known by its most common commercial application as a thickness gauge in thin-layer technology. When monitoring the thickness of a thin film during physical/chemical vapor deposition (PVD/CVD), the TSM resonator can act as a nanobalance, providing a real-time measurement of the thickness [72]. In general, this kind of devices is claimed a sensitivity of less than 0.1 *nm*, which implies a sensitivity less than a monolayer. The ability to rapidly monitor changes in these properties of thin film materials or fluid make the acoustic wave sensors a great tool for monitoring a series of dynamic processes, including film deposition, photo-polymerization, phase-transition, corrosion, diffusion and so on. Recently, the porous materials have attracted a lot of attention due to their light weight, good mechanical or optical properties. The acoustic wave sensors are considered as a strong tool to characterize the porous materials, or observe their related behaviors in different service conditions. Acoustic wave sensors allow the real-time characterization of materials in preparation processes, such as self-assembling, absorption at the solid-liquid or solid-gas interfaces. More importantly, the monitoring of absorption process is not only applied

extensively in basic materials science and engineering, but also extended to chemical and biochemical fields.

So far, acoustic wave sensors have been used as the chemical or biochemical sensors to detect a given reagent in the environment. In most cases, they are in the form of molecules or macromolecules, such as water vapor or other gas, enzymes, antibodies or antigens. Taking TSM resonator as an example, by suitable surface treatment, the TSM resonator can be made sensitive to one gas or another as a nanosensor. Selecting a suitable coating on the electrodes of TSM resonator, the specific gas can be absorbed and immobilized onto the sensor surface, thus determining the selectivity and enhancing the sensitivity of sensor. It can be seen that obtaining adequate selectivity and sensitivity for the measurement of a given reagent requires a chemical or biochemical interface. The interface is usually a layer of coating, which on the one hand can be physically or chemically bound to the sensor substrate surface, and on the other hand can combine with the given reagent through absorption, bonding or reaction. As a result, the modification of piezoelectric surface plays an important role in the chemical and biochemical applications. For example, conducting polymer films, like polypyrrole and polyaniline, can be prepared on the surface of metallic electrodes for chemical sensors used in electro-chemistry [72]. And, one of the most important applications of acoustic wave biosensors is the immunosensors. The crucial operation procedure for immunosensors is immobilization of immunoreagents, which strongly depends on the combination of immunoreagents and the biochemical interface. Different types of combination mechanisms can be utilized in the immunosensors, including direct immobilization of biomolecules through absorption, or entrapping of biomolecules by electrogenerated polymers. Compared with the conventional sensing applications, these generally sealed acoustic wave sensors have to be opened for

chemical or biochemical sensing applications, and their surface functionalized with a chemically sensitive coating. Viscoelastic properties of coating materials (polymers, macromolecules, etc.) and contact media (gaseous or liquid medium) can have a strong impact on the vibration behavior of piezoelectric substrate and diminish the mechanical quality factor *Q*, which will be discussed in depth in following session.

2.2.4 Research Progress in Acoustic Wave Biosensors

A series of studies have reported the acoustic wave sensors for the measurement of chemical and biological species in surrounding environments. The TSM resonator is firstly demonstrated, and then the SAW sensor and SH-APM sensor are considered owing to their higher sensitivity. As chemical or biochemical sensors, the acoustic wave sensors have been applied in the detection and concentration measurement of specific molecules in gaseous and liquid medium. For example, the TSM resonator was applied to detect the influenza virus [3]. In general, obtaining adequate sensitivity and selectivity for the measurement of a given reagent requires a suitable chemical or biochemical interface. The interface is generally a layer of coating, which acts as a chemical sensitive and selective element that immobilizes a finite mass of some reagents from the environment. The changes in the coating layer would perturb the underlying acoustic wave sensors, leading to the corresponding response of electric signals. The mechanism in this kind of detection can be classified into different types. When some of them are depending on the mass-loading changes, some others may trace the variations in the mechanical or electrical properties, such as the viscoelasticity or the impedance. A number of studies reported Au or Ag electrodes were applied as the absorbent to detect the specific chemical species in liquid. Recently, an important conception “immunosensor” was proposed, in which the corresponding antibodies are

coated on the sensing surface to immobilize the specific protein molecules. This type of biosensors can be extensively applied to a series of related fields, including toxicity testing in food industry, contamination testing in civil engineering, pharmaceutical screening in medical science and so on.

As mentioned above, the classical sensing application of TSM resonators is microgravimetry. It is a well-known tool to measure the thin film thickness in the nanometer (*nm*) range. During the deposition of thin films, the resonance frequency shift is inversely proportional to the total film thickness. Currently, microweighing is only one out of many uses of TSM resonators. The TSM resonator can be applied as an acoustic reflectometer, a high-frequency interfacial rheometer, or a micromechanical probe [73]. So far, there has been a remarkable progress in development and application of TSM resonators in sensing technology. Quartz TSM resonator has been applied to characterize the viscoelastic properties of materials bounded on its surface [33, 74]. The mechanical properties, such as the elasticity and viscosity, of the thin film or the fluid on the surface of TSM resonator can be extracted from the corresponding electric signal, which is the basis of characterization of adherent cells in this study. When using TSM resonator sensors in liquid medium, the actual variations in resonance frequency will diverge essentially from the original linear relation for a microweighing sensor in vacuum or gaseous medium. More importantly, there is considerable dissipation of acoustic energy due to liquid contact, which turns out to be the energy lost in equivalent electrical circuits. The oscillation is significantly damped and the mechanical quality factor Q is significantly reduced.

The Love mode SAW sensor has been considered as one of the most promising probing methods in both fundamental biology and biomedical engineering [37, 38]. Comparing with the

traditional TSM resonator, Love waves excited by surface IDT electrodes perform extremely sensitivity to certain surface perturbations as well as favorable inertness to other surrounding factors, resulting in an extensive application prospect of Love wave sensors in complicated liquid or multiphase circumstances [36, 42]. Love wave sensors were also applied for chemical compound sensing in liquid due to a high mass sensitivity compared with other surface acoustic wave modes [75, 76]. Due to its potential high sensitivity, the Love wave sensor is considered as an advisable tool to monitor the cell behaviors in liquid in a simple, non-invasive, and quantitative manner.

2.3 THICKNESS SHEAR MODE RESONATORS

A TSM resonator consists of a thin disk of AT-cut quartz with circular electrodes on both sides, which can be electrically excited in a number of resonant thickness shear modes. As its surface loading condition varies, the electrically-excited acoustic wave propagation can change accordingly through the entire quartz crystal. In Session 2.1.3, based on an acoustic-electrical analogy, two types of equivalent circuit models for a TSM resonator are introduced: the lumped-element model (Butterworth-Van Dyke, BVK) and the distributed model (Transmission Line Model, TLM). The former model can be derived from reduction of the later one in the near-resonant circumstance [1]. Fig. 5 and Fig. 6 respectively show the lumped-element model and transmission line model for a TSM resonator with external loading. As shown in Fig. 6, TLM has two acoustic ports and one electrical port, and via a transformer the acoustic variables, force F and linear velocity v, are coupled to an electrical port [77]. When the surface force F_1 or F_1' is changed, the electric potential V and current I can vary following the relationship indicated in

(24). For the lumped-element model, as shown in Fig. 5(b), an additional real motional resistance R_2 and inductance L_2 are caused by a change in F_1 or F_1'. Because of the zero error between its assumption and actual TSM electrical response, TLM is chosen to provide a comprehensive description for the TSM resonator with viscoelastic loading layers in this study [1, 34]. Nevertheless, some problems about coating property extraction have not been solved completely, including the effective measurement and calculation error control. It has also been found that viscoelastic coatings of varied thicknesses can induce other resonance effects, leading to an incompatibility with the calculation model [10]. In this session, a modified TLM is introduced, and based on it the corresponding storage shear modulus G' and loss shear modulus G'' of viscoelastic coatings on the surface of TSM resonator can be extracted.

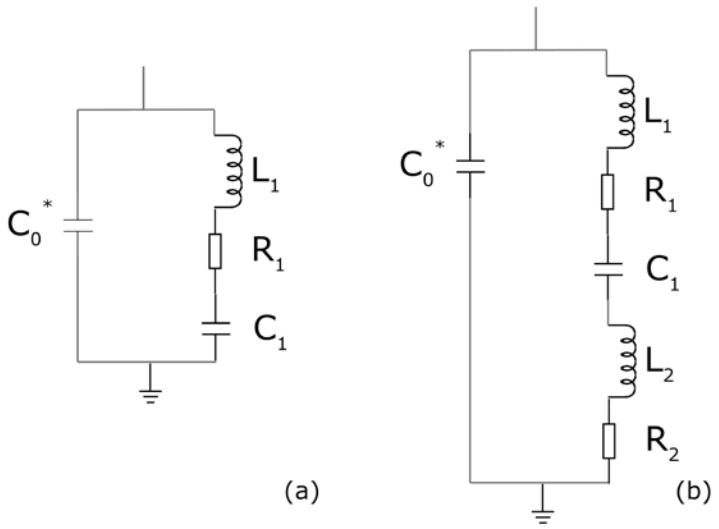

Figure 5. Lump-element model of a thickness shear mode resonator

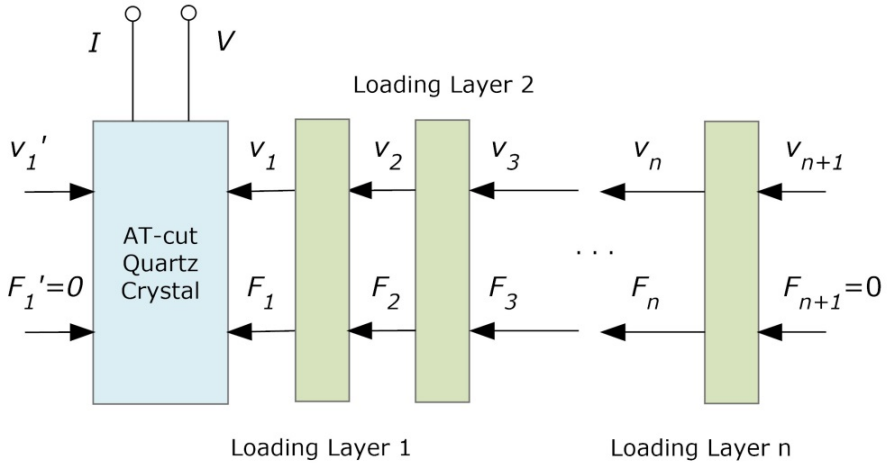

Figure 6. Transmission line model of a thickness shear mode resonator

2.3.1 Transmission Line Model for Thickness Shear Mode Resonators

The acoustic-electrical analogy of TLM can be defined as (24),

$$\begin{bmatrix} F_1 \\ F_1' \\ V \end{bmatrix} = -j \begin{bmatrix} Z_C \cot\alpha_q & Z_C(\sin\alpha_q)^{-1} & h/\omega \\ Z_C(\sin\alpha_q)^{-1} & Z_C \cot\alpha_q & h/\omega \\ h/\omega & h/\omega & 1/\omega C_0 \end{bmatrix} \begin{bmatrix} \upsilon_1 \\ \upsilon_1' \\ I \end{bmatrix} \tag{24}$$

where F_1, F_1' and v_1, v_1' are the external force and linear velocity at the TSM resonator surfaces, respectively; and Z_C, α_q, h and C_0 are defined as follows, with relevant parameters shown in Table 3:

$$\begin{aligned} Z_C &= AZ_q = A\sqrt{\rho c_{66}^D} \\ \alpha_q &= \omega h_q \sqrt{\rho / c_{66}^D} \\ h &= e_{26} / \varepsilon_{22} \\ C_0 &= \varepsilon_{22} A / h_q \end{aligned} \tag{25}$$

Table 3. Parameters of TSM resonator [57]

Density of Quartz	ρ	$2.651\times10^{3}\ kg\cdot m^{-3}$
Shear Stiffness of Quartz	$c_{66}^{D} = c_{66} + e_{26}^{2}/\varepsilon_{22} + j\omega\eta_q$	$2.970\times10^{10}\ N\cdot m^{-2} + j\omega\eta_q$
Piezoelectric Constant of Quartz	e_{26}	$9.657\times10^{-2}\ A\cdot s\cdot m^{-2}$
Dielectric Permittivity of Quartz	ε_{22}	$3.982\times10^{-11}\ A^2\cdot s^4\cdot kg^{-1}\cdot m^{-3}$
Surface Area of TSM Resonator	A	$2.047\times10^{-5}\ m^2$
Thickness of TSM Resonator	h_q (theoretical)	165 μm

Letting $Z_1 = F_1/v_1$, $Z_1' = F_1'/v_1'$ to represent the surface loading condition of TSM resonator, (24) is rewritten as

$$\begin{bmatrix} V \\ I \end{bmatrix} = [B] \cdot \begin{bmatrix} F_1 \\ \upsilon_1 \end{bmatrix} = \frac{1}{\varphi H} \begin{bmatrix} 1 & \frac{j\varphi^2}{\omega C_0} \\ j\omega C_0 & 0 \end{bmatrix} \cdot \begin{bmatrix} \cos\alpha_q + j\frac{Z_1'}{Z_C}\sin\alpha_q & Z_C(\frac{Z_1'}{Z_C}\cos\alpha_q + j\sin\alpha_q) \\ \frac{j}{Z_C}\sin\alpha_q & 2(\cos\alpha_q - 1) + j\frac{Z_1'}{Z_C}\sin\alpha_q \end{bmatrix} \cdot \begin{bmatrix} F_1 \\ \upsilon_1 \end{bmatrix} \tag{49}$$

where

$$H = \cos\alpha_q - 1 + j\frac{Z_1}{Z_q}\sin\alpha_q, \varphi = hC_0 \tag{50}$$

Defining the complex electrical impedance $Z = V/I$, complex electrical admittance $Y = I/V$, then Z and Y are expressed as

$$\begin{aligned} Z &= \frac{1}{j\omega C_0} - \frac{K^2}{j\omega C_0 \alpha_q} \frac{2\tan(\alpha_q/2) - j(Z_1 + Z_1')/Z_C}{(1 + Z_1 Z_1'/Z_C^{\,2}) - j(Z_1 + Z_1')/Z_C \cot\alpha_q} \\ Y &= j\omega C_0 + \frac{j\omega C_0 (2\tan(\alpha_q/2) - j(Z_1 + Z_1')/Z_C)}{\alpha_q / K^2 ((1 + Z_1 Z_1'/Z_C^{\,2}) - j(Z_1 + Z_1')/Z_C \cot\alpha_q) - 2\tan(\alpha_q/2) + j(Z_1 + Z_1')/Z_C} \end{aligned} \tag{51}$$

where

$$K^2 = e_{26}^2 / \varepsilon_{22} c_{66}^D \tag{52}$$

Generally speaking, for unloaded TSM resonator, both surfaces are stress free with two short-circuit acoustic terminations of $F_1 = Z_1 = F_1' = Z_1' = 0$. Substituting the Z_1 and Z_1' into (51) Y expression,

$$Y = j\omega C_0 + \frac{2 j\omega C_0 \tan(\alpha_q / 2)}{\alpha_q / K^2 - 2\tan(\alpha_q / 2)} \tag{53}$$

However, with extra layers (upper/lower electrodes, cell monolayer and culture medium) on TSM resonator surfaces, Z_1 and Z_1' are changed accordingly depending on these layers' own physical and mechanical properties. For Au or Pt electrodes on both sides are relatively thin (~100 *nm*), their effects on surface loading Z_1 and Z_1' values are neglected, which can simplify the original theoretical model effectively. Thus, Z_1 can be determined only by the properties of loading layers on upper electrode, and Z_1' is always zero. Using the boundary conditions (internal force and linear velocity) between contact layers, TLM model can be described as Fig. 6, and the corresponding transfer matrix is given [77]:

$$\begin{bmatrix} F_1 \\ \upsilon_1 \end{bmatrix} = [B_1]\cdot[B_2]\cdot\ldots\cdot[B_{n-1}]\cdot[B_n]\cdot\begin{bmatrix} F_{n+1} \\ \upsilon_{n+1} \end{bmatrix}$$
$$\begin{bmatrix} F_n \\ \upsilon_n \end{bmatrix} = [B_n]\cdot\begin{bmatrix} F_{n+1} \\ \upsilon_{n+1} \end{bmatrix} = \begin{bmatrix} \cos\alpha_n^L & jZ_n^L \sin\alpha_n^L \\ j\sin\alpha_n^L / Z_n^L & \cos\alpha_n^L \end{bmatrix}\cdot\begin{bmatrix} F_{n+1} \\ \upsilon_{n+1} \end{bmatrix} \tag{54}$$

where Z_n^L, α_n^L have similar definitions with Z_q, α_q,

$$Z_n^L = A\sqrt{\rho_n c_n}$$
$$\alpha_n^L = \omega h_n \sqrt{\rho_n / c_n} \tag{55}$$

where ρ_n, c_n and h_n are the density, stiffness and thickness of loading layer, respectively. Defining $Z_n = F_n/v_n$, $Z_{n+1} = F_{n+1}/v_{n+1}$, then

$$Z_n = Z_n^L \frac{Z_{n+1}\cos\alpha_n^L + jZ_n^L \sin\alpha_n^L}{Z_n^L \cos\alpha_n^L + jZ_{n+1}\sin\alpha_n^L} \tag{56}$$

Substituting Z_1 and Z_1' into (51) Y expression,

$$Y = j\omega C_0 + \frac{j\omega C_0(2\tan(\alpha_q/2) - jZ_1/Z_C)}{\alpha_q/K^2(1-jZ_1/Z_C\cot\alpha_q) - 2\tan(\alpha_q/2) + jZ_1/Z_C}, Z_1 = Z_1^L \frac{Z_2\cos\alpha_1^L + jZ_1^L\sin\alpha_1^L}{Z_1^L\cos\alpha_1^L + jZ_2\sin\alpha_1^L} \quad (57)$$

Nevertheless, considering the excluded electrode effect of TSM resonator, other non-uniformity influences as well as surrounding perturbations, TLM model is modified further as shown in Fig. 7. Taking all these uncertainties into account, the total parallel capacitance C_0^* is defined as [31]

$$C_0^* = C_0 + C_p \quad (58)$$

where C_0 is the static capacitance of TSM resonator, and C_p is the external capacitance.

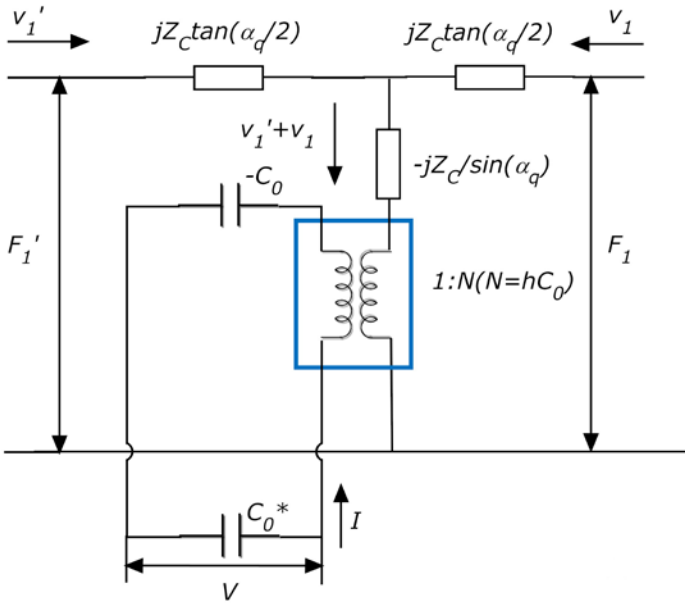

Figure 7. Modified distributed equivalent circuit of a thickness shear mode resonator

With C_0^* as a desirable way of compensation for the original TLM model, (53) (57) are respectively rewritten into (59) (60):

$$Y = j\omega C_0^* + \frac{2\, j\omega C_0 \tan(\alpha_q / 2)}{\alpha_q / K^2 - 2\tan(\alpha_q / 2)} \tag{59}$$

$$Y = j\omega C_0^* + \frac{j\omega C_0 (2\tan(\alpha_q / 2) - jZ_1 / Z_C)}{\alpha_q / K^2 (1 - jZ_1 / Z_C \cot\alpha_q) - 2\tan(\alpha_q / 2) + jZ_1 / Z_C}, Z_1 = Z_1^L \frac{Z_2 \cos\alpha_1^L + jZ_1^L \sin\alpha_1^L}{Z_1^L \cos\alpha_1^L + jZ_2 \sin\alpha_1^L} \tag{60}$$

This modified TLM model provides an explicit relationship between experimental observations (the electrical response of TSM resonator) and relevant device parameters.

2.3.2 Extraction of Complex Shear Modulus of Adherent Cells

For a TSM resonator biosensor that is frequently applied in liquid environment, a multilayer-loaded TLM is adopted when considering the liquid medium as a semi-infinite viscous layer. In this case, the actual multilayer-loading model for TSM resonator with cell adhesion consists of three mechanical impedance layers as indicated in Fig. 8(a): the protein (collagen I or fibrinogen) coating, the cell monolayer and semi-infinite viscous liquid layer (culture medium). Because the protein coating is quite thin (<20 *nm*), this model can be simplified with the protein coating as an intrinsic effect included into TSM resonator itself. By acquiring an optimal solution of effective parameters (η_q, h_q, C_0 and C_p) from the admittance of unloaded TSM resonator, effect of protein coating can be compensated as well as other surface perturbations. Fig. 8 presents an equivalent two-layer-loading model of TSM resonator for cell monolayer characterization. The model is composed of two mechanical impedance layers, the cell layer and liquid medium layer. Assuming the cell monolayer as an isotropic, homogeneous and uniform coating on quartz crystal, Z_1^L and α_1^L can be calculated as follows:

$$\begin{aligned} Z_1^L &= Z_{Cell} = A\sqrt{\rho_{Cell} G_{Cell}}, G_{Cell} = G' + jG'' \\ \alpha_1^L &= \alpha_{Cell} = \omega h_{Cell} \sqrt{\rho_{Cell} / G_{Cell}} \end{aligned} \tag{61}$$

where ρ_{Cell} is the density of objective layer, and G_{Cell} is the complex shear modulus. Meanwhile, as the liquid medium is semi-infinite,

$$Z_2 = Z_{Med} = (1+j)A\sqrt{\omega\rho_{Med}\eta_{Med}/2} \tag{62}$$

where ρ_{Med}, η_{Med} are the density and the viscosity of liquid medium respectively,. Thus, Z_1 in (60) can be be expressed as follows:

$$Z_1 = A\sqrt{\omega\rho_{Med}\eta_{Med}/2}\,\frac{2j\sqrt{\omega\rho_{Med}\eta_{Med}/2}\cos(\omega h_{Cell}\sqrt{\rho_{Cell}/G_{Cell}}) - (1-j)\sqrt{\rho_{Cell}G_{Cell}}\sin(\omega h_{Cell}\sqrt{\rho_{Cell}/G_{Cell}})}{\sqrt{\rho_{Cell}G_{Cell}}\cos(\omega h_{Cell}\sqrt{\rho_{Cell}/G_{Cell}}) - (1-j)\sqrt{\omega\rho_{Med}\eta_{Med}/2}\sin(\omega h_{Cell}\sqrt{\rho_{Cell}/G_{Cell}})} \tag{63}$$

If with only liquid medium on electrode surface, the TSM resonator is contacting directly with the semi-infinite viscous fluid, and the corresponding expression of Z_1 is as that

$$Z_1 = Z_2 = Z_{Med} = (1+j)A\sqrt{\omega\rho_{Med}\eta_{Med}/2} \tag{64}$$

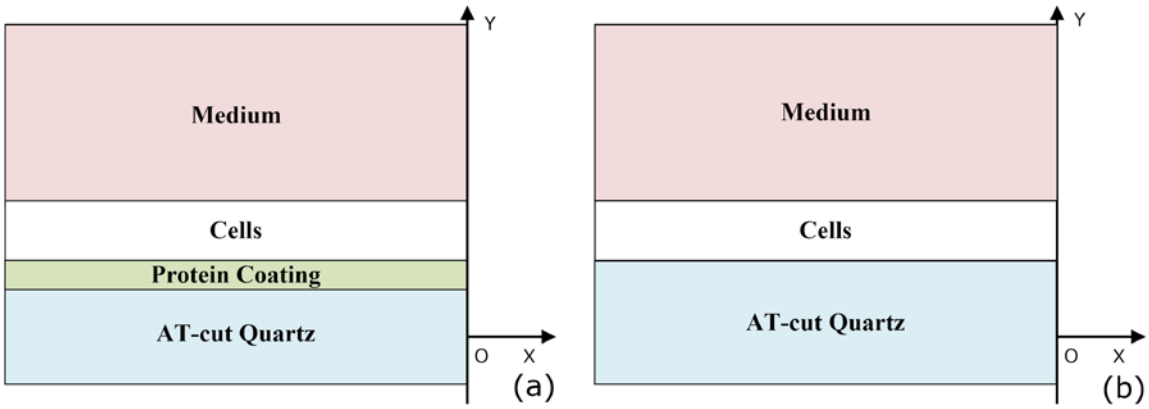

Figure 8. Schematic diagram of a thickness shear mode resonator with adherent cells

For an appropriate analysis on the TSM resonator with adherent cells, the parameter calibration of unloaded TSM resonator plays an important role in compensating additional effects from surface electrodes, protein coating and other perturbations. In this step, the optimal solution of effective parameters of TSM resonator (η_q, h_q, C_0 and C_p) is determined, where those

effects are considered as the intrinsic characteristics of TSM resonator. Two input variables are required in the algorithm of effective parameter extraction: (1) The admittance spectrum $Y(\omega_i) = G(\omega_i) + jB(\omega_i)$ of unloaded TSM resonator (including the TSM resonator with protein coating, which is considered as a special unloaded case as discussed), where i is assigned with from 1 to n, and n is the number of acquired angular frequency points. For Agilent 4294A impedance analyzer used in this study, n = 801; (2) The total parallel capacitance C_0^* that is measured at double fundamental resonance frequency based on the limiting relationship $Y = j\omega C_0^*$ [78]. By Regula-Falsi iteration method, a series of valid solution sets (η_q, h_q and C_0) are obtained, and the optimal solution is chosen among them as the one that makes the error function achieve the smallest value [79]. Error function is defined as (65), which represents the cumulative error of experimental admittance spectrum deviating from the theoretical one,

$$Error_i = \frac{\sum_{i=1}^{M}(G(\omega_i)_{EXP} - G(\omega_i)_{TLM})^2 + \sum_{i=1}^{M}(B(\omega_i)_{EXP} - B(\omega_i)_{TLM})^2}{\sum_{i=1}^{M}(G(\omega_i)_{EXP})^2 + \sum_{i=1}^{M}(B(\omega_i)_{EXP})^2} \tag{65}$$

where $G(\omega_i)_{TLM}$, $B(\omega_i)_{TLM}$ are developed from (60), and $G(\omega_i)_{EXP}$, $B(\omega_i)_{EXP}$ are from experimental observations.

In addition, prior to the extraction of cellular complex shear modulus, complex impedance of liquid medium should be obtained as well. Certain input variables are needed in the algorithm of mechanical impedance Z_{Med}: (1) The admittance spectrum $Y(\omega_i) = G(\omega_i) + jB(\omega_i)$ of TSM resonator with liquid medium; (2) Relevant effective parameters of unloaded TSM resonator extracted in previous step, including equivalent thickness h_q, quartz viscosity μ_q, static capacitance C_0, and total parallel capacitance C_0^*. Conducting the Regula-Falsi iteration method and error comparison as introduced in the first step, the optimal solution of Z_{Med} is acquired.

With (1) the modified effective parameters for TSM resonator with protein coating, (2) the complex mechanical impedance of liquid medium, as well as (3) the admittance spectrum $Y(\omega_i) = G(\omega_i) + jB(\omega_i)$ for TSM resonator with cell adhesion, the specific solution of the complex shear modulus $G_{Cell} = G' + jG''$ and average thickness h_{Cell} of cell monolayer can be determined based on the similar algorithm. The G'' discretization within an appropriate range is operated firstly, and the corresponding G' is obtained by Regula-Falsi iteration method. Among all these valid solution sets (G', G'' and h_{Cell}) recorded during this process, an optimal solution is selected as the one can make the error function defined as (65) get the smallest value.

2.4 LOVE-MODE ACOUSTIC WAVE SENSORS

The Love mode SAW sensor has been considered as one of the most promising probing methods in both fundamental biology and biomedical engineering, detecting behaviors of cells on its surface in a non-invasive, simple and quantitative manner [37, 38]. Comparing with the traditional TSM resonator, Love waves excited by surface inter-digital transducer (IDT) electrodes perform extremely sensitivity to certain surface perturbations as well as favorable inertness to other surrounding factors, resulting in an extensive application prospect of Love wave sensors in complex liquid or multiphase circumstances [36, 42]. Unlike the TSM resonator, Love waves exist only when an acoustic wave guiding layer of finite thickness is deposited on a semi-infinite piezoelectric substrate, and its shear bulk wave velocity is smaller than that in the substrate. With the piezoelectric effect of piezoelectric substrate involved, dispersion equation in the Love wave sensor becomes complicated, when the dissipation factor D can be expressed explicitly for the TSM resonator. In this session, Love wave propagation equations in a layered

Love wave biosensor in liquid medium with a viscoelastic wave guiding layer are introduced. Based on it, the corresponding electrical response of Love wave sensor can be calculated depending on different mechanical properties of loading layers.

2.4.1 Love Wave Propagation in a Layered Love Wave Sensor

The common piezoelectric substrates for Love wave sensors are quartz (ST-cut), 36º *YX*-$LiTaO_3$ and 36º *YX*-$LiNbO_3$ [41]. Among them, the low insertion loss and large electromechanical coupling coefficient provide 36º *YX*-$LiTaO_3$ advantages over other substrates [47]. Particularly, $LiTaO_3$ is considered as a better substrate material for relatively high loss applications, for example, used in liquid medium or with a viscoelastic biocompatible polymer wave guiding layer [48]. Thus, in this study, the 36˚ *YX*-$LiTaO_3$ based Love wave sensor is adopted as a cell-based biosensor to monitor cell behaviors. Fig. 9 schematically illustrates the basic structure of a Love wave biosensor: IDT electrodes are fabricated on the surface of the piezoelectric crystal substrate. A wave guiding layer is deposited on electrodes. The Love wave sensor is placed in culture medium with direct contact between the wave guiding layer and liquid medium. For analysis purpose, a Cartesian coordinate system x_1, x_2, and x_3 is established for the basic unit structure of a Love wave biosensor, where x_1-axis is parallel to the direction of Love wave propagation, x_2-axis is in the polarization direction and x_3-axis is perpendicular to the surface of piezoelectric crystal substrate. The wave guiding layer occupies the domain of $0 \leq x_3 \leq h_1$, and the cell monolayer occupies $h_1 \leq x_3 \leq h_2$. Both piezoelectric crystal substrate and liquid medium are considered semi-infinite.

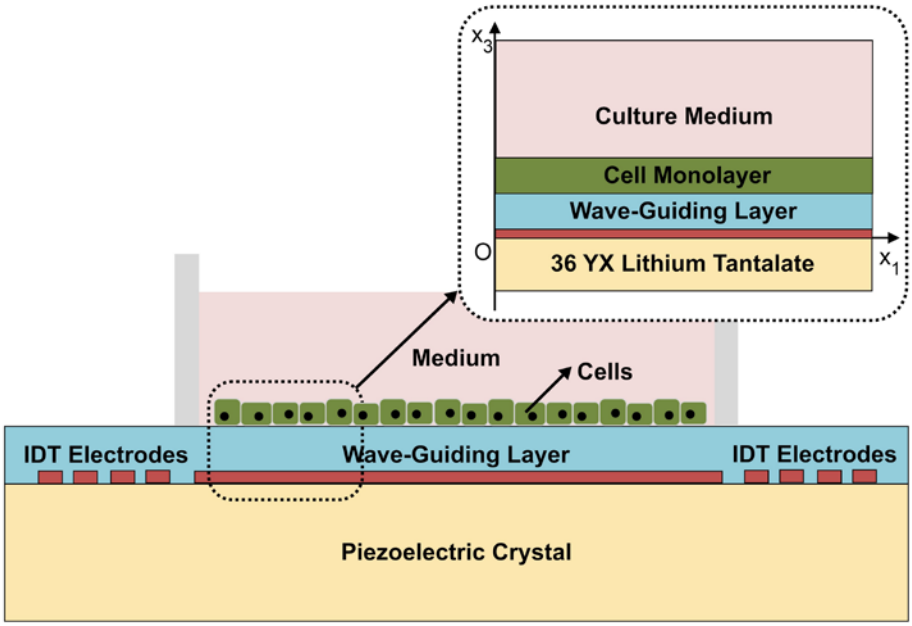

Figure 9. Schematic structure of a cell-based Love wave biosensor

As discussed in Session 2.2.1, 36º *YX*-$LiTaO_3$ substrate does not generate a pure shear wave, and the corresponding acoustic wave propagation equations are in this form:

$$u_i = (M_1 A_{i1} e^{-k\beta_1 x_3} + M_2 A_{i2} e^{-k\beta_2 x_3} + M_3 A_{i3} e^{-k\beta_3 x_3} + M_4 A_{i4} e^{-k\beta_4 x_3}) e^{j(\omega t - k x_1)}, i = 1,2,3$$
$$\varphi = (M_1 A_{41} e^{-k\beta_1 x_3} + M_2 A_{42} e^{-k\beta_2 x_3} + M_3 A_{43} e^{-k\beta_3 x_3} + M_4 A_{44} e^{-k\beta_4 x_3}) e^{j(\omega t - k x_1)} \quad (45)$$

where the wave number $k = k_0 - j\alpha = \omega/\upsilon - j\alpha$ ($\alpha > 0$), υ is the propagation velocity, α is the attenuation factor of wave propagation, and $\alpha << 1$ for normal piezoelectric crystal substrates; β_j (j = 1,2,3,4) are the four effective roots of an eighth-order polynomial equation; and [A_{1j}, A_{2j}, A_{3j}, A_{4j}] is the corresponding nontrivial solution of the linear homogeneous equations with β_j. With the general solution into constitutive relations (36), the shear stress on x_1–x_2 plane and the electric potential along x_3 direction in piezoelectric crystal substrate can be calculated as follows:

$$
\begin{aligned}
&T_{13} = -k(M_1 R_1 e^{-k\beta_1 x_3} + M_2 R_2 e^{-k\beta_2 x_3} + M_3 R_3 e^{-k\beta_3 x_3} + M_4 R_4 e^{-k\beta_4 x_3}) e^{j(\omega t - k x_1)},\\
&R_i = c_{55}\beta_i A_{1i} + jc_{56} A_{2i} + jc_{55} A_{3i} + je_{15} A_{4i}, i = 1,2,3,4\\
&T_{23} = -k(M_1 S_1 e^{-k\beta_1 x_3} + M_2 S_2 e^{-k\beta_2 x_3} + M_3 S_3 e^{-k\beta_3 x_3} + M_4 S_4 e^{-k\beta_4 x_3}) e^{j(\omega t - k x_1)},\\
&S_i = jc_{41} A_{1i} + c_{44}\beta_i A_{2i} + c_{43}\beta_i A_{3i} + e_{34}\beta_i A_{4i}, i = 1,2,3,4\\
&T_{33} = -k(M_1 T_1 e^{-k\beta_1 x_3} + M_2 T_2 e^{-k\beta_2 x_3} + M_3 T_3 e^{-k\beta_3 x_3} + M_4 T_4 e^{-k\beta_4 x_3}) e^{j(\omega t - k x_1)},\\
&T_i = jc_{31} A_{1i} + c_{34}\beta_i A_{2i} + c_{33}\beta_i A_{3i} + e_{33}\beta_i A_{4i}, i = 1,2,3,4\\
&D_3 = -k(M_1 W_1 e^{-k\beta_1 x_3} + M_2 W_2 e^{-k\beta_2 x_3} + M_3 W_3 e^{-k\beta_3 x_3} + M_4 W_4 e^{-k\beta_4 x_3}) e^{j(\omega t - k x_1)},\\
&W_i = je_{31} A_{1i} + e_{34}\beta_i A_{2i} + e_{33}\beta_i A_{3i} - \varepsilon_{33}\beta_i A_{4i}, i = 1,2,3,4
\end{aligned}
\tag{46}
$$

Compared with (36) for piezoelectric materials, the constitutive equations in regard to $\boldsymbol{u}$ and φ for normal elastic and dielectric materials are in a simple form [1]:

$$
\begin{aligned}
&c_{ijkl}\frac{\partial^2 u_l}{\partial x_j \partial x_k} = (\mu_{ijkl} + j\omega\eta_{ijkl})\frac{\partial^2 u_l}{\partial x_j \partial x_k} = \mu_{ijkl}\frac{\partial^2 u_l}{\partial x_j \partial x_k} + \eta_{ijkl}\frac{\partial^2 \dot{u}_l}{\partial x_j \partial x_k} = \rho_L \frac{\partial^2 u_i}{\partial t^2}\\
&-\varepsilon_{ij}^S \frac{\partial^2 \varphi}{\partial x_i \partial x_j} = 0
\end{aligned}
\tag{66}
$$

where $\boldsymbol{\eta}$ is the dynamic viscosity constant, ρ_L is the density. As an isotropic material, the wave guiding layer in this study has the viscoelastic and permittivity matrices $\boldsymbol{c}$, $\boldsymbol{\varepsilon}$ as that

$$
\boldsymbol{c} = \begin{bmatrix}
c_{11} & c_{12} & c_{12} & 0 & 0 & 0\\
c_{12} & c_{11} & c_{12} & 0 & 0 & 0\\
c_{12} & c_{12} & c_{11} & 0 & 0 & 0\\
0 & 0 & 0 & c_{44} & 0 & 0\\
0 & 0 & 0 & 0 & c_{44} & 0\\
0 & 0 & 0 & 0 & 0 & c_{44}
\end{bmatrix}, c_{ij} = \mu_{ij} + j\omega\eta_{ij}
\tag{67}
$$

$$
\boldsymbol{\varepsilon} = \begin{bmatrix}
\varepsilon_{11} & 0 & 0\\
0 & \varepsilon_{11} & 0\\
0 & 0 & \varepsilon_{11}
\end{bmatrix}
$$

The general solution of $\boldsymbol{u}$ and φ in the wave guiding layer can be expressed as,

$$
\begin{aligned}
&u_i^L = U_i e^{jk\beta_{Li} x_3} e^{j(\omega t - k x_1)}, i = 1,2,3\\
&\varphi^L = \Phi e^{jk\beta_{L4} x_3} e^{j(\omega t - k x_1)}
\end{aligned}
\tag{68}
$$

For 36° *YX*-$LiTaO_3$ substrate, the predominant component of surface acoustic waves has a shear horizontal polarization along the propagation direction. In order to simplify the theoretical model, only particle movement along x_2-axis would be considered in continuous boundary conditions. Substituting (68) into (66), u_2 and φ can be independently calculated as follows:

$$u_2^L = (M_5 e^{jk\beta_{L2}x_3} + M_6 e^{-jk\beta_{L2}x_3}) e^{j(\omega t - kx_1)}$$
$$\varphi^L = (M_7 e^{kx_3} + M_8 e^{-kx_3}) e^{j(\omega t - kx_1)} \tag{69}$$

where

$$\beta_{L2} = \left(\frac{\omega^2 \rho_L}{k^2 c_{44}} - 1 \right)^{1/2} = \left(\frac{\omega^2 \rho_L}{k^2 c_L} - 1 \right)^{1/2} \tag{70}$$

and $M_{5\sim8}$ are the coefficients to be determined by the boundary conditions. For an ideal elastic wave guiding layer ($\eta_L = 0$), β_{L2} expression can be simplified as $\beta_{L2} = (\upsilon^2 \rho_L / \mu_L - 1)^{1/2}$. The shear stress on x_1- x_2 plane along x_2-axis in wave guiding layer can be calculated,

$$T_{23}^L = jk\beta_{L2} c_L (M_5 e^{jk\beta_{L2}x_3} - M_6 e^{-jk\beta_{L2}x_3}) e^{j(\omega t - kx_1)} \tag{71}$$

The Maxwell-Wiechert model is introduced to describe the complex shear modulus of the viscoelastic polymer wave guiding layer. In the linear model for viscoelasticity, the relationship of shear modulus and rate of strain can be described by a spring and a dashpot in series. The total rate of strain contains an elastic part and a viscous part, and a relaxation time $\tau = \eta_0 / \mu_0$ can be introduced. An additional branch that only includes a spring is labeled as an elastic branch, which ensures that the material would eventually return to its original shape rather than result in plastic deformation. As a result, the expression of the shear modulus can be written as [55]

$$c_L = \mu_0 + \sum \mu_n \frac{i\omega\tau_n}{1 + i\omega\tau_n} \tag{72}$$

The viscosity is very small when $\omega\tau_n$ approaches zero or infinity. In this study, this expression with $n = 1$ will be used in (72).

u_2 and φ of the adherent cell layer can be solved in the similar method as follows:

$$u_2^P = (M_9 e^{jk\beta_{P2}(x_3 - h_1)} + M_{10} e^{-jk\beta_{P2}(x_3 - h_1)}) e^{j(\omega t - kx_1)}$$
$$\varphi^P = (M_{11} e^{k(x_3 - h_1)} + M_{12} e^{-k(x_3 - h_1)}) e^{j(\omega t - kx_1)} \tag{73}$$

$$\beta_{P2} = \left(\frac{\omega^2 \rho_P}{k^2 c_P} - 1 \right)^{1/2} \tag{74}$$

where h_1 is the thickness of wave guiding layer, ρ_P and c_P are the density and complex shear modulus of adherent cell layer, respectively. $M_{9\sim12}$ are the coefficients to be determined by the boundary conditions. Similarly, the shear stress on x_1-x_2 plane along x_2-axis in the cell layer can be obtained as,

$$T_{23}^{L} = jk\beta_{P2}c_P(M_9 e^{jk\beta_{P2}x_3} - M_{10}e^{-jk\beta_{P2}x_3})e^{j(\omega t - kx_1)} \tag{75}$$

When a Love wave sensor with a wave guiding layer is used in a vacuum, there is no particle motion but only an electric field existing outside the substrate, and the electric potential tends to be zero when $x_3 \rightarrow \infty$. In this case, the solution for φ in a vacuum is given as that

$$\varphi^{V} = M_0 e^{-k(x_3 - h_1 - h_2)}e^{j(\omega t - kx_1)} \tag{76}$$

where h_1, h_2 are the thickness of wave guiding layer and adherent cells respectively, M_0 is the coefficient to be determined by the boundary conditions.

For a Love wave sensor placed in liquid, a small amount of acoustic wave energy will propagate into liquid medium with a decay length. There are two possible surface conditions for the piezoelectric crystal substrate in a vacuum, free surface or metalized surface. When in a liquid medium, in order to avoid unexpected effects induced by the high dielectric coefficient of liquid medium, the surface of piezoelectric crystal substrate should be metalized, resulting in φ = 0 at x_3 = 0. Au/Cr or Au/Ti films are usually applied in this case to get short-circuited surface. In this case, the velocity field generated in contacting medium by the in-plane oscillation of wave guiding layer is determined by solving the incompressible Navier-Stokes equations [1]

$$\begin{aligned} &\nabla \cdot \boldsymbol{v} = 0 \\ &\rho_M\left(\frac{\partial \boldsymbol{v}}{\partial t} + \boldsymbol{v}\cdot\nabla\boldsymbol{v}\right) = -\nabla p + \nabla\cdot\eta_M(\nabla\boldsymbol{v} + \nabla\boldsymbol{v}^T) \end{aligned} \tag{77}$$

where $\boldsymbol{v}$ represents the fluid velocity, ρ_M, η_M are respectively the density and dynamic viscosity of medium, and p is the pressure. When the velocity initiated by boundary perturbations is

considered small, these nonlinear terms can be eliminated from (77), and the governing equations can be simplified as follows:

$$\begin{aligned} &\nabla \cdot \boldsymbol{v} = 0 \\ &\rho_M \frac{\partial \boldsymbol{v}}{\partial t} = -\nabla p + \nabla \cdot \eta_M (\nabla \boldsymbol{v} + \nabla \boldsymbol{v}^T) \end{aligned} \tag{78}$$

Assuming the general solution of $\boldsymbol{v}$ in a liquid medium as that

$$\upsilon_i^M = U_i e^{-k\beta_{Mi}(x_3 - h_1 - h_2)} e^{j(\omega t - kx_1)}, i = 1,2,3 \tag{79}$$

and substituting (79) into (78), υ_2 can be solved independently from the momentum equation. Correspondingly, a quadratic equation with respect to β_{M2} is obtained. Since part of the surface waves are propagating along the positive direction of x_3, and when $x_3 \rightarrow \infty$, υ_2 tends to be zero, only $k\beta_{M2}$ with positive real part can be adopted, and the solution of υ_2 is as follows:

$$\upsilon_2^M = M_{13} e^{-k\beta_{M2}(x_3 - h_1 - h_2)} e^{j(\omega t - kx_1)}, k\beta_{M2} = \sqrt{k^2 + j\rho_M \omega / \eta_M} \tag{80}$$

M_{13} is the coefficient to be determined by boundary conditions. It is important to note that when k = 0, $k\beta_{M2}$ turns to be $(1+j)(\rho_M\omega/2\eta_M)^{1/2}$. The corresponding decay length δ for (80) can be calculated:

$$\delta = \sqrt{\frac{2}{k^2 + \sqrt{k^4 + \rho_M^2 \omega^2 / \eta_M^2}}} \tag{81}$$

and when k = 0, $\delta = (2\eta_M/\rho_M\omega)^{1/2}$, providing exactly the same decay length expression for TSM wave propagation in a liquid medium [1]. In some previous studies, Love wave propagation was assumed to have similar attenuation as TSM wave propagation along the thickness direction of piezoelectric crystals. Nevertheless, with a large k value, decay length δ in a Love wave sensor is much smaller than that in quartz TSM resonator. Based on (81), δ for the Love wave propagation in water is given in order of ~50 *nm*, which presents high consistency with experimental observations [36]. The shear stress on x_1-x_2 plane along x_2-axis in a liquid medium is also obtained:

$$T_{23}^{M} = -jk\beta_{M2}\eta_{M}M_{13}e^{-jk\beta_{M2}(x_3-h_1-h_2)}e^{j(\omega t-kx_1)} \tag{82}$$

It is well known that for the high-viscosity liquid at high frequencies it might be necessary to consider relaxation effect. The Maxwell model of viscoelasticity assumes a complex viscosity with a characteristic relaxation time as the viscoelastic wave guiding layer discussed above [80]. At low frequencies the liquid behaves as a Newtonian fluid; and at high frequencies it behaves as a solid with shear stiffness. For a cell-based Love wave biosensor, cell culture medium is considered the low-viscosity liquid (η_M < 10 *cp*), and thus only the real part of viscosity would be taken into account.

2.4.2 Determination of Propagation Velocity and Loss in a Layered Love Wave Sensor

As it is shown in previous session, there are a series of undetermined coefficients (M_1, M_2, M_3, M_4, …) in the $\boldsymbol{u}$, φ and $\boldsymbol{v}$ expressions. When a Love wave sensor without adherent cells (h_2 = 0) is used in vacuum, there are two possible surface conditions for the piezoelectric crystal substrate. In the case of free surface, $M_{0\sim8}$ need be determined though 9 independent boundary relations. For 36° *YX*-$LiTaO_3$ substrate, the predominant component of surface particle motion is shear horizontal. In order to simplify our theoretical model, only particle movement along x_2-axis would be considered in continuous boundary conditions. Thus, based on the continuity of displacement, stress, electric potential and electric displacement at contact interfaces,

$$\begin{aligned}
&x_3 = 0, u_2 = u_2^L \Rightarrow M_1A_{21} + M_2A_{22} + M_3A_{23} + M_4A_{24} = M_5 + M_6\\
&x_3 = 0, T_{23} = T_{23}^L \Rightarrow M_1S_1 + M_2S_2 + M_3S_3 + M_4S_4 = -jc_L\beta_{L2}(M_5 - M_6)\\
&x_3 = h_1, T_{23}^L = 0 \Rightarrow M_5e^{jk\beta_{L2}h_1} - M_6e^{-jk\beta_{L2}h_1} = 0\\
&x_3 = 0, \varphi = \varphi^L \Rightarrow M_1A_{41} + M_2A_{42} + M_3A_{43} + M_4A_{44} = M_7 + M_8\\
&x_3 = 0, D_3 = D_3^L \Rightarrow M_1W_1 + M_2W_2 + M_3W_3 + M_4W_4 = \varepsilon_L(M_7 - M_8)\\
&x_3 = h_1, \varphi^L = \varphi^V \Rightarrow M_7e^{kh_1} + M_8e^{-kh_1} = M_0\\
&x_3 = h_1, D_3^L = D_3^V \Rightarrow \varepsilon_L(M_7e^{kh_1} - M_8e^{-kh_1}) = -\varepsilon_0M_0
\end{aligned} \tag{83a}$$

The particle movement along the x_2-axis is dominant compared to the movements in the x_1 and x_3 directions. As a result, additional stress boundary equations are,

$$\begin{aligned} &x_3 = 0, T_{13} = 0 \Rightarrow M_1 R_1 + M_2 R_2 + M_3 R_3 + M_4 R_4 = 0 \\ &x_3 = 0, T_{33} = 0 \Rightarrow M_1 T_1 + M_2 T_2 + M_3 T_3 + M_4 T_4 = 0 \end{aligned} \tag{83b}$$

When the surface of piezoelectric crystal substrate is electrically shorted, the number of unknown coefficients is reduced to 6 ($M_{1\sim6}$). The corresponding independent boundary equations are modified as

$$\begin{aligned} &x_3 = 0, u_2 = u_2^L \Rightarrow M_1 A_{21} + M_2 A_{22} + M_3 A_{23} + M_4 A_{24} = M_5 + M_6 \\ &x_3 = 0, T_{13} = 0 \Rightarrow M_1 R_1 + M_2 R_2 + M_3 R_3 + M_4 R_4 = 0 \\ &x_3 = 0, T_{23} = T_{23}^L \Rightarrow M_1 S_1 + M_2 S_2 + M_3 S_3 + M_4 S_4 = -jc_L \beta_{L2} (M_5 - M_6) \\ &x_3 = 0, T_{33} = 0 \Rightarrow M_1 T_1 + M_2 T_2 + M_3 T_3 + M_4 T_4 = 0 \\ &x_3 = h_1, T_{23}^L = 0 \Rightarrow M_5 e^{jk\beta_{L2} h_1} - M_6 e^{-jk\beta_{L2} h_1} = 0 \\ &x_3 = 0, \varphi = 0 \Rightarrow M_1 A_{41} + M_2 A_{42} + M_3 A_{43} + M_4 A_{44} = 0 \end{aligned} \tag{84a}$$

When a Love wave sensor is moved into a liquid, there is only one possible surface condition, metalized surface. The number of coefficients to be determined turns out to be 7 ($M_{1\sim6}$ and M_{13}) in case of without the adherent cells ($h_2 = 0$), or 9 ($M_{1\sim6}$, $M_{9\text{-}10}$ and M_{13}) in case of with cells ($h_2 \neq 0$). Compared with (84a), the first 4 boundary equations and last one remain the same, and two or four more independent ones should be added accordingly:

$$\begin{aligned} &h_2 = 0: \\ &x_3 = h_1, \upsilon_2^L = \upsilon_2^M \Rightarrow M_5 e^{jk\beta_{L2} h_1} + M_6 e^{-jk\beta_{L2} h_1} = M_{13} \\ &x_3 = h_1, T_{23}^L = T_{23}^M \Rightarrow c_L \beta_{L2} (M_5 e^{jk\beta_{L2} h_1} - M_6 e^{-jk\beta_{L2} h_1}) = -\omega \beta_{M2} \eta_M M_{12} \end{aligned} \tag{84b}$$

$$\begin{aligned} &h_2 \neq 0: \\ &x_3 = h_1, u_2^L = u_2^P \Rightarrow M_5 e^{ik\beta_{L2} h_1} + M_6 e^{-ik\beta_{L2} h_1} = M_9 + M_{10} \\ &x_3 = h_1, T_{23}^L = T_{23}^P \Rightarrow c_L \beta_{L2} (M_5 e^{ik\beta_{L2} h_1} - M_6 e^{-ik\beta_{L2} h_1}) = c_P \beta_{P2} (M_9 - M_{10}) \\ &x_3 = h_1 + h_2, \upsilon_2^P = \upsilon_2^M \Rightarrow M_9 e^{ik\beta_{P2} h_2} + M_{10} e^{-ik\beta_{P2} h_2} = M_{13} / i\omega \\ &x_3 = h_1 + h_2, T_{23}^P = T_{23}^M \Rightarrow c_P \beta_{P2} (M_9 e^{ik\beta_P h_2} - M_{10} e^{-ik\beta_P h_2}) = i\beta_M \eta_M M_{13} \end{aligned} \tag{84c}$$

The combination of (84a) and (84b) or (84c) forms a set of linear homogeneous equations with respect to undetermined coefficients, which are the complete boundary conditions for a cell-based Love wave biosensor in liquid. The equations are given with an $n \times n$ coefficient matrix

form (n is the number of unknown coefficients discussed above for each case). Dispersion relation for this layered Love wave sensor can be obtained by evaluating the propagation velocity υ and attenuation factor α, which can satisfy the determinant of coefficient matrix to be zero. However, since particle motions along x_1, x_3 in the wave guiding layer and liquid medium are neglected, an approximate calculation need be performed instead, in which υ and α are determined to minimize the determinant of coefficient matrix. A series of values of propagation velocity υ and attenuation factor α is tried until the determinant is minimized within the predetermined accuracy. Subsequently, the errors from approximation are also evaluated by comparing the particle displacements in x_1, x_2, x_3 directions at the interface of 36° *YX*-$LiTaO_3$ substrate and wave guiding layer, thus proving the validity of our assumption. After the propagation velocity υ is determined, the electromechanical coupling coefficient K^2 of Love waves generated in 36° *YX*-$LiTaO_3$ substrate with a wave guiding layer can be calculated based on this equation [81]:

$$K^2 = 2 \times \frac{\upsilon - \upsilon_{short}}{\upsilon} \tag{85}$$

where υ, υ_{short} are respectively the propagation velocity with free surface and electrically-shorted surface. The value K^2 indicates the conversion efficiency of electrical energy and mechanical energy to each other in the piezoelectric materials. In addition, the propagation loss per millimeter (*mm*) is given by [65]

$$PL = -0.02\alpha \log e \tag{86}$$

Furthermore, considering a very thin mass loading layer on the surface of wave guiding layer, and assuming it has the same particle motion as that of the wave guiding layer surface, the mass loading is regarded as an acoustically thin and/or rigid layer, and its displacement is

uniform across its thickness. In this case, the boundary equations for T_{23} at $x_3 = h_1$ in (83a) and (84a) should be changed to

$$x_3 = h, T_{23}^L = -\sigma \frac{\partial^2 u_2^L}{\partial t^2} \Rightarrow \mu_L \beta_L (M_5 e^{jk\beta_L h} - M_6 e^{-jk\beta_L h}) = -\frac{j\sigma\omega^2}{k}(M_5 e^{jk\beta_L h} + M_6 e^{-jk\beta_L h}) \tag{87a}$$

and T_{23} in (84b) can be modified as

$$x_3 = h, T_{23}^L - T_{23}^M = -\sigma \frac{\partial^2 u_2^L}{\partial t^2} \Rightarrow \mu_L \beta_L (M_5 e^{jk\beta_L h} - M_6 e^{-jk\beta_L h}) + \frac{j\sigma\omega^2}{k}(M_5 e^{jk\beta_L h} + M_6 e^{-jk\beta_L h}) = -\omega\beta_M \eta \tag{87b}$$

where σ is the surface density of mass layer. Propagation velocity υ' and attenuation factor α' with a mass loading can be acquired based on the modified boundary equations. Compared to that without a mass loading, both propagation velocity and attenuation factor are changed accordingly, indicating an increased kinetic energy contributed as the mass moving synchronously with the wave guiding layer surface. The corresponding mass sensitivity of a Love wave sensor can then be defined from the relative propagation velocity change as follows:

$$S_m^{\upsilon} = \frac{\upsilon' - \upsilon}{\sigma \cdot \upsilon} \tag{88}$$

3.0 AGING-RELATED VISCOELASTICITY CHARACTERIZATION OF TENDON STEM/PROGENITOR CELLS BY A THICKNESS SHEAR MODE RESONATOR

In this chapter, viscoelastic properties of aging and young tendon stem/progenitor cells (TSCs) from rats are characterized by thickness shear mode (TSM) resonators. Acquired admittance spectrums of TSM resonators are sent into a programmed analyzer based on a two-layer-loading transmission line model (TLM), and the corresponding storage modulus G', loss modulus G'', as well as average thickness h_{TSC} for TSC monolayer are obtained. An overall increase in G', G'' and h_{TSC} during aging process can be attributed to the internal dense cytoskeleton, which also induces apparent variations in cell morphologies accordingly. Our results are in agreement with those from other methods, indicating an advisable mechanical measurement technique.

3.1 INTRODUCTION

3.1.1 Tendon Stem/Progenitor Cells

Rats are eukaryotic organisms, and tendon stem/progenitor cells (TSCs) from rats are typical eukaryotic cells as well. In general, a typical animal eukaryotic cell consists of five major structural parts, from outside to inside: an extracellular matrix (ECM), an external plasma membrane, the cytosol interlaced by a cytoskeleton, a variety of membranebounded organelles

suspended in cytosol, and a nucleus to house the DNA [5]. Among them, the cytoskeleton as an intricate 3-demensional array of microfilaments, microtubules and intermediate filaments, helps establish and maintain cell shape. With its support for cellular architecture, the lipid plasma membrane surrounding defines the cell's boundary accordingly. As an information center of a cell, the nucleus directs cellular activities. Relevant cellular functions are localized in suspended organelles in cytosol, such as mitochondria and glycogens. The ECM surrounding cells consists primarily of proteins, providing a structural support between cells or cells and the substrate.

Cell adhesion to a substrate or ECM plays an important role in a variety of cellular activities, such as cell migration, proliferation, differentiation, and tissue formation [5]. Cell-cell or cell-substrate adhesive interactions govern cell aggregation, polarity and migration. Besides, such interactions could alter differentiation of cells by changes in cell morphology, proliferation, as well as programs of gene expression [82]. Generally speaking, the procedure of cell adhesion has three stages: attachment, spreading, and formation of focal adhesions and actin-containing stress fibers [83]. The stage of cell attachment, which involves integrin-ECM protein interactions, is considered as an intermediate state between weak contact and strong adhesion. The attached cells increase their surface contact area with the substrate through cell spreading and the formation of actin microfilaments, and then organize their cytoskeleton by the formation of focal adhesions and actin-containing stress fibers. Focal adhesions, or focal contacts, are the localized points of final attachment between cell surface and substrate [5]. For adherent cells on the substrate, focal adhesion contains clustered adhesion receptors, integrins, which span the plasma membrane and attach to other proteins both outside and inside the cell: to the outside, integrins attach to ECM proteins; to the inside, they interact with bundles of actin microfilaments via a few linker proteins. This intrgrin-dependent attachment enhances cell adhesion to the

substrate, functioning as not only the structural link between the cytoskeleton and ECM, but also the triggering signal pathway that directs cell functions. For an adherent cell, with the formation of focal adhesions, the cytoskeleton is anchored with ECM or substrate finally. Thus, the ECM, cytoskeleton, as well as the lipid membranes together make up to be the most crucial factor of viscoelasticity of adherent cells. Besides, the gel-like plasma (including cytoplasmic proteins and organelles) around the cytoskeleton also has an influence on cell viscoelasticity.

In addition to those common characteristics of eukaryotic cells discussed above, TSCs also possess their own distinct properties as one kind of stem/progenitor cells in tendons. Tendon is fibrous connective tissue that transmits muscular force to bone thus enabling joint motion and body movement. For a long time tendon had been considered to contain only tenocytes. However, some recent studies demonstrated that human, rat and mouse tendons also contain multi-potent adult stem cells, termed tendon stem/progenitor cells [84, 85]. Compared with tenocytes, TSCs exhibit distinct properties in various aspects, including cell morphology, marker expression, as well as proliferation and differentiation potential [86, 87]. Previous research revealed that appropriate stimulus could direct cellular differentiation and promote ECM development [88, 89]. Likewise, in proper circumstances differentiation of TSCs into active tenocytes could be stimulated as well, which is beneficial for maintaining tendon homeostasis. Nevertheless, excessive, improper stimulation is detrimental, as it induces differentiation of TSCs towards non-tenocyte lineages of cells, such as adipocytes, chondrocytes and osteocytes [90]. Rui *et al.* reported that repetitive tensile loading increased the expression of BMP-2, which could enhance osteogenic differentiation of TSCs [91]. Therefore, the potential of differentiation and proliferation of TSCs would be induced in certain circumstances, causing favorable or unfavorable effects on tendon functions. In order to improve the possibility of using TSCs and to

repair or regenerate injured tendons effectively, TSCs' behaviors, including their migration, differentiation and proliferation need be examined in detail. It is known that aging leads to a decline in the functional competence of human body and also degenerative changes in tendons [92]. At the cellular level, Zhou *et al.* reported that aging TSCs could decease proliferation rate, delaye cell cycle progression and alter cell fate patterns [93]. Presently, most studies concerning TSC aging focus on proliferation and differentiation, while discussions on fundamental mechanical properties, such as elasticity, viscosity and Poisson's ratio, are quite limited. Changes in viscoelasticity during the aging process of TSCs should be investigated as an essential parameter, and the results from such studies could contribute immensely to the aging-related treatment of tendon injury.

3.1.2 Viscoelasticity Characterization of Cells

So far, a variety of measurement methods have been developed for detection of cellular viscoelasticity, for example, magnetic bead microrheometry (MBM), atomic force microscopy (AFM), microplate manipulation, microfluorimetry and so on [10, 13, 18, 19, 94, 95]. Most of them (except microfluorimetry) need apply an external force on the individual cell in an invasive manner. For MBM, the diameter of ferrimagnetic microbead is approximately $1 \sim 5\ \mu m$, while the normal radius of AFM probe is even under $1\ \mu m$. As a result, it is difficult for these methods to present statistical results, although local measurement can be conducted on some specific parts of cells. Meanwhile, measurement process of these methods is also time consuming. In comparison, micofluorimetry as a non-invasive technique can provide relevant mechanical property measurement of cell group, but only limited to cellular viscosity. Due to its high sensitivity, simple structure, and easy interconnection with electronic measurement systems,

quartz TSM resonator has been applied to characterize the viscoelastic properties of materials bounded on its surface [33, 74]. When cell monolayer adheres on its surface, the electrically-excited acoustic-wave propagation can change accordingly through entire quartz crystal, allowing a simple, quantitative and non-invasive method to extract the complex shear modulus of adherent cells.

3.2 MATERIAL PREPARATION AND EXPERIMENTAL DETAILS

3.2.1 Isolation and Culture of Tendon Stem/Progenitor Cells

We isolated TSCs from the Achilles tendons of both old rats (20 month, 300~350 *g*) and young rats (8 week, 200~250 *g*). Briefly, the middle portion of tendons was retrieved by cutting the tendon samples 5 *mm* from the tendon-bone insertion and tendon-muscle junction. After removing the tendon sheath and surrounding paratenon, the middle tendon portion tissues were weighed and minced into small pieces (1 *mm* × 1 *mm* × 1 *mm*). Each 100 *mg* tissue sample was digested with 3 *mg* collagenase type I (Life Technologies, Carlsbad, CA, USA) and 4 *mg* dispase (Stemcell Technologies, Vancouver, BC, Canada) in 1 *ml* phosphate-buffered saline (PBS, Mediatech Inc., Manassas, VA, USA) at 37°C for 1 *hr*. The suspensions were centrifuged at 1500 G for 15 *min*, and the cell pellet was resuspended in growth medium consisting of Dulbecco's modified Eagle's medium (DMEM, Lonza, Walkersville, MD, USA) containing 20% fetal bovine serum (FBS, Atlanta Biologicals, Lawrenceville, GA, USA), 100 *U/ml* penicillin, 100 $\mu g/ml$ streptomycin, and 2 μM glutamine (Thermo Fisher Scientific Inc., Waltham, MA, USA). A single-cell suspension was obtained by diluting the suspension to 1 cell/μl and then

cultured in T25 flasks at 37°C with 5% CO_2. After 8~10 days in culture, colonies formed as the Achilles TSCs were visible on the surface of culture flask. Individual cell colonies were collected using trypsin (Life Technologies, Carlsbad, CA, USA) and transferred to separate T25 flasks for further culture.

3.2.2 Measurement and Characterization of Tendon Stem/Progenitor Cells

Fig. 10 schematically shows the measurement system of 10-*MHz* TSM resonator (International Crystal Manufacturing, Oklahoma City, OK, USA) for TSCs. The diameter of TSM resonator's central circle electrode was 5.10 *mm*. One tube (6.20 *mm*/8.00 *mm* × 6 *mm*) of poly(dimethylsiloxane) (PDMS, Dow Corning, Midland, MI, USA) was located around the upper electrode, forming the well-like structure for TSC culture. The admittance spectrum of TSM resonators was obtained using an Agilent 4294A Precision Impedance Analyzer (Agilent Technologies, Palo Alto, CA, USA). In sweep signaling, frequency step was set as 20 *Hz*, and driving voltage was 500 *mV*. For different TSM resonators in varied conditions, the sweep frequency range was adjusted within 9.96 ~ 10.00 *MHz*. Prior to the measurements, TSM resonators with empty wells were sterilized overnight by exposure to UV light. Subsequently, the entire electrode surface of TSM resonators was coated with collagen by incubating the well with 100 μl 100 $\mu g/ml$ collagen type I (Stemcell Technologies, Vancouver, BC, Canada) in PBS for 2 *hr*. After washing these wells three times in PBS, they were refilled with 100 μl 1.0×10^5 *cell/ml* TSC suspensions from old and young rat Achilles tendons. TSM resonators were maintained in an incubator at 37°C with 5% CO_2 for 12.5 *hr*, and the corresponding admittances were detected every 1 *min*. In addition, the initial admittances of unloaded TSM resonators as well as TSM resonators with culture medium and collagen coating were also recorded for further extraction of

TSCs' viscoelastic properties. All measurements were performed three times. After measurements, TSM resonators were removed from the measurement system. TSCs on the electrodes of TSM resonators were then fixed with 4% paraformaldehyde in PBS and treated with 0.1% Triton X-100 for 10 *min* before staining the nuclei with DAPI (1:5000). Washed three times in PBS, these stained TSCs were examined by fluorescence microscopy (Eclipse TE2000-U, Nikon, Japan).

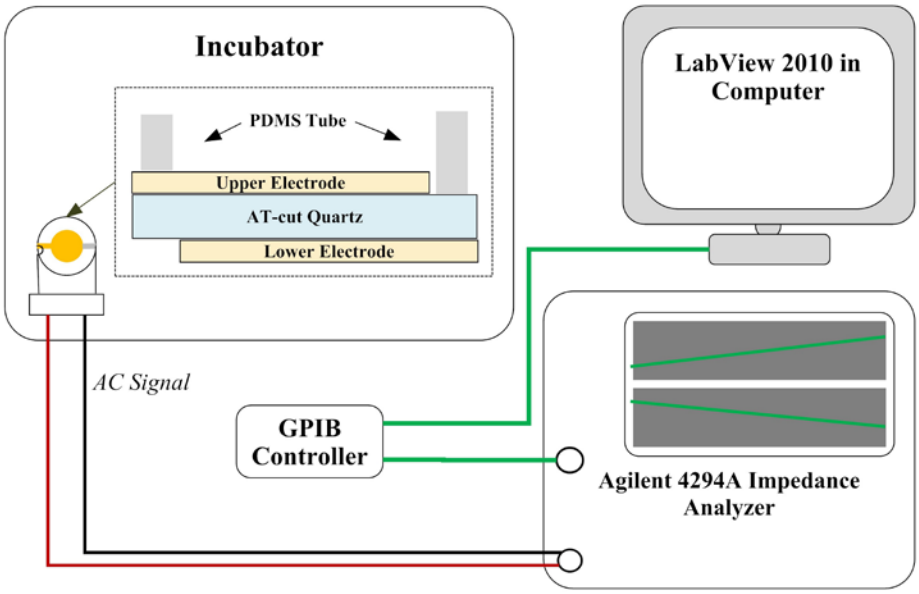

Figure 10. Schematic diagram of the TSM resonator measurement system

In parallel experiments, identical dose of TSC suspensions were cultured in collagen-coated 96-well culture plate and PDMS wells on Au/Si wafer. After 12 *hr*, the morphologies of TSCs were observed through phase-contrast microscopy (Eclipse TS100, Nikon, Japan) and scanning electron microscopy (XL-30 FEG SEM, FEI/Philips, Japan, accelerating voltage: 5 *kV*), respectively. Then, TSCs in 96-well plate were also fixed with 4% paraformaldehyde in PBS and

treated with 0.1% Triton X-100 for 10 *min*. Fluorescein phalloidin in methanol was applied at a dilution ratio of 1:40 for 20 *min* for actin staining, and these stained TSCs were examined by fluorescence microscopy as well after washing.

3.3 THEORETICAL MODEL AND ANALYTICAL METHODS

Following the modified TLM introduced in Chapter 2, parameter calibration of unloaded TSM resonator plays an important role in compensating additional effects from Au or Pt electrodes, protein coating and other perturbations. Table 4 lists the extracted effective parameters (h_q, μ_q, C_0 and C_p) for unloaded TSM resonator and TSM resonator with collagen coating, where those effects are considered as the intrinsic characteristics of TSM resonator itself. Both fitting are well-acceptable with the error of 0.0372% and 0.0280%, leading to the affirmative effective parameters of TSM resonator. From Table 4, it can be seen that the effective TSM thickness is slightly larger than the theoretical value 165 μm, and quartz viscosity is also increased compared with the reference value 0.00035 $Pa{\cdot}s$ [31]. In the meantime, it is illustrated that collagen absorption does not cause evident changes in calibrated TSM parameters, when only external capacitance C_p increasing to some extent. Simplified two-layer-loading model for TSC adhesion is confirmed further from this perspective, and all these parameters given in Table 4 will be used in following fitting calculation.

Prior to the extraction of TSC complex shear modulus, complex impedance of culture medium should be acquired. Conducting the Regula-Falsi iteration method and error comparison, optimal solution is obtained:

$$Z_{Med} = (1+j)A\sqrt{(0.5696+0.1888j)\omega}$$

With (1) the calibrated effective parameters for TSM resonator with collagen coating, (2) the complex impedance of culture medium, as well as (3) the admittance spectrum $Y(\omega_i) = G(\omega_i) + jB(\omega_i)$ for TSM resonator with TSC adhesion, the specific solution of complex shear modulus $G_{TSC} = G' + jG''$ and average thickness h_{TSC} of TSC monolayer can be determined based on the similar algorithm.

Table 4. Calibrated parameters of TSM resonator

Effective Parameters	Unloaded TSM Resonator	TSM Resonaotr with Collagen
Thickness of TSM h_q	166.39 μm	166.39 μm
Viscosity of Quartz μ_q	0.0416 $Pa{\cdot}s$	0.0402 $Pa{\cdot}s$
Static Capacity of TSM C_0	4.5884 pF	4.5940 pF
External Capacity of TSM C_p	6.8496 pF	7.4308 pF

3.4 RESULTS AND DISCSSIONS

3.4.1 Tendon Stem/Progenitor Cells Adhesion on the Substrate

Fig. 11 presents the resonance frequency variation of TSM resonators during TSC adhesion: (a) is for TSCs from old rats and (b) is for TSCs from young rats. The insets are their corresponding admittance spectrum sets, where the resonance frequencies are collected. The spectrum recording endures for 12.5 *hr*. As the time goes on, the color of admittance spectrums in plots is shifting from pink to black gradually. It is illustrated that with the adhesion of both aging and young TSCs, the intensity of resonance peaks is decreasing gradually, and the FWHM (Full Width at Half Maximum) tends to be larger. The resonance frequencies extracted from these resonance

peaks exhibit similar variation tendency for both aging and young TSCs as well. As it is marked, the entire frequency variation during TSC adhesion experiences three regions: I rapid decrease, II reverse increase, and III slow decrease to be stable. The main differences between (a) and (b) are merely expressed in the time distributed in three regions, as well as magnitude of frequency variation. As introduced in Session 3.1.1, the procedure of cell adhesion has three stages: attachment, spreading, and formation of focal adhesions and stress fibers. In our experiments, the Au/Cr electrode surface is pre-coated with collagen, which is considered a primary and structural part of ECM in tendons [5]. When suspending cells are approaching to the substrate, these ECM proteins are bound by integrin receptors composed of α/β chains, which span the plasma membrane [82, 96]. Receptor-ligand binding induces initial attachment, and then TSCs undergo the following two stages successively. As it is shown in Fig. 11, in the beginning there is an obvious decease in resonance frequency of TSM resonators with a great number of TSCs falling down and attaching on electrodes. With more and more TSCs finishing attachment, TSC spreading becomes the predominant behavior, resulting in a reverse increase of resonance frequency in region II. As the reorganization of cytoskeleton and formation of focal adhesion, resonance frequency of TSM resonators is decreased slightly in region III. With decreasing tendency in region III is eliminating and the variation curve is stable, all TSCs in medium are considered adhered to the surface of electrodes completely. In this case, the admittance spectrum acquired after 11 *hr* can be adopted for TSC monolayer characterization.

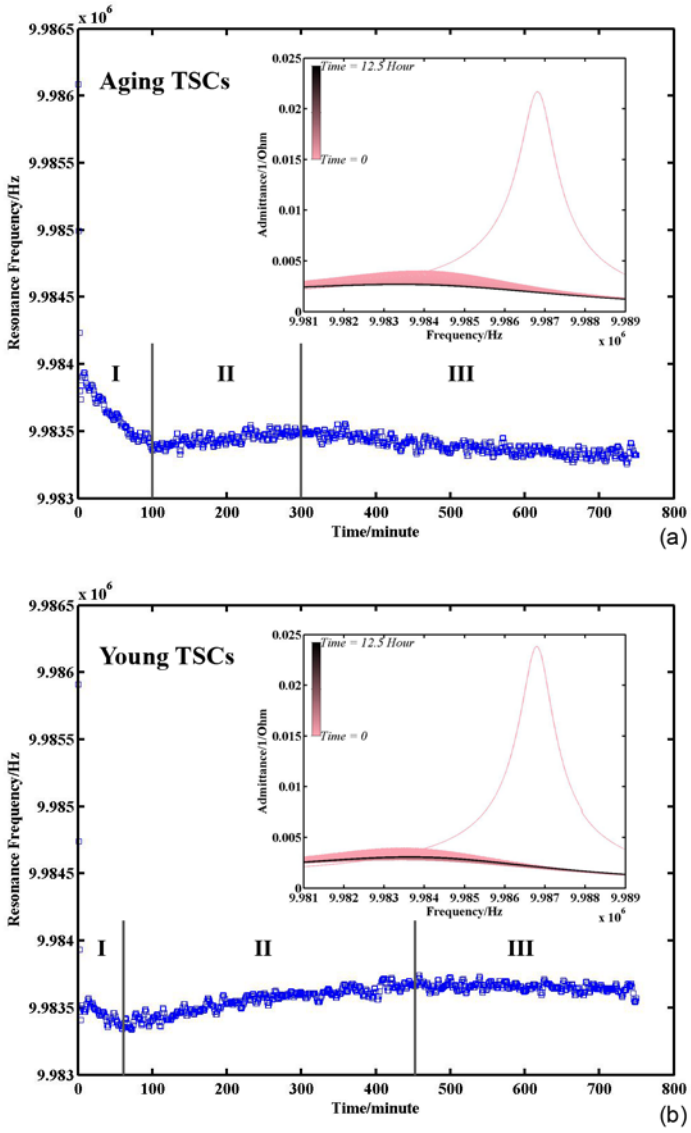

Figure 11. Resonance frequency of TSM resonators with TSC adhesion (insets are corresponding admittance spectrum sets)

Fig. 12 shows TSCs' microscopy photos after cell suspension is kept in wells for 12 *hr*: (a) ~ (b) are for TSCs from old rats, and (c) ~ (d) are for TSCs from young rats. (a), (c) are obtained by phase-contrast microscopy, where cell suspension is added into 96-well plate. Both aging and young TSCs adhere and form relatively-uniform cell monolayer as assumed in the

theoretical model. There is no obvious overlap or blank space on the substrate, leading to an appropriate assumption in the following calculation. Meanwhile, the TSCs on the electrodes of TSM resonators are nuclei stained and observed through fluorescence microscopy (Fig. 12(b), (d)). As that in 96-well plate, TSCs seeded into PDMS wells exhibit the similar consistency and uniformity, indicating TSC monolayer an isotropic, homogeneous layer further. Nevertheless, it also illustrates quite different morphologies between aging and young TSCs. As shown in (a), (c), compared to young TSCs with characteristic elongated shape as fibroblasts, aging TSCs possess enlarged, flat, polygonal cell shape, extending without any specific directions. There are obvious changes in TSC morphologies during aging process, which will be discussed later.

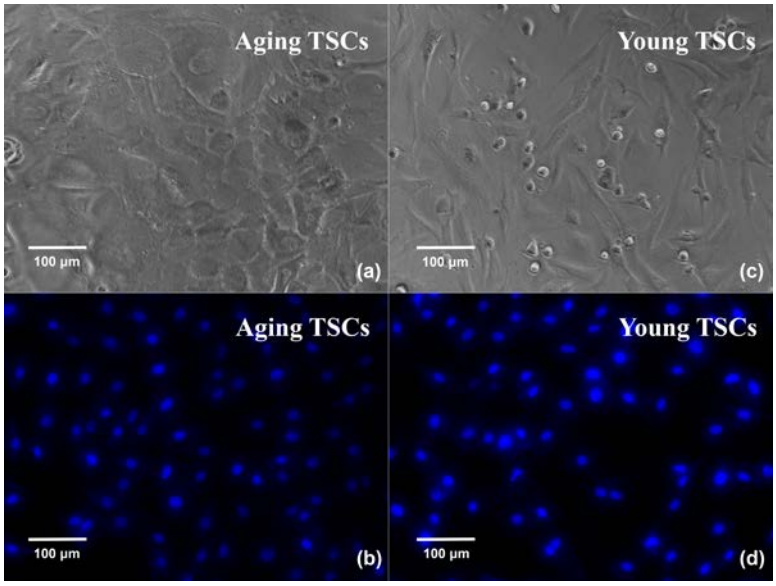

Figure 12. Phase-contrast and fluorescence (nuclei staining) photos of TSCs

3.4.2 Viscoelasticity of Tendon Stem/Progenitor Cells

Based on the multilayer loading model introduced previously, the corresponding programmed analyzer is built up for extraction of TSCs' viscoelastic properties. Assuming TSC monolayer as an isotropic, homogeneous loading layer, its equivalent density is required in this algorithm. As it is known, a typical animal eukaryotic cell consists of five major structural parts, from outside to inside: ECM, an external plasma membrane, the cytosol interlaced by a cytoskeleton, a variety of membranebounded organelles suspended in cytosol, and a nucleus to house the DNA [5]. Thus, three equivalent densities of TSC monolayer are adopted: 1.20 g/cm^3, 1.10 g/cm^3 and 1.00 g/cm^3. For the primary component of ECM and cytoskeleton is a variety of protein fibers, such as collagen, actin and fibrin, a theoretical protein density of 1.20 g/cm^3 is chosen as the upper limit [97]. Meanwhile, assuming the plasma as special protein solution, the density of pure water, 1.00 g/cm^3, is accepted as the lower limit.

Sending the admittance spectrum acquired between 11.5 *hr* and 12.5 *hr* to the analyzer, a series of complex shear modulus of TSC monolayer G', G'' as well as average thickness h_{TSC} are obtained. Fig. 13 gives the statistical results of G', G'' and h_{TSC} for aging and young TSCs, and the fitting-error analysis in extraction procedure is shown in Fig. 14. Fig. 14(a), (b) are representative comparison between experimental and fitting curves of $Y = G + jB$, where Y is the admittance spectrum collected after 12 *hr*. The error upper limit is set as 1% in algorithm. Much smaller than this setting point, the fitting-error results for both aging and young TSC monolayer are stabilized under 0.1%, indicating certainty and reliability of extracted G' and G'' in Fig. 13. G', G'' and h_{TSC} from different equivalent densities of TSC monolayer are marked in Fig. 13, respectively. It is illustrated that G' and G'' present similar increasing tendency as equivalent density is decreasing, and the corresponding thickness is also rising as a result of near-constant

mass load. Shear modulus G' and loss modulus G'' of aging TSCs increase from 18030 ± 171 *Pa* to 21608 ± 205 *Pa* and from 113654 ± 348 *Pa* to 136209 ± 422 *Pa*, respectively, with the adopted density decreasing from 1.20 g/cm^3 to 1.00 g/cm^3. In the meantime, the average thickness of TSCs increases gradually from 320.56 ± 3.42 *nm* to 384.23 ± 4.13 *nm*. Comparing the viscoelastic properties of aging and young TSCs, the aging TSCs possess larger storage modulus and loss modulus, as well as an increased average thickness. The storage modulus of aging TSCs is over ten times than that of young, revealing an obvious increase in stiffness of TSCs from young to aging. In the case of 1.10 g/cm^3, storage modulus G' of aging and young TSCs are 19658 ± 187 *Pa* and 824 ± 13 *Pa*, respectively. In comparison, the loss modulus exhibits a relatively slight increase: with 1.10 g/cm^3 as preset density, G'' for aging and young TSCs are 123910 ± 383 *Pa* and 105915 ± 363 *Pa*, respectively. Besides, the corresponding thickness h_{TSC} of aging TSC monolayer is 349.47 ± 3.78 *nm*, which is approximately 15% larger than that of young (298.32 ± 4.39 *nm*). These differences between aging and young TSCs have an important relation with their architecture. In order to get more details concerning cellular architecture, including cytoskeleton organization and adhesion thickness, TSCs are detected by both SEM and fluorescence microscopy shown in next session.

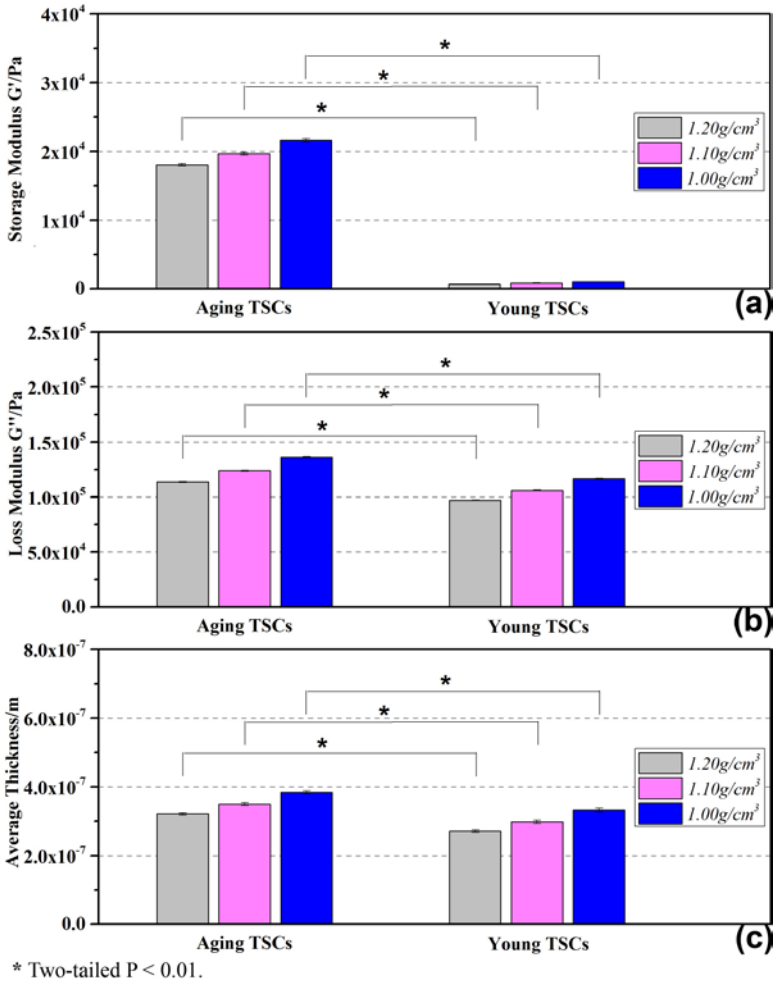

Figure 13. Complex shear modulus and average thickness of TSCs

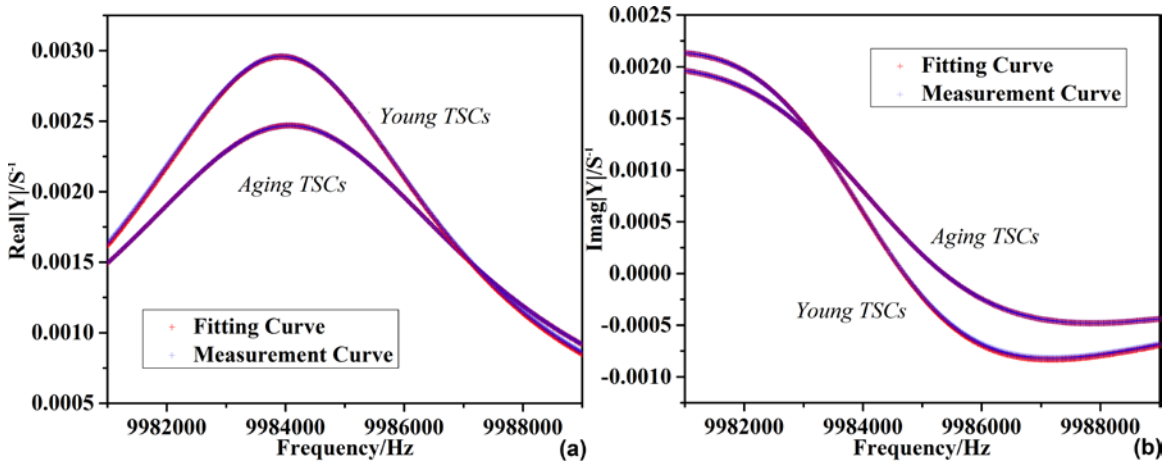

Figure 14. Admittance spectrum fitting of TSM resonator with TSC adhesion

3.4.3 Cytoskeleton of Tendon Stem/Progenitor Cells

Fig. 15 are SEM ((a) ~ (c), (e) ~ (f)) and fluorescence ((d), (g)) photos: (a) is the cross-section observation of aging TSCs; (b), (c) present the adhesion pattern of aging TSCs when (e), (f) of young TSCs; and (d), (g) describe the internal actin cytoskeleton of aging and young TSCs. It can be seen that TSC monolayers are uniform and compact across the entire surface as in Fig. 12, without any obvious overlap or uncovered space. The relatively low roughness is in good agreement with our presupposition, guaranteeing an affirmative fitting in TLM analysis. Fig. 15(b), (c), (e) and (f) reveal morphology details of adherent TSCs on electrodes. For aging TSCs, cell spreading is extending from spherical membrane in random directions, forming an irregular polygonal circumference. Comparing with this large, flat cell shape, young TSCs tend to spread along a specific direction to form an elongated, slender shape. The lamellipodium and filopodium are often observed along the edge of two polar of young TSCs, while no similar phenomenon is found in aging ones. As it is known, with TSCs spreading, actin microfilaments are formed extensively in cells, and then cellular cytoskeleton based on actin-containing stress fibers are organized and linked with ECM, establishing and supporting cell shape. The distribution of primary component of cellular cytoskeleton, actin microfilaments in both aging and young TSCs, which cell morphologies are strongly dependent on, are shown in Fig. 15(d), (g). It is illustrated that numerous actin microfilaments are occupying most of the cytoplasmic area in both aging and young TSCs. However, compared with discrete, flocculent ones in young TSCs, actin microfilaments in aging TSCs tend to form long, filamentous bundles: some are closely parallel along one certain direction, as another set of parallel bundles cross them in different direction. There is a considerable increase in the number and individual size of actin microfilaments during aging of TSCs, when similar conclusions have been drawn on other

general fibroblasts. Wang *et al.* reported increased organization of cytoskeleton in aging human dermal fibroblasts, which was considered as a result of an increasing in the abundance of cytoplasmic filaments [98]. Hereafter, Nishio *et al.* suggested further that overproducing of vimentin filaments in skin fibroblast cytoskeleton resulted in senescent cell morphologies [99, 100]. Schulze proposed in vivo aging process, the cytoskeletal polymers showed a shift from monomeric G-actin to polymerized, filamentous F-actin, but no significant changes in vimentin and microtubule content [101]. Fluorescence analysis provides an explanation that aging TSCs possess a dense cytoskeleton organization compared to young TSCs, which causes the former increased cell size and irregular cell shape. For aging TSCs, the dense cytoskeleton could be attributed to overproducing of actin microfilaments and some other specific protein, aggregation or mutation. Considering cytoskeleton as the structural and supportive component, its inherent variations not only lead to an apparent increasing in average thickness of TSC monolayer, but also induce both stiffness and viscosity to increase during aging process.

3.4.4 Comparison of TSM Resonator with Other Measurement Methods

From Fig. 15(a) the average thickness h_{TSC} of aging TSC monolayer is obtained as approximately 400 *nm*, exhibiting great consistence with theoretical model (h_{TSC} = 384.23 ± 4.13 *nm* with density of 1.00 g/cm^3). Thus, SEM photos confirm reliability of our extracted results further. In the case of 1.00 g/cm^3, the viscoelasticity of aging and young TSCs are 21608+136209*j* and 985+116582*j Pa* respectively. Using $\eta = G''/\omega$, effective viscosity of them are obtained as 2.17 and 1.86 *cp*. Comparing with cell viscoelasticity by other techniques, including MBM, AFM, microplate manipulation and microfluorimetry shown in Table 5, our result could reach agreement by different extent, even though various cell types, and local measurement on the

individual cell conducted in most methods. According to viscoelasticity theory, complex shear modulus $c_P = G' + jG''$ is dependent on oscillation frequency ω. Their relation is described in power-law structural damping model functionally as that

$$c_P = G_0(1 + j\chi)(f / f_0)^{\gamma}\Gamma(1-\gamma)\cos(\pi\gamma/2) + j\mu f \tag{89}$$

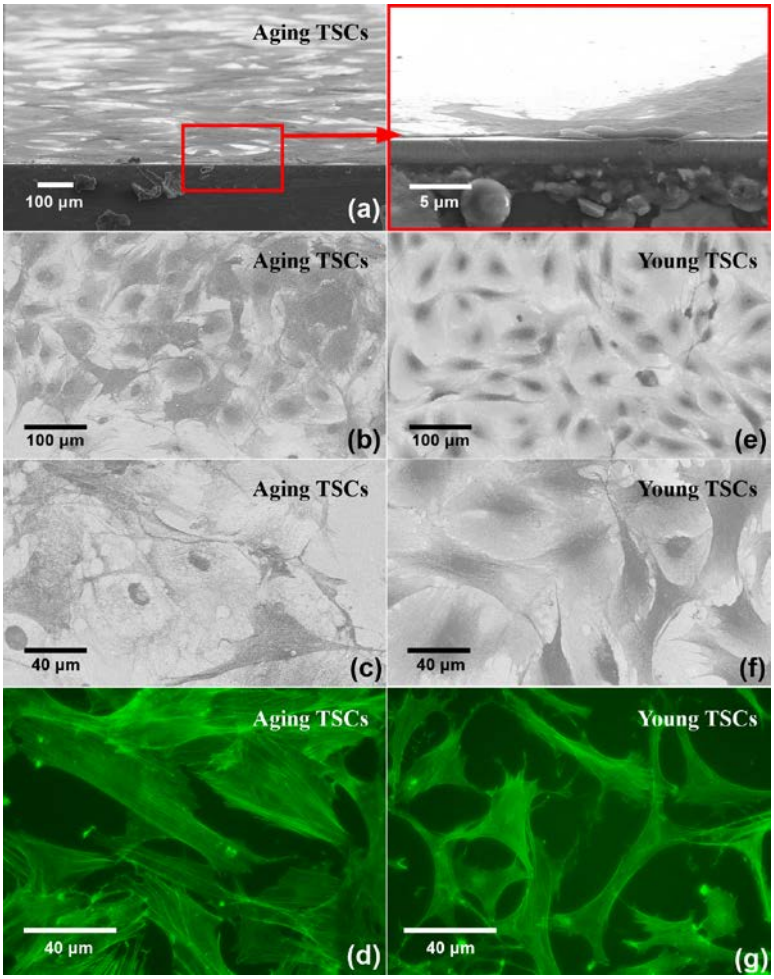

Figure 15. SEM and fluorescence (actin staining) photos of TSCs

where G_0 is a modulus scale factor, f_0 is a frequency scale factor, γ is the power-law exponent usually assigned in 0.10-0.16, χ is structural damping coefficient related to γ by $\chi = \tan(\pi\gamma/2)$, and μ is Newtonian viscous damping coefficient [9, 19]. With γ of small values, the factor $\Gamma(1-\gamma)\cos(\pi\gamma/2)$ is close to unity and so (89) can be simplified as

$$c_P = G_0(1 + j\chi)(f / f_0)^{\gamma} + j\mu f \tag{90}$$

Thus, as G_0 = constant, $G' \propto f^{\alpha}$. When γ is assigned with 0.12, storage modulus G' of aging and young TSCs at 160 *Hz* is calculated as 5744 and 262 *Pa*, respectively. When γ = 0.14, G' turns out to be 4606 and 210 *Pa*. The shear modulus G' of young TSCs transformed at low frequency is of the same order magnitude with results for 3T3s by AFM and chick fibroblasts by microplate method [8, 11, 102], and G' of aging TSCs transformed at low frequency keeps consistent order with that of 3T3 fibroblasts from analysis of magnetic bead microrheometry as well [17]. From this perspective, it is indicated that storage modulus G' of TSC monolayer could reflect shear stiffness of individual cell to some extent. Meanwhile, due to quite similar measurement conditions (non-invasive, group test, at high frequencies), our viscosity results reach good agreement with that from microfluorimetry [103]. In comparison, η of fibroblasts by other techniques at low frequencies appears to be several orders of magnitude larger [8, 11, 17, 102]. This frequency-dependent variation matches power-law structural damping model partially while $\eta \propto f^{\gamma-1}$ as G_0 = constant and viscous damping coefficient μ is ignored. In fact, there are obvious differences in η among these low-frequency, local measurement methods, suggesting significant effect of measurement environment on loss modulus G'' at low frequencies. With frequency-dependent relation is eliminated at high frequencies and μ becomes the dominant factor, the TSM measurement could obtain relatively non-mutative, stable viscosity as microfluorimetry. Therefore, G' and G'' as statistical stiffness and viscosity of TSC monolayer,

could exhibit characteristic viscoelasticity of individual TSC in a group, and at the same time avoid too much fluctuations from individual differences. In addition, because of the stable, average, statistical features of TSM measurements, the differences of viscoelasticity between aging and young TSCs can also be amplified appropriately compared with that expressed by other techniques, implying a potential of TSM technique for mechanical property mark. Through high-frequency TSM measurement, the reliable and repeatable complex shear modules of cell monolayers with various cytoskeleton organizations are provided in an economic, simple, invasive manner. Meanwhile, the average thickness of cell monolayer, as a reflection of cell size, could be obtained with viscoelastic properties, which cannot be realized in other techniques. According to variations in shear modulus of cell monolayer, as well as average thickness, internal architecture of cell could be deduced and corresponding status in a variety of procedures (contractility, proliferation, differentiation, etc.) be acquired.

Table 5. Comparison of fibroblast viscoelasticity by different measurement methods

Method	**Cell Type**	**G′/*Pa***	**Viscosity/*cp***	**Measuring Frequency/*Hz***	**Local Measurement**	**External Force**	**Ref.**
MBM	NIH 3T3	2×10^3~4×10^3	2×10^3	-	Yes	Yes	[17]
AFM	3T3	200-715	100-500	50-300	Yes	Yes	[8, 102]
Microplate Manipulation	Chick Fibroblast	600~1000	1×10^7	-	Yes	Yes	[11]
Microfluorimetry	Swiss 3T3	-	1.1±0.2	5 M~200 M	No	No	[103]

3.5 CONCLUSIONS

In this chapter, the quartz TSM resonator is adopted to extract the complex shear modulus of adherent TSC monolayer owing to its high sensitivity, repeatability and easy connection with electrical measurement systems. 100 μl 1.0×10^5 *cell/ml* TSC suspensions from old and young rats are added respectively, and the corresponding admittances are detected every 1 *min*. Sending the admittance spectrums acquired between 11.5 *hr* and 12.5 *hr* to an analyzer, which is established based on a two-layer-loading TLM, a series of complex shear modulus of TSC monolayer G', G'' and average thickness h_{TSC} are obtained. The results show an overall increase in storage modulus, loss modulus, as well as average thickness during aging process. The storage modulus of aging TSCs is over ten times than that of young, revealing an important rise in stiffness of TSCs. Meanwhile, both phase-contrast and SEM photos present enlarged, flat and heterogeneous cell shape for aging TSCs when young TSCs possess general elongated, slender shape. Increased cell size and irregular cell shape is attributed to the dense cytoskeleton organization, which induces both stiffness and viscosity to increase. Our results concerning TSC monolayer are agreeable with those obtained through other techniques, including MBM and AFM. These results identify an economic, non-invasive, promising method to measure viscoelastic properties of TSCs, which could contribute to aging-related treatment of tendon injury. Furthermore, viscoelasticity changes reflect internal cytoskeleton variations that are also involved extensively in a series of cell activities, such as contractility, proliferation, and differentiation. The reliable and repeatable complex shear modulus of cells is provided by TSM resonators, indicating a potential biophysical marker during not only aging process but also other cell activities.

4.0 REAL-TIME MONITORING THE ACTIVATION PROCESS OF PLATELETS USING A THICKNESS SHEAR MODE RESONATOR

In this chapter, the thickness shear mode (TSM) resonator is adopted to monitor activation process of platelets. Using fibrinogen-coated electrodes for platelet adhesion and thrombin for platelet activation, the electrical admittance spectrums during the entire process are recorded. The acquired electrical admittance is processed by a programmed analyzer based on a two-layer-loading model, and the corresponding storage modulus G′, loss modulus G″, as well as average thickness hPL of platelet monolayer at a series of time points are obtained. Our findings show that G', G'' and h_{PL} can provide useful quantitative measures on platelet structure variations in activation process, indicating potential of TSM resonators in characterization of platelets.

4.1 INTRODUCTION

4.1.1 Platelets and Platelet-rich Plasma

Compared with TSCs, platelets from rats' blood are not considered as typical eukaryotic cells since there are no nuclei in them. Whole blood is mainly composed of plasma and three kinds of cells: leukocytes (white blood cells), erythrocytes (red blood cells) and thrombocytes (platelets). Plasma is a pale-yellow liquid that normally holds the blood cells in suspension. It also contains

plasma protein and other materials, including a series of dissolved nutrients and waste products. Resting platelets in plasma are small (2 ~ 3 μm), anucleate, disc-shaped cells. A platelet contains a number of distinguishable structural elements including: a delimited plasma membrane, invaginations of the surface membrane that form the open canalicular system (OCS), a closed-channel network of residual endoplasmic reticulum that form the dense tubular system (DTS), a spectrin-based membrane skeleton, an actin-based cytoskeletal network, a peripheral band of microtubules and numerous organelles in a sol-gel zone [104].

As one of major components in blood, platelets play a critical role in a number of pathophysiological processes, including hemostasis, hemorrhage, inflammation and cancer [104]. During normal hemostasis, when the damaged vessel wall exposes collagen and basement membrane proteins, platelet adhesion to the substrate is initiated by platelet rolling. The adherent platelets aggregate gradually and are activated to release activation mediators, such as ADP and thromboxane A2. Following activation, the platelets produce thrombin, catalyzing the initiation of coagulation cascade, which generates a mesh-like fibrin deposit in the end [105]. The platelet membrane is densely packed with highly specific surface receptors, which could finely regulate signal-dependent platelet activation in coagulation, inflammation, angiogenesis as well as wound repair. During normal hemostasis, platelet receptor-ligand interactions play an important role in a series of platelet activities, including recruitment, adhesion, and aggregation. Major receptors (GPIb-IX-V, αIIbβ1, $\alpha 2\beta$1, GPVI, etc.) have a direct role in this process, either in activating platelets or as adhesive receptors interacting with damaged cell walls or with other platelets to contribute to thrombus formation. Meanwhile, there are evident differences among them in both positive and negative feedback loops in hemostasis process, emphasizing their significance in platelet functions and in the ways that platelets adapt their function to different situations [106].

The matrix inside platelets resembles a liquid gel called sol–gel zone [104]. Critical components of platelet cytoskeleton includes, from the plasma membrane inward, a spectrin-based skeleton that is adherent to the cytoplasmic side of plasma membrane, a microtubule coil that runs along the perimeter and thus lines the thin axis of the cell, and a rigid network of cross-linked actin filaments that fills the cytoplasmic space of the cell. Actin is the most abundant of all the platelet proteins, and actin filaments are also primary component in platelet cytoskeleton. As is introduced in TSCs part, for a eukaryotic cell, cytoskeleton in cytoplasm is involved in cellular contraction and motility, establishing and supporting cellular architecture. Changes in the state of polymerization and movement of these fibrous components of the matrix are intimately related to cellular internal contraction and to cellular structure. Similarly, cytoskeleton of platelets also plays an important role in their structural variations, which is closely associated with specific activities or status they are currently in. For example, resting platelet is a small, discoid cell. When it is activated, accompanied by a striking reorganization of actin-based cytoskeleton, the platelet spreads to form a dendritic structure. Fine projections extend in all directions. Surfaces of these pseudopods are smooth compared with the central body from which they extend. Detailed variations in platelet architecture will be discussed in following sessions.

After activation, platelets also release a variety of fundamental growth factors that are stored in their alpha-granules, such as PDGF, VEGF, TGF-β and HGF [107, 108]. Because these growth factors are essential for the tissue-repair process, patients with traumatic injuries are often treated with platelet-rich plasma (PRP), an autologous concentration of platelets in a small volume of plasma. PRP has been extensively applied in a series of clinical treatments including bone regeneration, skin rejuvenation, bleeding reduction and other soft tissue healing [108-110]. In orthopedic and sports medicine field, PRP is widely used by professional athletes to treat

tendon and ligament injuries for a quick return to sports activities. Despite its prevalent use, efficacy of PRP treatment is still controversial due to conflicting outcomes from clinical trials, and a major contributor to these differential results is undesired variations of platelets during PRP preparation. In general, PRP is isolated simply by a low-speed centrifugation, where the stability of platelets is <2 hour since PRP contains plasma proteins, in particular enzymes, which potentially activate these platelets [111]. Therefore, it is important to analyze the states of platelets prior to use in clinical treatments to avoid inadvertent platelet activation by plasma proteins or other uncertainties.

4.1.2 Detection of Platelet Activation

Currently, most studies that evaluate platelets are based on optical microscopy observation of platelet morphologies, which is time consuming and labor intensive. Besides, some other measurement methods have been developed, including atomic force microscopy (AFM), thromboelastography (TEG), surface plasmon resonance (SPR), etc. [16, 112-115]. AFM is an invasive technique that applies an external force on individual cells. As the normal radius of AFM probe is usually <100 *nm*, it is difficult to statistically examine cell groups, although local measurement can be conducted on some specific parts of cells. TEG on the other hand is specifically used to measure platelet contribution during coagulation process. However, both AFM and TEG cannot be performed *in situ*. In comparison, SPR as a non-invasive technique is applied to monitor certain platelet activities, but it cannot analyze mechanical properties of platelets such as elasticity or viscosity [116]. The quartz TSM resonator is proposed for a real-time analysis of platelets due to its high sensitivity, repeatability, and easy connection with electronic measurement systems [33, 74]. Compared with other methods, the TSM resonator

allows a simple, non-invasive and quantitative method to extract the complex shear modulus of platelet groups.

Previous studies have presented some applications of TSM resonators in detecting platelet adhesion, activation and aggregation [117-123]. However, when characterizing platelets in PRP, platelets should not be activated on the surface of TSM resonators to avoid the formation of fibrin gel [117-119]. Recent studies reported platelet activation and adhesion where suspended platelets were activated by agonists binding to the electrode surface of TSM resonators [120-122]. In this case, the resonator response was recorded as a combination response of platelet activation and adhesion, posing a challenge to separate platelet activation signals from adhesion signals thus confounding interpretation of the results. Kunze *et al.* compared the electrical response of TSM resonators to activation of adherent platelets with and without plasma proteins, but still lacking specific explanations to activation process [123]. In addition, discussions from a perspective of mechanical properties are quite limited in these studies, and viscoelastic properties of platelets during activation process have not been precisely determined thus far. Changes in viscoelasticity and average thickness of platelets should be investigated as essential parameters, and results from such studies could contribute to the real-time detection and evaluation of platelet functions.

4.2 MATERIAL PREPARATION AND EXPERIMENTAL DETAILS

4.2.1 Isolation and Washing of Platelets

An isolation method by centrifugation and washing was adopted to obtain high-concentration platelet suspension in Tyrode's buffer without damaging and free from plasma proteins [111]. Rat blood (freshly collected from 7 ~ 9 week old rats) added with acid-citrate-dextrose (ACD, 1:6) was centrifuged at 2,300 g for 1 *min* to obtain PRP in supernatant. PRP was centrifuged again at 2,200g for 5 *min* and the pellet containing platelets was collected by discarding the supernatant platelet-poor plasma (PPP). The platelets were washed twice in Tyrode's albumin buffer following the standard washing procedure, and then suspended in Tyrode's albumin buffer containing 0.02 *U/ml* apyrase to a final concentration of ~1,000,000 */μl*.

4.2.2 Measurement and Characterization of Platelets

As shown in Fig. 10, the same measurement system of 10-*MHz* TSM resonator in previous TSC study was applied. The diameter of central circle electrodes was 5.10 *mm*. One tube (6.2 *mm*/8.0 *mm* × 6 *mm*) made of poly(dimethylsiloxane) (PDMS, Dow Corning, Midland, MI, USA) was located around the upper electrode, forming a well-like structure for platelet adhesion and activation. TSM resonators were placed in culture dishes, covered with lids, and then put into an incubator. The electrical admittance spectrums of TSM resonators were obtained using an Agilent 4294A Precision Impedance Analyzer (Agilent Technologies, Palo Alto, CA, USA). In sweep signaling, frequency step was set as 20 *Hz*, and driving voltage was 500 *mV*. For different TSM resonators in varied conditions, the sweep frequency range was adjusted within 9.96 ~

10.00 *MHz*. Prior to the measurements, TSM resonators were sterilized overnight by exposure to UV light. After that, 100 μl of 100 $\mu g/ml$ human fibrinogen (Cat. #F3879, Sigma-Aldrich, St. Louis, MO, USA) in phosphate-buffered saline (PBS, Mediatech Inc., Manassas, VA, USA) was added into wells and kept at 37ºC with 5% CO_2 for 2 *hr*. Through this procedure, the entire electrode surface of TSM resonators was coated with fibrinogen, allowing resting platelets to adhere to the substrate and then form a dense monolayer [106, 124]. Washing three times in PBS, these wells were refilled with 100 μl of a ~1,000,000 $/\mu l$ platelet suspension, and incubated at 37°C with 5% CO_2 for 2 *hr*. During this period of time, suspended platelets were adhering to the fibrinogen-coated electrode surface gradually, and corresponding electrical admittance spectrums of TSM resonators were recorded every 1 *min*. Subsequently, these wells were washed three times in PBS to remove excess, non-adherent platelets, followed by the addition of 100 μl Tyrode's albumin buffer containing 0.02 *U/ml* apyrase. Adherent platelets were then activated by different concentrations of thrombin (1 *U/ml*, 10 *U/ml* and 100 *U/ml*, Sigma-Aldrich, St. Louis, MO, USA) and maintained in an incubator at 37°C with 5% CO_2 for 2.5 *hr*, and corresponding admittance spectrums during this process were recorded every 1 *min*. In addition, the initial admittance spectrums of unloaded TSM resonators as well as that with Tyrode's albumin buffer and fibrinogen coating were also recorded for the following extraction of platelet monolayer viscoelastic properties. All measurements were performed three times, and the platelets in three independent measurements for one thrombin concentration were from the same platelet isolation step. In parallel experiments, 100 μl of a ~1,000,000 $/\mu l$ platelet suspension was added into fibrinogen-coated 96-well culture plate, and following the same procedure, adherent platelets were activated by 100 *U/ml* thrombin. Both un-activated and activated platelets were observed through optical microscopy (Eclipse TS100, Nikon, Japan).

To examine variations in platelet morphologies during activation process, platelet suspension as above was also added into fibrinogen-coated PDMS wells on Au/Si wafer and maintained in an incubator for 30 *min*. After washing in PBS to remove excess platelets and refilling 100 μl Tyrode's albumin buffer containing 0.02 *U/ml* apyrase, adherent platelets of low density were located in the incubator for further 1.5 *hr*. These platelets were then activated by thrombin of 100 *U/ml*, fixed with 4% paraformaldehyde in PBS at a series of time points after the addition of thrombin, and sequentially washed with increasing concentrations of ethanol solution (10%, 20%, 30%, 40%, 50%, 60%, 70%, 80%, 90% and 100%). The platelet morphologies were examined by scanning electron microscopy (Helios NanoLab 600 SEM, FEI, Hillsboro, OR, USA, accelerating voltage: 5 *kV*).

4.3 THEORETICAL MODEL AND ANALYTICAL METHODS

As introduced in Chapter 2, prior to the extraction of platelet monolayer's viscoelastic properties, effective parameters (η_q, h_q, C_0 and C_p) for TSM resonators with fibrinogen coating are obtained firstly. Table 6 lists the typical extracted effective parameters (h_q, μ_q, C_0 and C_p) for unloaded TSM resonator and TSM resonator with fibrinogen coating. Both fitting are well-acceptable with the error of 0.0268% and 0.0315%, leading to the affirmative calibrated parameters of TSM resonator. From Table 6, it can be seen that effective quartz crystal thickness is slightly larger than theoretical value 165 μm, and quartz viscosity is also increased compared with reference value 0.00035 *Pa·s* [31]. In the meantime, it is indicated that fibrinogen absorption does not cause distinct changes in calibrated effective parameters, when only external capacitance C_p increases to some extent. Simplified two-layer-loading model for platelet adhesion and activation

is confirmed further from this perspective, and all these parameters given in Table 6 will be used in following fitting calculation.

Then, the complex impedance of buffer medium is also calculated as

$$Z_{Buffer} = (1+j)A\sqrt{(0.6560 + 0.2249\,j)\omega}$$

With (1) the modified effective parameters for TSM resonator with fibrinogen coating, (2) the complex impedance of buffer medium, and (3) the admittance spectrum $Y(\omega_i) = G(\omega_i) + jB(\omega_i)$ for TSM resonator with platelet adhesion, the specific solution of complex shear modulus $G_{PL} = G' + jG''$ and average thickness h_{PL} of platelet monolayer can be determined.

Table 6. Calibrated parameters of TSM resonator

Effective Parameters	Unloaded TSM Resonator	TSM Resonator with Fibrinogen
Thickness of TSM h_q	166.11 μm	166.11 μm
Viscosity of Quartz μ_q	0.0406 $Pa{\cdot}s$	0.0384 $Pa{\cdot}s$
Static Capacity of TSM C_0	4.3214 pF	4.3468 pF
External Capacity of TSM C_p	6.0709 pF	6.1449 pF

4.4 RESULTS AND DISCSSIONS

4.4.1 Platelet Adhesion and Activation

Fig. 16(a) presents the typical electrical admittance spectrums of TSM resonator sensor acquired during a 2-*hr* platelet adhesion process. With an increase in incubation time, the color of admittance spectrums shifts from pink to black gradually. As more and more platelets settle on

electrodes, the intensity of resonance peaks decreases gradually, and the full width at half maximum (FWHM) becomes larger. The inset on left is corresponding resonance frequency variation curve collected from these resonance peaks, and the one on right is the mean resonance frequency shift curve for all three measurements. The extracted resonance frequencies decrease continuously in the first 1 *hr*, and then plateau as most platelets settle down. For all three independent measurements, the resonance frequency shift during platelet adhesion process presents similar tendencies. Although falling speed of platelets in suspensions varies, the overall frequency shift for TSM resonators keeps relatively stable 2 *hr* after seeding, and the mean frequency shift is – 3991 ± 210 *Hz*. Fig. 16(b) is the admittance spectrum of TSM resonator after washing the well in PBS 2 *hr* after seeding and adding the same amount of fresh Tyrode's albumin buffer. Evidently, there is an increase in both resonance peak position and intensity compared with the spectrums in black in Fig. 16(a), illustrating that not all platelets in suspension are adhered to fibrinogen-coated electrode surface. As they are not bonded to fibrinogen, those platelets on the bottom of wells are removed during washing procedure. Compared to TSM resonator with platelet suspension (spectrum in pink in Fig. 16(b)), the resonance frequency shift with adherent platelets is – 1214 *Hz*. For all three independent measurements, the increase in resonance frequency after washing is a characteristic, reproducible observation, and the mean frequency shift is – 1206 ± 195 *Hz*. These results agree well with previous research that also used TSM resonator to monitor platelet adhesion process [118]. In parallel experiments, identical dose of platelet suspensions are added into fibrinogen-coated 96-well culture plate and incubated for 2 *hr*. Then these wells are washed three times in PBS, and phase-contrast microscopy photo of adherent platelets is taken as the inset of Fig. 16(b) shows. The adherent platelets are uniformly sphere shaped with average diameter of <2 μm. They form a

dense monolayer without any obvious overlap on the substrate, or any blank space which could allow more platelets to adhere to without affecting neighboring platelets, which leads to a reasonable assumption in following calculation.

Fig. 17 shows the electrical admittance spectrum response of TSM resonator sensors during platelet activation process by thrombin (100 *U/ml*) for 2.5 *hr* (TSM resonators used in Fig. 17 are not the same ones used in adhesion experiments, and TSM resonators used in Fig. 16 are applied to monitor platelet activation by 10 *U/ml* of thrombin). Fig. 17(a) depicts the typical admittance spectrums acquired in this process when line color gradually changes from pink to black. During the first 30 *min*, the intensity of resonance peaks decreases along with a concomitant decrease in FWHM. As platelet activation progresses, the intensity of resonance peaks begins to increase and FWHM rises as well. The inset of Fig. 17(a) is corresponding resonance frequency variation curve extracted from this set of resonance peaks. All three resonance frequency variation curves from three independent measurements are presented in Fig. 17(b). The results indicate similar tendencies in resonance frequency variations during platelet activation. Three stages are evident in the entire process: I rapid increase, II decrease after a peak point, and III monotonic increase again. The initial peaks (I & II) are completed within 20 ~ 40 *min* for all three measurements. Following these peaks, a monotonic increase of frequency vs. time curves (III) shows an approximate slope of 20 *Hz/min* for all three sets of admittance spectrums. Although variation magnitude and turning points are varied because of slight changes in platelet concentration and other related factors, these results exhibit consistent variation tendencies with previous research where TSM resonator is also applied to monitor platelet activation process [123]. In parallel experiments, adherent platelets in 96-well culture plate are activated by thrombin of 100 *U/ml*, and phase-contrast microscopy photo is taken after 2.5 *hr* as

the inset of Fig. 17(b) shows. Compared with adherent platelets, activated platelets possess highly fragmented morphologies. There is no regular, consistent disc shape for activated platelets, and a number of small pieces are observed over the entire substrate. Significant changes are demonstrated in platelet architecture and corresponding electrical response of TSM resonators during activation process.

4.4.2 Viscoelasticity and Cytoskeleton of Platelets

To further understand related changes on platelets, their morphologies and viscoelastic properties in the entire activation process are investigated. Fig. 18(a) presents the SEM photos of adherent platelets taken at a series of time points after thrombin (100 *U/ml*) is added into the PDMS wells on Au/Si wafer. From left to right, these photos are taken after 0, 10 *min*, 20 *min*, 30 *min*, 1 *hr* and 2 *hr* in order, respectively. Photos in the first row are a partially enlarged view of corresponding ones in the second row, presenting the characteristic morphologies of platelets at different time points. During the entire activation process, although the overall shapes are varied between each other, adherent platelets still exhibit relatively consistent, characteristic structure at each time point, indicating platelet monolayer an isotropic, homogeneous layer. It should be noted that with an increase in incubation time there are significant changes in platelet architecture. The first recognizable change is a transformation from a discoid to a more spherical shape during the first 10 *min*. Subsequently, some fingerlike projections, filopods (also called cellular antennae) are elaborated from the spheres surface as shown in 10-*min* and 20-*min* photos. Following filopodial growth, platelets begin to spread onto the substrate at around 20 *min*. By 30 *min*, large circumferential lamellas form and platelets exhibit a “fried-egg” shape. Such spreading drastically increases the surface area of platelets. With continued incubation,

some new filopods are also observed on the central dense aggregation part in 30-*min* photos. Growth of these filopods results in a shrunk, fragmented central part structure as shown in 60-*min* photos. Because of continuous platelet spreading and filopod extending, after 2 *hr*, the platelets become quite thin, flat and fragmented, and the "fried-egg" structure almost disappears.

Variations in platelet architecture from a discoid to an activated form primarily depend on the remolding of their internal actin cytoskeleton [104, 125]. For a typical cell, cytoskeleton as an intricate 3-dimensional (3D) array of microfilaments, microtubules and intermediate filaments, helps establish and maintain cell shape. The lipid plasma membrane surrounding defines the cell's boundary accordingly [5]. In resting platelets, long actin filaments are distributed within the platelet cytoplasm to form a sparse fibrous network, supporting the initial disc structure together with a microtubule coil that runs along the perimeter of the disc. When platelets are activated by thrombin, these long actin filaments are fragmentized into a number of short actin filaments, and the microtubules forming the coil are disassembled as well, leading to a rounding up of platelets as the first recognizable change. Subsequently, accompanied by platelet spreading and filopod extending, a striking reorganization of actin cytoskeleton occurs in platelets. It is indicated that regions that correspond to circumferential lamellae are densely filled with a 3D network of short actin filaments, and these elaborated filopods are also filled with long filaments with roots that are coalesced from filaments in the cytoskeletal center [104]. Therefore, with continuous spreading, the rounding platelets cannot only reorganize those short actin filaments that originated from the long ones, but also assemble new net filaments. The process of platelet cytoskeleton reorganization is carried out with the growth of abundant new actin filaments. For fully activated platelets, except the drastically compressed central part, the entire platelets are occupied by a fully established dense network of actin filaments.

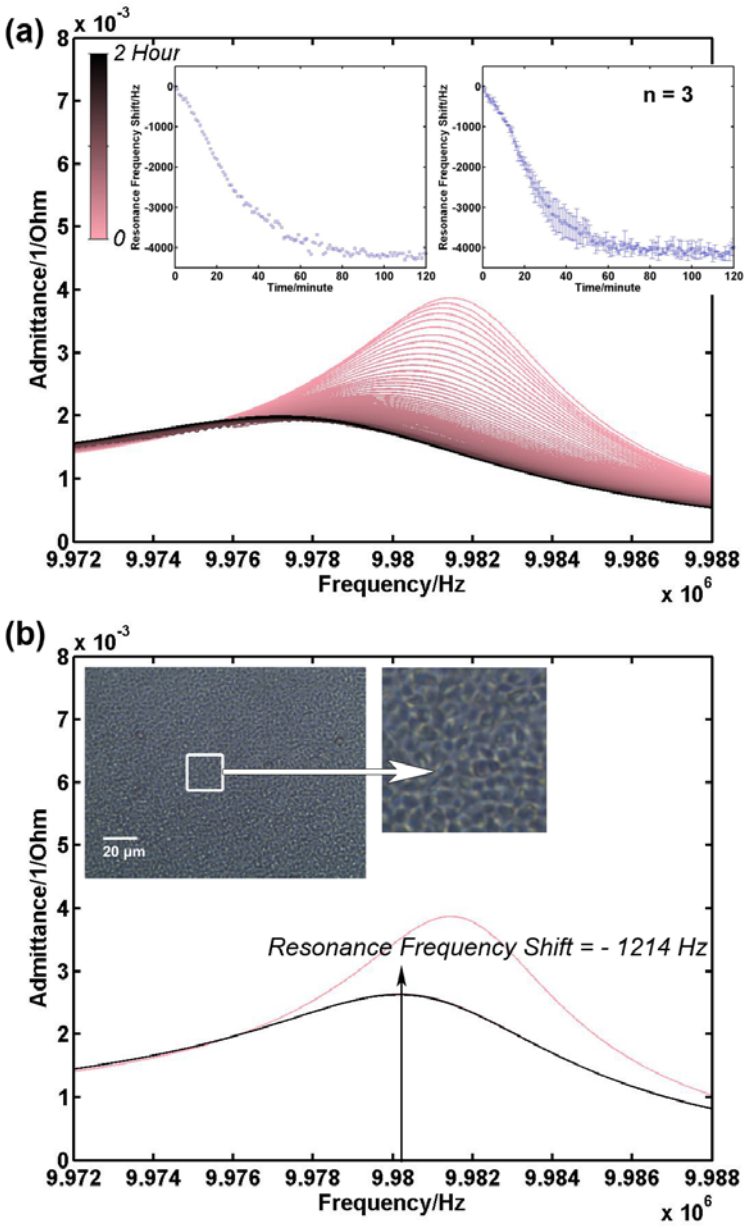

Figure 16. Platelet adhesion: (a) Admittance spectrum set of TSM resonator during platelet adhesion process (adding platelet suspension at Time = 0). The insets on left is corresponding resonance frequency shift curve, and the one on right is the mean resonance frequency shift curve for all three measurements. (b) Admittance spectrum of TSM resonator with platelet suspension (pink) and with adherent platelet monolayer (black). The inset is phase-contrast photo of adherent platelets in 96-well plate taken after 2 *hr* of platelet adhesion process.

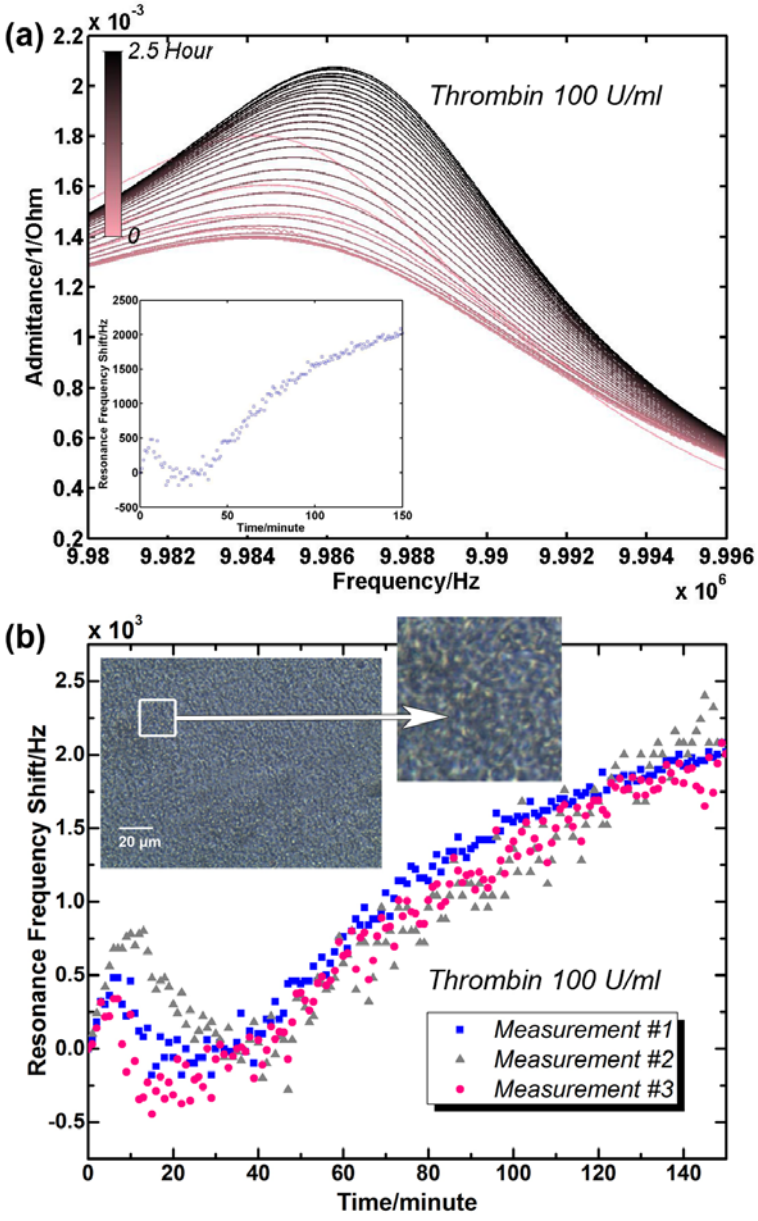

Figure 17. Platelet activation by thrombin (100 *U/ml*): (a) Admittance spectrum set of TSM resonator during platelet activation (adding thrombin directly after Time = 0) and corresponding resonance frequency shift curve. For clarity, admittance spectrums were plotted every 5 *min*. (b) Resonance frequency shift curves of TSM resonators during platelet activation and phase-contrast photo of activated platelets. The inset is phase-contrast photo of activated platelets in 96-well plate taken after 2.5 *hr* of platelet activation process.

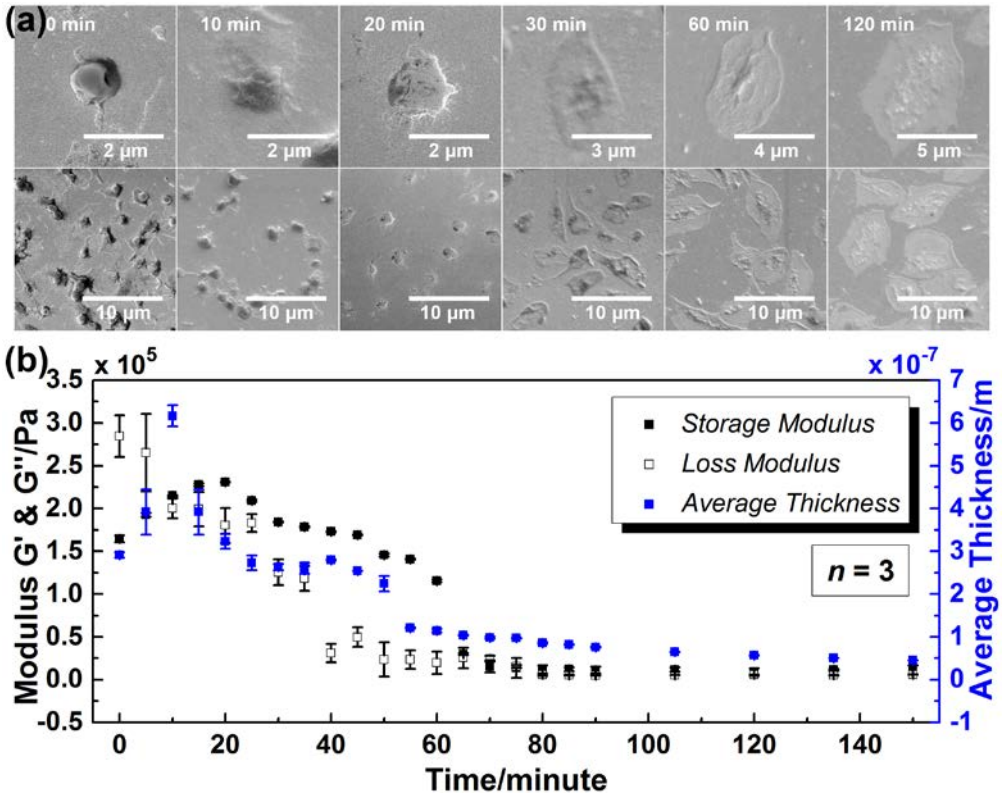

Figure 18. Characterization of platelet monolayer at a series of time points during platelet activation by thrombin (100 *U/ml*) (adding thrombin directly after Time = 0): (a) SEM photos of platelets (Photos in the first row are a partially enlarged view of corresponding ones in the second row, presenting the characteristic morphologies of platelets at different time points.) (b) Storage modulus G', loss modulus G'' and average thickness h_{PL}

In the meantime, based on the two-layer-loading transmission line model (TLM), a programmed analyzer is built up for extraction of platelet monolayer viscoelastic properties. Assuming isotropic, homogeneous platelet monolayer, its equivalent density is preset in the algorithm. In our previous work, a set of approximate values for the density of cell monolayer have been examined, and the theoretical model exhibited high consistency with experimental results in the case of 1.00 g/cm^3 [126]. Thus, 1.00 g/cm^3 is adopted as the equivalent density of platelet monolayer. Sending the electrical admittance spectrums acquired at a series of time

points to the analyzer, the complex shear modulus of platelet monolayer G', G'' as well as average thickness h_{PL} are obtained. The error upper limit is set as 1%. Much smaller than this setting point, the fitting errors in extraction procedure are all stabilized <0.1%, indicating certainty and reliability of extracted parameters. Fig. 18(b) gives G', G'' and h_{PL} at different time points during platelet activation. Significant variations of G', G'' and h_{PL} are observed in the initial stage of activation process. However, as activation continues beyond 1 *hr*, both G' and G'' present similar stable tendencies. For storage modulus G', there is an obvious increase in the beginning, followed by a decrease with continued incubation. The maximum value of G' is 230,662 ± 452 *Pa*, achieved at 20 *min*. After 1 *hr*, G' tends to be stable, and the final value is around 11000 *Pa*. Loss modulus G'' decreases gradually from 284,520 ± 24,511 *Pa* to 19,864 ± 13,084 *Pa* during the first 1 *hr*, and then enters a plateau phase as well. Besides, the average thickness h_{PL} increases sharply in the first 10 *min* with the peak value of 616 ± 25 *nm* acquired at 10 *min*, and then begins to decrease with continued incubation. After 1 *hr*, h_{PL} already decreases to ~100 *nm*. The rate of decrease reduces gradually, and the final value of h_{PL} acquired after 2.5 *hr* is <50 *nm*. During this period after 1-*hr* incubation, continuous increase in resonance frequency shift as shown in Fig. 17 is attributed to slight changes in G', G'' and h_{PL}, especially h_{PL}. Taking the average shear modulus obtained after 1 *hr* G' = 10000 *Pa* and G'' = 5000 *Pa* as an example, the relation between the resonance frequency shift and coating thickness keeps a good linearity as coating thickness goes into 0.04 ~ 0.09 μm (this range is where average thickness of platelets obtained after 1 *hr*). The change rate of the resonance frequency shift is about –16 *Hz*/*nm*. Thus, although Fig. 18(b) presents relatively stable tendencies for G', G'' and h_{PL} after 1 *hr*, the resonance frequency shift still changes continuously.

The changes in both viscoelasticity and average thickness of platelet monolayer could be associated with variations in platelet architecture based on remolding of their internal actin cytoskeleton. Fig. 18 illustrates that h_{PL} could accurately describe the average thickness of platelet monolayer. When platelets transform from a discoid to a more spherical structure, their effective height increases as indicated in h_{PL}'s increase during the first 10 *min*. Peak value of h_{PL} is acquired when platelets show their typical spherical shape. As platelets begin spreading, their height decreases significantly, which is demonstrated by h_{PL}'s continuous decrease after 10 *min*. G' and G'' values also correlate well with the corresponding variations in platelet architecture. The peak position of G' is at 20 *min* following the peak position of h_{PL}, when some filopods are elaborated from the periphery of platelets but without obvious cell spreading. Although the shear stiffness of original long-fibrous network is reduced partially with filament fragmentation and cell rounding, the growth of filopods, which are filled with bundled long actin filaments, could increase the cytoskeletal stiffness to some extent. However, as platelets begin spreading, a dense 3D network of short actin filaments is established gradually. Compared to the long-fibrous network of resting platelets, the short-flocculent structure occupying the interior space of activated platelets could reduce the overall shear stiffness due to good deformation capacity of short-actin-filament connections. Thus, as more and more net filaments assemble and large lamellas overlap, G' of platelet monolayer decreases until 1 *hr*. In the meantime, both filopod extending and platelet spreading through short-actin-filament assembly could compress the cytoplasm regions extensively, thereby decreasing the effect of cytoplasm viscosity on G''. In this case, G'' of platelet monolayer decreases continuously during the entire activation process. After 1 *hr* of activation, when the interior of almost all the platelets is occupied by a dense network of short actin filaments, and there are no further considerable changes in platelet

cytoskeleton, both G' and G'' tend to be stable, and only a slight decrease can be observed in h_{PL}. The viscoelasticity and average thickness of platelet monolayer exhibit quite different tendencies with the resonance frequency shift of TSM resonators. Thus, G', G'' and h_{PL} could provide quantitative, conclusive details on platelet structure variations in activation process.

4.4.3 Monitoring Activation Process of Platelets in Different Concentrations

Fig. 19 shows the typical resonance frequency variation curves of TSM resonators during platelet activation by different concentrations of thrombin. Similar to that of thrombin of 100 *U/ml* in Fig. 17(b), three independent measurement results of both 10 *U/ml* and 1 *U/ml* present consistent tendencies in resonance frequency variations during platelet activation. For clarity, typical resonance frequency shift curve is applied to represent characteristic variations of all three measurements. It is indicated that the resonance frequencies extracted from electrical admittance spectrum sets exhibit similar variation tendencies: I initial increase, II decrease after a peak point, and III monotonic increase again. The main differences between Fig. 17 and Fig. 19 are merely expressed in the time distributed to three stages, as well as the magnitude of frequency change. Compared with 100 *U/ml*, the peak positions for 1 *U/ml* and 10 *U/ml* are postponed to 10 ~ 20 *min*. Accordingly, the elapsed time before monotonic increase (Stage III) is also extended as the concentration of thrombin decreases. The second increase for 1 *U/ml* and 10 *U/ml* starts at around 70 *min* and 50 *min*, respectively, when that of 100 *U/ml* starts after only 20 *min* of activation. This phenomenon could be attributed to the mechanism of platelet activation. When high concentration of thrombin (100 *U/ml*) is added into PDMS wells, a large part of adherent platelets are activated simultaneously and the performance of platelets exhibit group consistency as shown in those SEM photos in Fig. 18. Thus, corresponding electrical response of TSM

resonators show explicit changes which relates well with specific cellular architecture variations of platelet group. Nevertheless, in response to low concentrations of thrombin (1 *U/ml*, 10 *U/ml*), a small part of adherent platelets are activated at first, when others keep resting until new potent agonists are secreted by activated platelets [104, 105]. In this case, there is no obvious group consistency for platelets in the beginning of activation process, and with continuous secretion of agonists, a large number of resting platelets are activated in succession. Only when the number of platelets activated at the same time is large enough, dominant activities of platelet group could be manifested in TSM resonator's response to some extent, resulting in a flatter peak and a longer valley before the second increase. Besides, for all three thrombin concentrations the monotonic increase curves keep similar increase slopes. In Fig. 17 and Fig. 18, for 100 *U/ml*, the starting time point of monotonic increase is associated with the peak position of G', as well as the initial spreading of platelets. Because of continuous spreading of platelets, the viscoelasticity and average thickness of platelet monolayer keep decreasing, leading to a steady rise of resonance frequency shift of TSM resonators. Therefore, it can be deduced that for 1 *U/ml* and 10 *U/ml*, despite varied conditions of spreading, almost all the platelets start to spread after about 70 *min* and 50 *min*, respectively.

Fig. 20 gives the extracted G', G'' and h_{PL} at a series of time points of platelet activation by different concentrations of thrombin. The fitting errors for all three concentrations are stabilized <0.2%. Fig. 20(a) shows that with varied concentrations of thrombin, the variation tendencies of storage modulus G' are not exactly the same. For 100 *U/ml*, there is an increase at first, and then a decrease with continued incubation. However, for 1 *U/ml* and 10 *U/ml*, there is a slight decrease in the beginning, followed by an increase and a decrease again. As the concentration of thrombin decreases, peak value of G' decreases gradually, and peak position

shifts to a higher time point. G' can achieve the maximum value of 230,662 ± 452 *Pa* at 20 *min* with 100 *U/ml* thrombin, when the peak values for 1 *U/ml* and 10 *U/ml* are respectively 163,606 ± 382 *Pa* at 70 *min* and 174,973 ± 20,544 *Pa* at 60 *min*. After 1 *hr*, as G' for 100 *U/ml* tends to be stable, there is still an obvious decrease for low concentrations. In comparison, the variation tendencies of loss modulus G'' for different concentrations are quite similar as shown in Fig. 20(b). G'' goes down continuously and then enters a plateau. Primary differences are focused on an extended duration of reduction as the concentration of thrombin decreases. With 100 *U/ml* thrombin, G'' becomes <40,000 *Pa* after only 40 *min*, when that turns to 80 *min* and 60 *min* for 1 *U/ml* and 10 *U/ml*, respectively. In addition, as it is shown in Fig. 20(c), variations of average thickness h_{PL} for three concentrations are also analogous to each other. h_{PL} increases in the beginning, and then decreases gradually with continued incubation. For low concentrations, there is a relatively stable stage before h_{PL} arrives at its peak point. The sharp peak observed in h_{PL} of 100 *U/ml* disappears in the case of low concentrations, replaced by a flat, backward-shifting peak. For 100 *U/ml*, the peak value of h_{PL} acquired at 10 *min* is 616.14 ± 24.78 *nm*. For 1 *U/ml* and 10 *U/ml*, the peak values are achieved as 280.00 ± 33.37 *nm* at 60 *min* and 431.17 ± 40.91 *nm* at 40 *min*, respectively. The final value of h_{PL} rises as the concentration of thrombin decreases. Even though, for all three concentrations, h_{PL} are <100 *nm* after 2.5 *hr*.

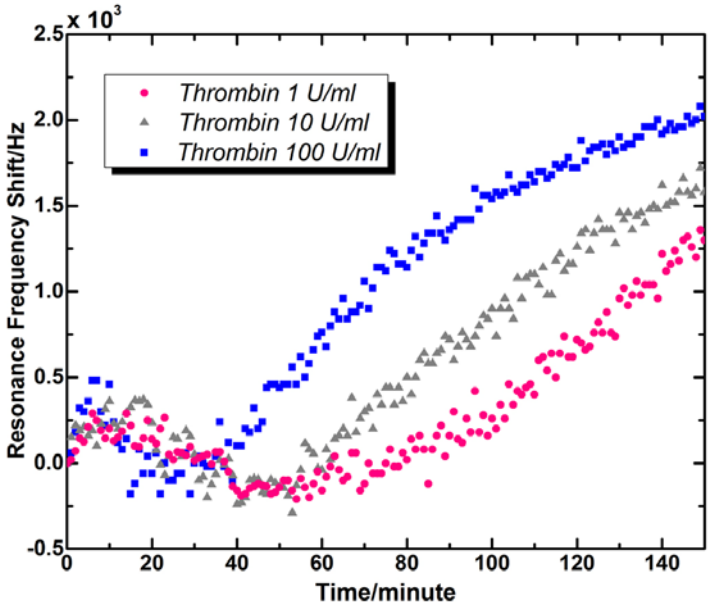

Figure 19. Typical resonance frequency shift curves of TSM resonators during platelet activation by different concentrations of thrombin (adding thrombin directly after Time = 0)

Variations in G', G'' and h_{PL} depending on thrombin concentrations could be associated with the activation mechanism discussed in previous session. In spite of some differences in detail, with a decrease of thrombin concentration from 100 *U/ml* to 1 *U/ml*, all variation peaks and plateaus in G', G'' and h_{PL} are shifted to a higher time point. Changes of low concentrations (1 *U/ml*, 10 *U/ml*) are not as sharp as that of 100 *U/ml*, especially the flat peak shapes and low peak values. With addition of thrombin in low concentrations, the activation processes of all adherent platelets are not simultaneous, and part of resting platelets need be activated by agonists secreted by activated platelets. When enough platelets have been activated, variations in G', G'' and h_{PL} start to show evident tendencies, revealing the dominant activities of platelets on TSM resonators. Peak value of h_{PL} is acquired when platelets show their typical spherical shape as the first transformation in activation process. For 1 *U/ml* and 10 *U/ml*, the peak values are obtained

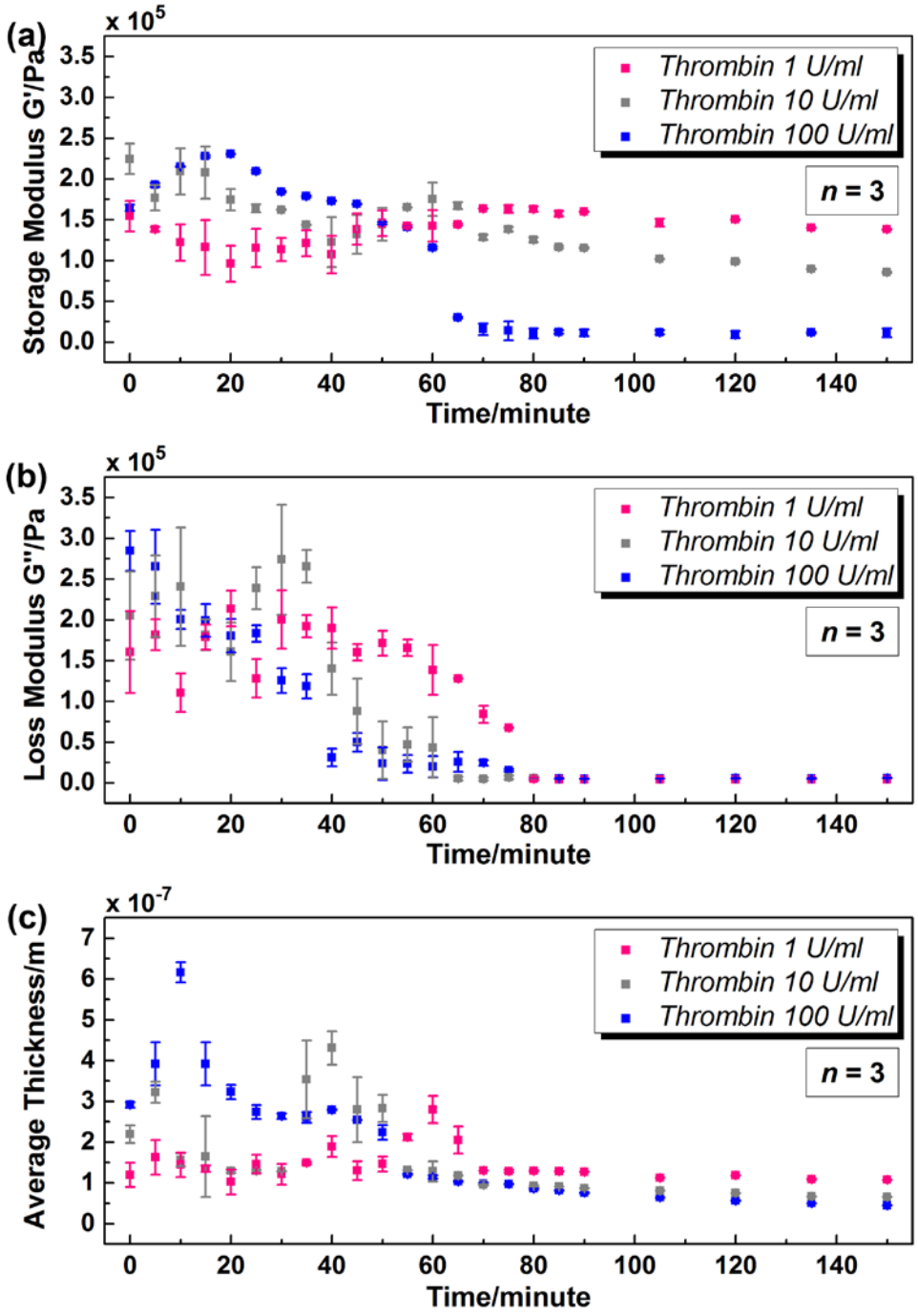

Figure 20. Characterization of platelet monolayer at a series of time points during platelet activation by different concentrations of thrombin (adding thrombin directly after Time = 0): (a) Storage modulus G' (b) Loss modulus G'' (c) Average thickness h_{PL}

at 60 *min* and 40 *min* respectively, indicating the starting time point of shape transformation for a dominant part of platelets. The peak of G' appears 10 ~ 20 *min* after the peak of h_{PL}, when some filopods are elaborated from the periphery of platelets but without obvious cell spreading. For 1 *U/ml* and 10 *U/ml*, the spreading of a large part of platelets starts at around 70 *min* and 60 *min* respectively, reaching good agreement with previous observations from Fig. 19. In fact, for all three concentrations, the overall viscoelasticity and average thickness keep decreasing with platelet spreading, leading to a steady rise of TSM resonance frequency shift. Thus, specific stages during activation process can be deducted from variations of G', G'' and h_{PL}. With comparable values of G', G'' and h_{PL}, it is indicated that the condition of platelets at 2.5 *hr* with thrombin of 1 *U/ml* are analogous to that at 60 *min* with 100 U/ml as shown in Fig. 18.

4.4.4 Comparison of TSM Resonator with Other Measurement Methods

In a series of transmission electron microscopy (TEM) photos, the cross section of resting platelets is a Frisbee-like shape, and periphery thickness is smaller than the central thickness (central thickness is approximately 0.5 μm). Once activated, the thickness of elaborated filopods and lamellipods are observed to be quite thin (<100 *nm*). In Fig. 18(b), the average thickness h_{PL} of resting platelets is 291 ± 6 *nm*, and after 1 *hr* of thrombin incubation is ~100 *nm*, indicating the same order as that observed by TEM [104]. Besides, the viscoelasticity of activated platelets is in good agreement with that obtained by AFM, even though local measurement on individual platelets was conducted in AFM. According to viscoelasticity theory, complex shear modulus $G_{PL} = G' + jG''$ depends on oscillation frequency ω. Their relation in power-law structural damping model is shown functionally in (89) and (90). When the modulus scale factor G_0 = constant, $G' \infty f^{\gamma}$. For different concentrations of thrombin, storage modulus G' of activated

platelets is 10 ~ 130 *kPa* after 2.5 *hr*. When γ is assigned with 0.12, G' of activated platelets at 20 *Hz* is calculated as 2 ~ 27 *kPa*. When γ = 0.14, G' turns out to be 1 ~ 21 *kPa*. The converted storage modulus G' at low frequency is of the same order magnitude with AFM results (1 ~ 50 *kPa*, ~20 *Hz*) [112]. From this perspective, G' as statistical stiffness of platelet monolayer could reflect characteristic shear elasticity of individual platelet in a group. In the meantime, due to the stable, average, statistical features of TSM resonators, variations of platelet viscoelasticity during activation process could be amplified appropriately compared with other local-measurement techniques, implying a potential of TSM resonator for mechanical-property mark. Through high-frequency TSM resonators, reliable and repeatable shear modules of platelet monolayer with varied cytoskeleton are provided in an economic, simple, non-invasive manner. Furthermore, the average thickness of platelet monolayer is obtained as well. According to variations in shear modulus and average thickness of cell monolayer, internal cellular architecture could be deduced and corresponding status in a variety of procedures (activation, aggregation, etc.) be acquired.

4.5 CONCLUSIONS

In this chapter, quartz TSM resonator sensor is adopted to monitor the process of platelet activation. Resting platelets adhering to fibrinogen-coated electrodes are activated by different concentrations of thrombin (1 *U/ml*, 10 *U/ml* and 100 *U/ml*), and corresponding complex shear modulus ($G' + jG''$) and average thickness (h_{PL}) of platelet monolayer at a series of time points are obtained. The extracted G', G'' and h_{PL} exhibit similar tendencies for varied concentrations of thrombin. Decrease of thrombin concentration brings an overall shift of peaks and plateaus to higher time points in G', G'' and h_{PL}, which could be associated with the partial activation of

platelets by low concentrations of thrombin. Meanwhile, changes of low concentrations (1 *U/ml*, 10 *U/ml*) are not as sharp as that of 100 *U/ml*, especially the flat peak shapes and low peak values. Variations in G', G'' and h_{PL} during activation process could be attributed to the remolding of actin cytoskeleton in platelets, which also induces evident changes in cell morphologies. The peak value of h_{PL} is acquired when platelets present their typical spherical shape as the first transformation in activation process. The G' peak appears 10 ~ 20 *min* after h_{PL} peak, when some filopods are observed along the periphery of platelets but without obvious cell spreading. As platelet spreading begins and continues, G', G'' and h_{PL} decreases, leading to a steady rise of resonance frequency shift of TSM resonators. These evaluations identify an economic, quantitative, non-invasive method to real-time measure relevant properties of platelets, which could also contribute to current PRP treatment. Furthermore, viscoelasticity and thickness changes reflect internal cytoskeleton variations that are involved extensively in a variety of cell activities, such as contractility and differentiation. G', G'' and h_{PL} can provide useful quantitative measures on platelet structure variations in activation, indicating potential of TSM resonators in characterization of cells during some specific transformation processes. TSM resonators exhibit high reliability and stability in monitoring of platelet activation, revealing an advisable technique to investigate cell activities in general, and platelet activation in particular.

5.0 A CELL-BASED LOVE-MODE ACOUSTIC WAVE BIOSENSOR WITH A BIOCOMPATIBLE WAVE GUIDING LAYER

In this chapter, a 36º *YX*-$LiTaO_3$ based Love wave sensor with a parylene-C wave guiding layer is considered as a cell-based biosensor. Starting from basic piezoelectric constitutive relations and acoustic wave propagation equations, a theoretical model of a Love wave biosensor is developed. Assuming the cells attached to the surface of the device as a uniform viscoelastic layer, the Love wave propagation in the wave guiding layer, adherent cell layer and penetration into the liquid medium are described. The effects of viscoelastic guiding layer and liquid medium on coupling coefficient K^2, propagation loss *PL* as well as sensor response to mass loading (mass sensitivity) are analyzed, from which the optimization criteria of wave guiding layer thickness in a Love wave biosensor can be deduced. In addition, this Love wave sensor is applied to monitor the adhesion process of cells. The effects of viscoelastic cell layer and wave guiding layer on the propagation velocity v and propagation loss *PL* are analyzed based on the theoretical model. The numerical results indicate that the adherent cell layer of various storage or loss shear modulus in certain range can cause evident, characteristic variations in propagation velocity and propagation loss, revealing the potential of Love wave sensors in providing useful quantitative measures on cellular mechanical properties.

5.1 INTRODUCTION

5.1.1 Material Selection of Love Wave Biosensors

As discussed in Session 2.4.1, the common piezoelectric substrates for Love wave sensors are quartz (ST-cut), 36º *YX*-$LiTaO_3$ and 36º *YX*-$LiNbO_3$ [41]. Among them, the low insertion loss and large electromechanical coupling coefficient provide 36º *YX*-$LiTaO_3$ advantages over other substrates [47]. Particularly, $LiTaO_3$ is considered as a better substrate material for relatively high loss applications, for example, with a viscoelastic biocompatible polymer wave guiding layer [48]. The main shortcoming of 36º *YX*-$LiTaO_3$ substrate is that it does not generate a pure shear wave, which may lead to increased damping in a liquid medium [61]. Thus for designing a highly sensitive $LiTaO_3$-based Love wave biosensor, it is crucial to minimize the acoustic propagation loss when the device is used in a liquid medium. So far, some theoretical discussions have been conducted on Love wave sensors, for the optimization of the transducers, minimizing propagation losses and reducing undesirable modes. Most of these theoretical calculations started with piezoelectric crystal substrates that generate a pure SH-SAW [41, 54, 59]. These studies mainly focused on sensors based on quartz crystal in 32 point group, rather than $LiTaO_3$ and $LiNbO_3$ crystals that belong to 3*m* point group. In addition, as the key part of a Love wave sensor, the wave guiding layer plays a crucial role in improving device performance. Various thin film materials have been considered as the guiding layer, including ZnO, SiO_2 and PMMA [43-46]. With a lack of proper biocompatible interface, most of the previous studies on Love wave sensors did not pay attention to their potential applications in cell-based bio-sensing. Some relevant experimental studies have reported the use of some biocompatible polymer wave guiding layers, such as PMMA [43, 44], polyimide [47] and novolac [48, 49]. Studies by Bender

et al, and Lange *et al* have shown that parylene-C [poly(2-chloro-p-xylylene)] was an appropriate acoustic-wave guiding layer due to its good uniformity, compactness and adhesion to the substrate [50, 127]. More importantly, the cell-based biosensor need support adherent living cells as a part of itself, creating a natural environment required by living cells [4]. Since cells are seeded and cultured on the sensing surface of metal or ceramic materials, but not directly on the standard cell culture wares such as a petri dish, slide, or other glass or polymeric plastic dishes, living cells should adhere to the surface without any limitations on their own biological functions, thus providing comparable references for their reactions in real natural environments. Parylene-C film possesses comparable cell and protein compatibility to the standard tissue culture substrate, indicating its great potentiality as a biocompatible interface for biomedical devices [51]. In general, polymer films have relatively low shear velocities, leading to an increased mass sensitivity. However, polymer films may also cause high acoustic wave propagation loss due to their viscoelastic properties, which is a disadvantage for Love wave biosensor applications.

5.1.2 Research Progress of Love Wave Biosensors

Recent experimental studies have reported the structural and functional optimization of Love wave biosensors for reducing propagation loss and improving sensitivity. Acoustic attenuation or damping effect caused by liquid medium has been analyzed in some theoretical studies based on different assumptions and theoretical models [80, 128-130]. In these studies, Love wave propagation was assumed to have a similar attenuation as the thickness shear mode (TSM) wave propagation along the thickness direction of piezoelectric crystals, which did not agree with experimental observations. Perturbation theory, as an approximation approach, was also adopted

in some of the Love wave sensor analyses; and the computational results agreed with experimental observations at the initial stage. However, an increasing deviation was found as the conditions varied continuously [131, 132]. The wave propagation losses caused by the viscoelastic wave guiding layer were also investigated in some studies. For example, *Kielczynski* proposed a low-loss theoretical model with relatively thick guiding layer, which was a first order theory valid for materials of low loss[133]. For more accurate results, higher order terms must be taken into account in the case of the Love wave propagation in high-loss medium. Starting from basic piezoelectric constitutive relations, *Liu et al* derived a model based on acoustic wave propagation equations through different layers to calculate performance parameters of Love wave sensors [55]. Love wave delay line on an ST-90° X quartz substrate was considered with an SU-8 wave guiding layer in the study, but the liquid loading effect was not taken into account. *McHale et al* derived the theoretical mass, liquid, and polymer sensitivity of Love wave and layer-guided shear horizontal acoustic plate mode (SH-APM) sensors with elastic and viscoelastic wave guiding layers [134, 135]. However, regardless of the effect of crystal substrate, there is a lack of experiment-related discussions on the optimal thickness of wave guiding layer. In addition, the mechanical properties of polymer materials at high frequencies differ from those at low frequency range, and a creep behavior is found with an increased frequency. The viscoelastic model for the wave guiding layer, i.e., the simple Maxwell model that describes the viscoelasticity as a spring connected to a dashpot in series, is over-simplified and needs further modification to reflect the real situation [55]. To better understand the Love wave sensor response to a soft viscoelastic thin film attached or adherent to the sensor surface, a more comprehensive theoretical analysis is needed that takes into account the device structure, electromechanical properties of piezoelectric crystal substrate, viscoelastic properties and

thickness of the wave guiding layer, and liquid loading, thus optimizing the performance of Love wave sensors for more effective biosensor applications.

In Love wave sensor tests, resonance frequency (or propagation velocity) and insertion loss are usually monitored in response to the properties or property variations of materials attached on the surface of the wave guiding layer, such as a layer of protein molecules or a cell monolayer. Some experimental studies have reported the cell-based applications of Love wave sensors; however, there is no mature theoretical analysis on them [136]. Most of these studies merely described the electrical sensor response to specific cellular behaviors from a perspective of experimental observation, but lacking in-depth theoretical explanation on the internal relation between signal changes and the corresponding cellular behaviors. In fact, without cellular structural or mechanical properties as intermediate parameters, this internal relation could not be established successfully. Based on the perturbation theory, considering the Love wave sensor as a simple mass sensor, an approximate linear relation was set up in some studies, in which no clear meaning was given to the linear relation coefficient. Along with a continuously varying condition, linear relation could not be maintained since the approximation prerequisite was not satisfied any more. Due to the lack of experiment-related discussions, there is little research focusing on theoretical modeling of the cell-based Love wave sensors, and an in-depth, comprehensive theoretical analysis is still lacking. Currently, the transduction process of cellular output to electrical signals that can be measured and analyzed has not been fully understood in Love wave biosensors. Therefore, more efforts need be devoted for a better understanding of the relation between variations in sensor response (e.g. resonance frequency, insertion loss) and cellular properties, thus achieving quantitative characterization of adherent cells in response to physical, chemical or biological stimulus. The performance of cell-based Love wave sensors

should be investigated based on a relatively mature theoretical model, which can contribute to sensor measurements and applications.

5.2 A LOVE WAVE BIOSENSOR WITH A WAVE GUIDING LAYER

From the theoretical model discussed in Session 2.4, a series of numerical results are obtained on a 36º *YX*-$LiTaO_3$ based Love wave biosensor as shown in Fig. 9. The period of Au/Ti IDTs is λ = 32 μm. Au/Ti thin films are deposited on the sensing area between the input and output IDTs, giving an operating frequency around 128 *MHz* for metalized surface. Since Au/Ti films are relatively thin (~150 *nm*), their effect on Love wave propagation can be neglected. Parylene-C film with the thickness *h* is deposited on the surface of Au/Ti film as the wave guiding layer. The elastic, piezoelectric and permittivity constant matrices, as well as the density of $LiTaO_3$ crystal reported by *Smith et al* are adopted for this work [60]. The material parameters of the wave guiding layer are set as follows: for pure elastic case, ρ_L = 1289 kg/m^3, $c_L = \mu_L$ = 0.985 *GPa*; and for viscoelastic case, ρ_L = 1289 kg/m^3, $\mu_0 = \mu_1$ = 0.985 *GPa*, τ = 0.01, 0.02 *ns*. In the latter case, the storage shear modulus is set at a relatively constant value around μ_L = 0.985 *GPa* with varying angular frequency ω when the loss shear modulus changes in orders of magnitude by setting different relaxation time τ. In addition, with pure water as the liquid medium in the calculation, the values of ρ_M = 1000 kg/m^3, η_M = 0.00102 *Pa·s* are used.

Generally speaking, the performance of the Love wave biosensors, such as resonance frequency shift or insertion loss, is affected by a series of factors in various degrees. Previous studies have reported the effects of piezoelectric crystal substrate [131], viscoelasticity of guiding layer [49], and liquid medium [41] on the insertion loss of the Love wave sensors. Based

on the theoretical calculations, the Love wave biosensor with a parylene-C wave guiding layer can be evaluated.

5.2.1 A Love Wave Sensor in Vacuum

Fig. 21 shows the propagation velocity υ and coupling coefficient K^2 for a Love wave sensor in a vacuum: the left is with an ideal elastic wave guiding layer, and the right is with a viscoelastic one. From the perspective of sensor applications, only the fundamental, zero-order Love waves generated in a certain range of wave guiding layer thickness are investigated. The results indicate that for both free and metalized surface, propagation velocity υ decreases with the normalized thickness of wave guiding layer: in the beginning, as h/λ increases, υ decreases slightly and its value is still larger than 4000 *m/s* at h/λ = 0.04; and as h/λ further increases, υ decreases dramatically to ~3600 *m/s* at h/λ = 0.06. The wave propagation velocities for free and metalized surface show the similar variation tendencies, although with different starting points. The coupling coefficient K^2 defined in Eq. (85) does not show monotonic change with respect to h/λ: with an initial increase in h/λ, K^2 increases gradually and achieves a peak value of 0.07138 at h/λ = 0.045; and as h/λ increases further, K^2 decreases quickly, and its value reaches to ~0.02 at h/λ = 0.06. For the input IDTs, a high coupling coefficient value means that the device can excite a strong Love wave, and for the output IDTs, it indicates a strong electrical signal can be detected by the instruments. In other words, a large electromechanical coupling coefficient will result in a low insertion loss for the delay line Love mode SAW sensor. In addition, from Fig. 21, it can be seen that there is no significant difference in υ and K^2 versus the normalized thickness h/λ between a pure elastic wave guiding layer and a viscoelastic wave guiding layer when a similar

storage shear modulus is used in the computation. Changes caused by various loss shear modulus can be considered negligible as it is shown in the right plot of Fig. 21.

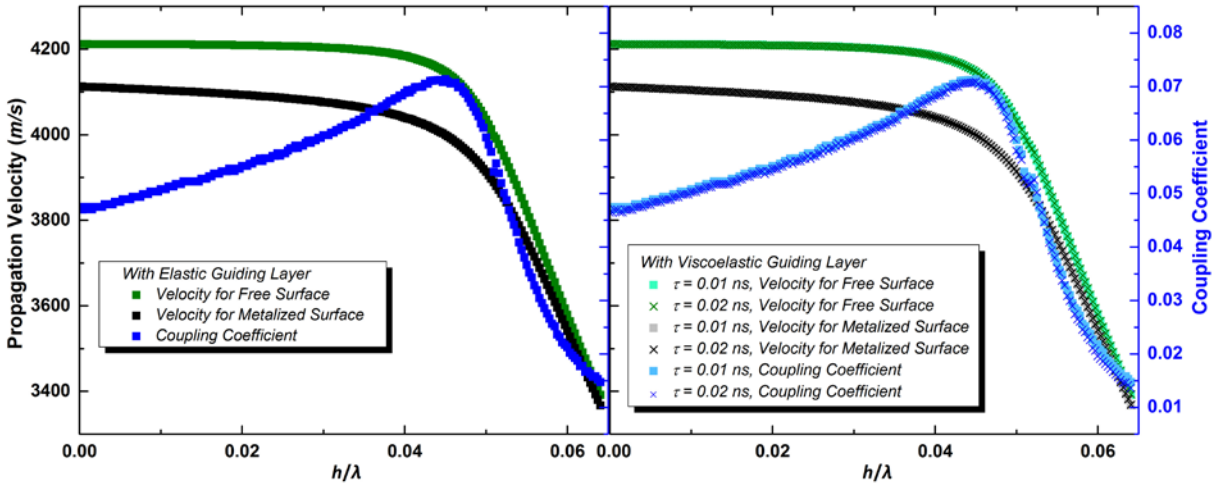

Figure 21. Propagation velocity of Love and coupling coefficient wave biosensor with a wave guiding layer

Shown in Fig. 22(a) are the propagation velocity υ and propagation loss *PL* versus the normalized thickness h/λ for a Love wave sensor in a vacuum with an ideal elastic wave guiding layer. With the normalized thickness h/λ increases, υ initially decreases gradually, and a more significant decrease can be seen when $h/\lambda > 0.04$. The propagation loss *PL* decreases to near 0×10^{-6} *dB*/*mm* at $h/\lambda=0.06$. The maximum *PL* value (0.5×10^{-6} *dB*/*mm*) is obtained when the Love wave propagation along the surface of 36º *YX*-$LiTaO_3$ substrate without wave guiding layer. The results agree well with the previous studies, which reported low propagation loss for surface acoustic wave propagation along the piezoelectric crystal substrates [81, 137]. Variations in propagation loss *PL* result from a redistribution of acoustic energy: with the wave guiding layer thickness increases, more acoustic energy is propagating in the wave guiding layer while less

acoustic wave energy is propagating in the surface layer of $LiTaO_3$ substrate. *PL* reduction in Fig. 22(a) implies the corresponding decrease in acoustic wave penetration depth into the substrate. As the value of h/λ increases further, the fraction of total acoustic energy guided by the wave guiding layer is appreciably large and the attenuation caused by leaky waves in the substrate is eliminated. Considering that a thin layer of mass loading (surface density $\sigma = 10^{-4}$ kg/m^2) is attached on the surface of the wave guiding layer, and assuming it has the same particle motion as that of the surface of wave guiding layer, the mass sensitivity defined by Eq. (88) versus h/λ is shown in Fig. 22(b) along with the propagation loss change that is calculated by $\Delta(PL)$ normalized by the surface density. The results show that the highest mass sensitivity appears around $h/\lambda = 0.06$, and so does the propagation loss change. Since *PL* is very small and its variation caused by a thin mass loading layer is even smaller, for a Love wave sensor in a vacuum with an elastic wave guiding layer, propagation velocity change or resonance frequency shift should be used to determine the mass loading quantitatively.

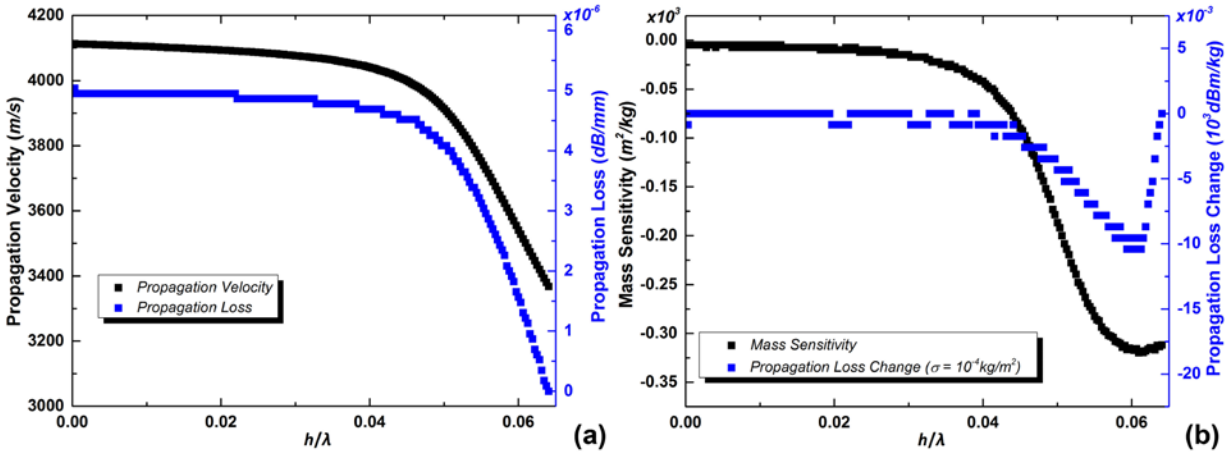

Figure 22. Love wave biosensor with an elastic wave guiding layer in vacuum: (a) propagation velocity and propagation loss (b) mass sensitivity and propagation loss change for a thin layer of mass loading ($\sigma = 10^{-4}$ kg/m^2) attached on the surface of Love wave sensor

As discussed above, some other materials have been evaluated as the wave guiding layer in previous research, including SiO_2, ZnO and PMMA. The corresponding propagation velocity, effective coupling coefficient, propagation loss as well as the mass sensitivity with an increase in the wave guiding layer thickness can be obtained based on the theoretical model proposed, and compared with the results obtained for parylene-C wave guiding layer (Fig. 23). Material properties adopted in calculations are listed as follows: SiO_2, $c_{44} = \mu_{44} = 25\ GPa$, $\rho = 2200\ kg/m^3$ [138]; ZnO, $c_{44} = \mu_{44} = 36\ GPa$, $\rho = 5720\ kg/m^3$ [139]; PMMA, $c_{44} = \mu_{44} = 1.78\ GPa$, $\rho = 1188\ kg/m^3$ [2, 140]. The results indicate that propagation loss *PL* can be limited to quite a low range for all these elastic wave guiding layers, and the maximum *PL* of $0.5\times10^{-6}\ dB/mm$ is obtained when the Love wave propagation along the bare surface of 36º *YX*-$LiTaO_3$ substrate. In comparison, the shear wave velocity υ_s of wave guiding layer ($\upsilon_s = (\mu_{44}/\rho)^{1/2}$) has an important influence in variations of the propagation velocity, coupling coefficient and mass sensitivity. The results indicate that for the sensor with a PMMA wave guiding layer, the coupling coefficient K^2 achieves its peak value 0.07325 at $h/\lambda = 0.061$; and for sensors with SiO_2 and ZnO wave guiding layers, due to their different shear wave velocities, the values of the maximum K^2 are 0.06813, 0.08180 at $h/\lambda = 0.178$ and 0.071, respectively. With an increase in shear wave velocity, the optimal thickness of wave guiding layer for the maximum coupling coefficient and mass sensitivity increases accordingly. The numerical results on $SiO_2/LiTaO_3$ and $ZnO/LiTaO_3$ Love wave sensors agree well with previous studies, which validates the theoretical model proposed in this study [136, 141].

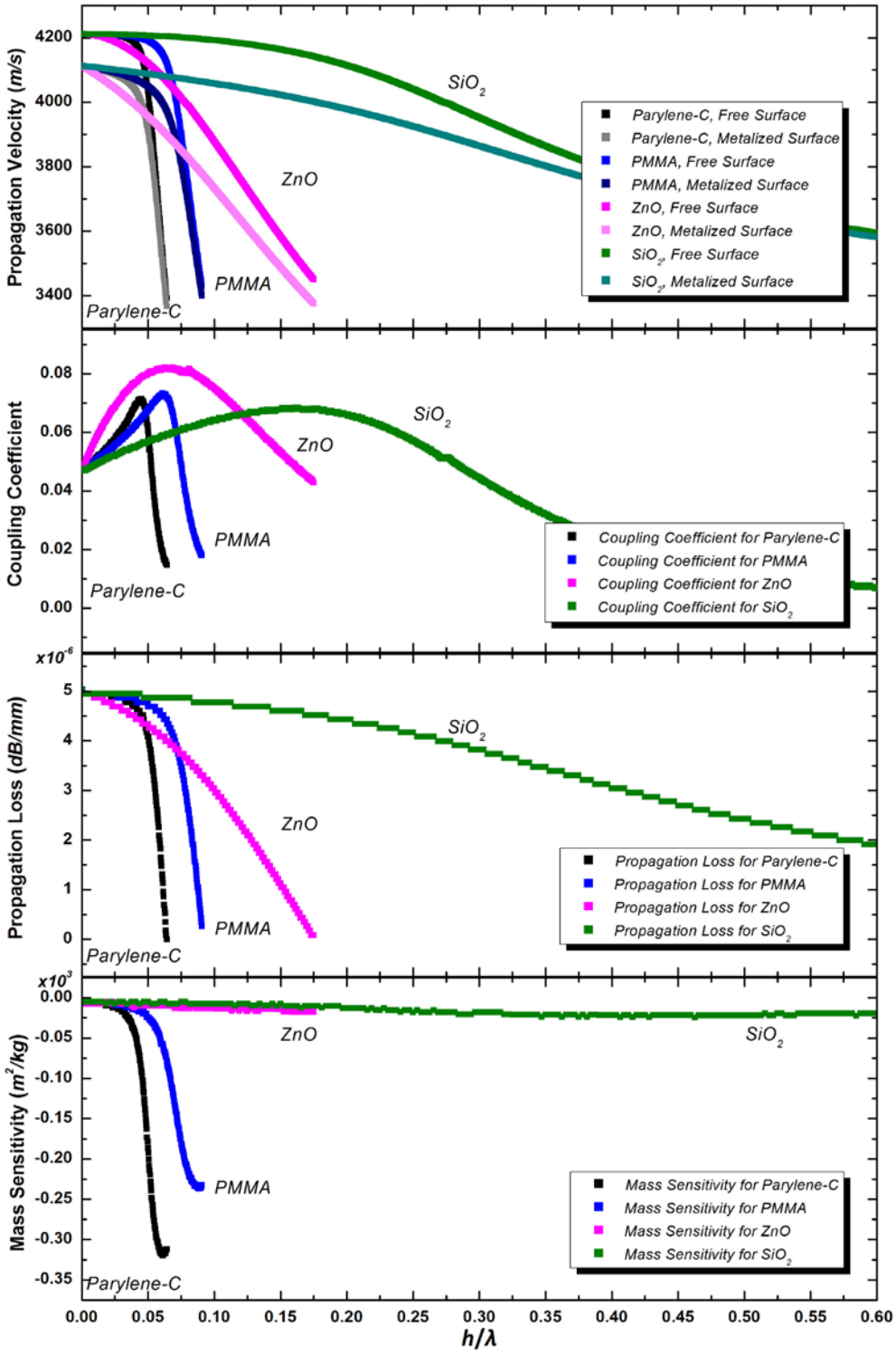

Figure 23. Love wave biosensor with different elastic wave guiding layers in vacuum: (a) propagation velocity (b) coupling coefficient (c) propagation loss (d) mass sensitivity

In the case of a Love wave sensor with a viscoelastic wave guiding layer, the propagation velocity v and propagation loss *PL* versus h/λ are plotted in Fig. 24(a) by setting two different relaxation time τ. There is no evident difference in propagation velocity v between an elastic wave guiding layer and a viscoelastic wave guiding layer; however, propagation loss *PL* shows quite different variation trends and magnitudes for sensors with viscoelastic guiding layers. As the normalized thickness h/λ increases, propagation loss *PL* increases slightly and remains less than1 *dB/mm* at $h/\lambda = 0.04$; and as h/λ increases further, *PL* increases significantly to ~22 *dB/mm* ($\tau = 0.01$ *ns*) and ~44 *dB/mm* ($\tau = 0.02$ *ns*) at $h/\lambda = 0.064$. The change in propagation loss *PL* is caused by the redistribution of acoustic energy: as h/λ increases, the acoustic energy propagating along the wave guiding layer increases accordingly. Compared with an ideal elastic wave guiding layer, the sensor with a viscoelastic wave guiding layer shows an appreciable loss during wave propagation because of its lossy nature. When $h/\lambda > 0.045$, significant amount of acoustic wave energy is trapped in the wave guiding layer, and thus the acoustic wave attenuation in this viscoelastic layer becomes the predominant mechanism of acoustic propagation loss. The corresponding response to a thin layer of mass loading is shown in Fig. 24(b). In comparison with Fig. 22(b), the mass sensitivity, defined by Eq. (88), shows a similar variation tendency, while the loss propagation change ($\Delta(PL)$) increases firstly and then decreases versus h/λ. The maximum mass sensitivity and propagation loss change appear around $h/\lambda = 0.064$, indicating high consistency of the mass-loading response for Love wave sensors with elastic wave guiding layer and viscoelastic wave guiding layer. The results also indicate that as the loss shear modulus of the wave guiding layer increases, propagation loss *PL* at the same value of h/λ increases accordingly, and so does the propagation loss change due to the mass loading. Thus, for a Love wave sensor with a viscoelastic wave guiding layer, it is an advisable way to monitor the

propagation loss variation as propagation velocity change or resonance frequency shift, especially in the steady increase range of *PL* change ($h/\lambda > 0.045$).

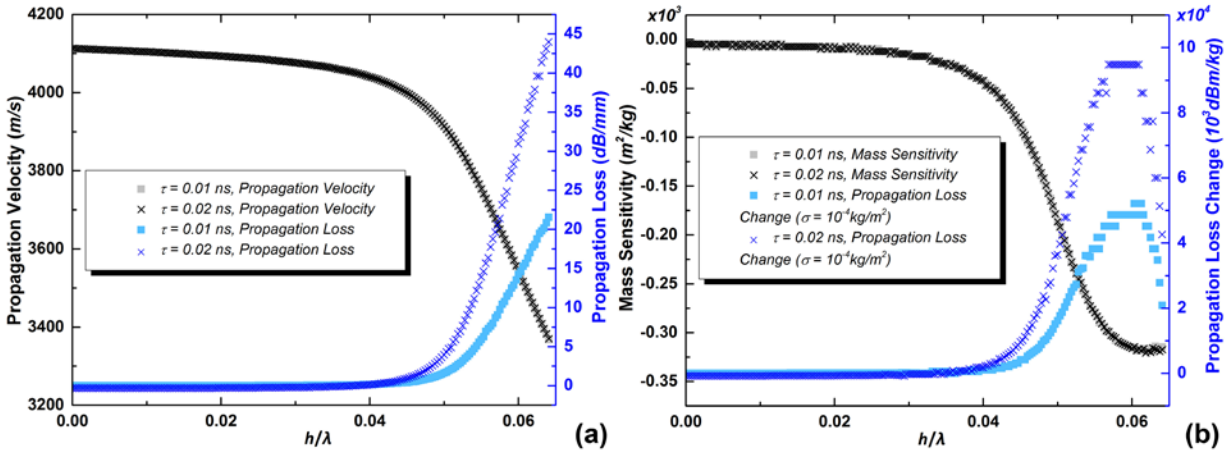

Figure 24. Love wave biosensor with a viscoelastic wave guiding layer in vacuum: (a) propagation velocity and propagation loss (b) mass sensitivity and propagation loss change for a thin layer of mass loading ($\sigma = 10^{-4}$ *kg/m*^{2}) attached on the surface of Love wave sensor

As shown in Fig. 21, for both the elastic wave guiding layer and viscoelastic wave guiding layer, the coupling coefficient K^2 reaches its peak value of 0.07138 at $h/\lambda = 0.045$. On the other hand, this h/λ value is at the initial increasing stage of the mass sensitivity and propagation loss change (Figs. 22 and Fig. 24). Nevertheless, when the mass sensitivity and propagation loss change are at their peak values, the corresponding propagation velocity υ is ~3400 *m/s*, and K^2 is only ~0.02. Thence, the optimal normalized thickness of wave guiding layer (h/λ) cannot be determined by one single criterion, for example, a high coupling coefficient or a large mass sensitivity, but by a more comprehensive consideration. Besides, the relatively high propagation loss due to the viscoelastic nature of the biocompatible polymer guiding layer

should be taken into account as well when designing an efficient Love wave biosensor. A balance is suggested to be made among a large propagation velocity, a high coupling coefficient, a large mass sensitivity and a low propagation loss. For a Love wave biosensor with either an ideal elastic wave guiding layer or a viscoelastic wave guiding layer, the maximum propagation velocity is obtained at $h/\lambda = 0$, and the maximum coupling coefficient and mass sensitivity are found at $h/\lambda = 0.045$ and 0.06, respectively. For a good combination of these performance parameters, the optimal normalized guiding layer thickness should be at the vicinity of $h/\lambda = 0.05$. So, for the Love wave sensor in vacuum with a parylene-C wave guiding layer, the guiding layer thickness should be around 1.6 μm.

5.2.2 A Love Wave Sensor in Liquid

Besides a viscoelastic wave guiding layer, propagation loss can also be induced when the sensing surface is contacting with a viscous liquid, such as the cell culture medium. Fig. 25 shows the variations in propagation velocity v and propagation loss PL as a function of the relevant properties of liquid medium, including the viscosity and density. Both v and PL show an approximate linear relation with respect to the square root of viscosity and density of the liquid medium, though with different slopes. With the viscosity or density increases, v decreases gradually and PL increases. The results agree well with the numerical results of previous studies for the low-viscosity liquid environment, validating the proposed theoretical model [128, 129].

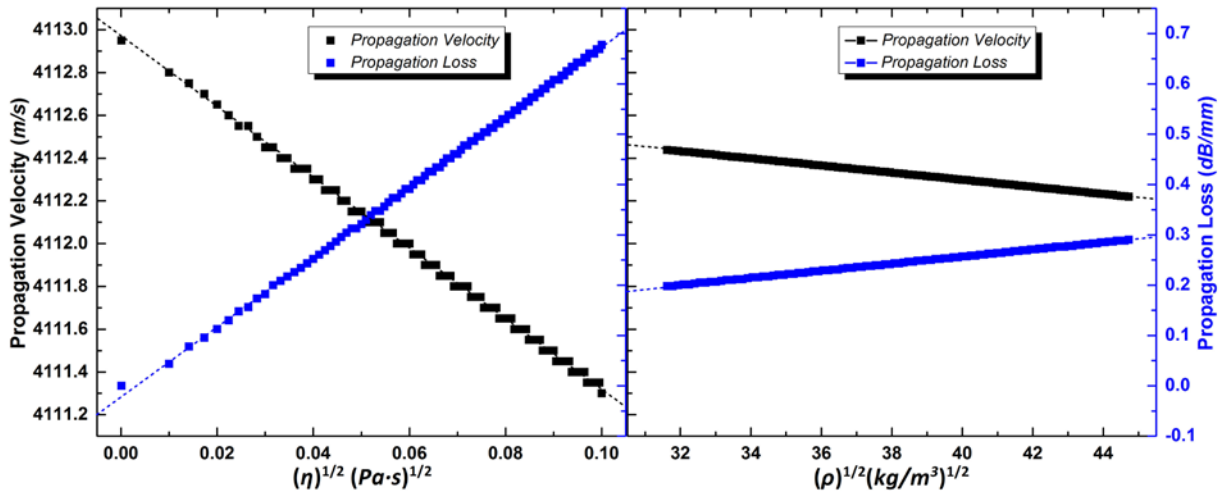

Figure 25. Propagation velocity and propagation loss of Love wave biosensor in liquid

Fig. 26(a) demonstrates the propagation velocity υ and propagation loss *PL* for a Love wave sensor in liquid (water) with an ideal elastic wave guiding layer. It can be seen that υ and *PL* exhibit the opposite variation tendencies with regard to an increasing normalized thickness of wave guiding layer: as h/λ increases, υ decreases and *PL* increases slowly; and as h/λ increases further to >0.04, υ decreases and *PL* increases dramatically. Compared to Fig. 22(a), the propagation velocity υ shows the similar variations versus h/λ, while the propagation loss *PL* becomes relatively large due to the acoustic wave propagation in viscous liquid. From the perspective of energy redistribution, as the normalized thickness h/λ increases, the fraction of total acoustic energy confined in the wave guiding layer is raised; and consequently, attenuation is accumulated gradually at the interface of guiding layer and liquid medium, resulting in an enhanced propagation loss. Assuming that a uniform thin layer of mass loading (surface density $\sigma = 10^{-4}$ kg/m^2) is attached on the surface of the wave guiding layer, the corresponding response to mass loading is shown in Fig. 26(b), in which the mass sensitivity is calculated by the relative propagation velocity change normalized by the surface density, defined in Eq. (88), and

propagation loss change is calculated from $\Delta(PL)$ normalized by the surface density. With an increasing normalized thickness, the mass sensitivity decreases firstly and tends to be stable, while the propagation loss change increases gradually and then decreases. In comparison with the case in vacuum, the mass sensitivity shows the similar variations, reaching its peak value around h/λ = 0.06. However, the peak in propagation loss change curve is shifted slightly to the left side, with the peak value at ~0.058. For a Love wave biosensor with an ideal elastic wave guiding layer, the existence of liquid medium causes considerable propagation loss, and the acoustic loss due to leaky waves in the substrate can be neglected.

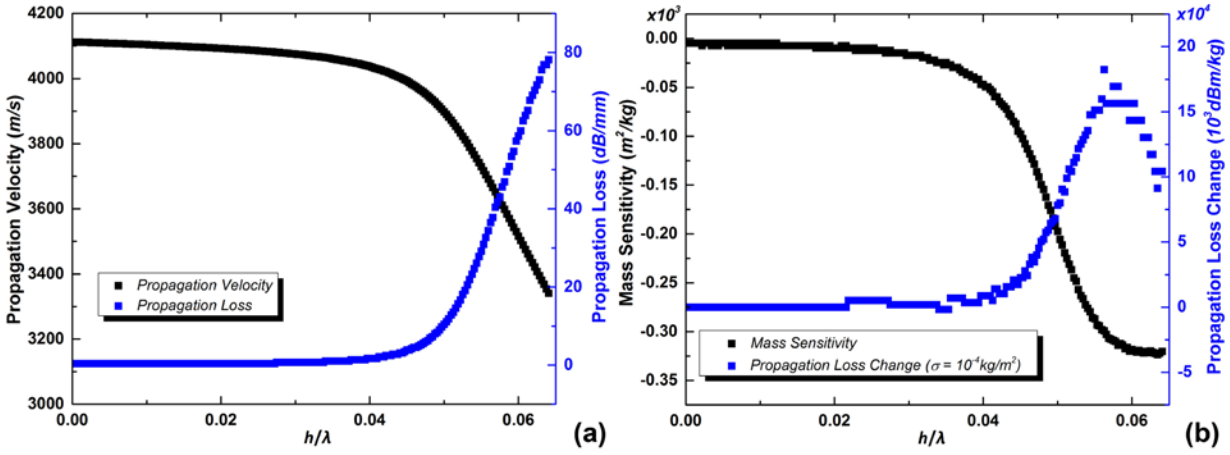

Figure 26. Love wave biosensor with an elastic wave guiding layer in liquid: (a) propagation velocity and propagation loss (b) mass sensitivity and propagation loss change for a thin layer of mass loading ($\sigma = 10^{-4}$ kg/m^2) attached on the surface of Love wave sensor

In the case of a Love wave sensor in liquid with a viscoelastic wave guiding layer, the propagation velocity v and propagation loss PL versus h/λ are shown in Fig. 27(a). As in a vacuum, the propagation velocities show nearly the same changes in liquid for both an elastic

wave guiding layer and a viscoelastic wave guiding layer: with the normalized thickness h/λ increases, v decreases gradually. *PL* also increases continuously versus the h/λ as in Fig. 26(a); however, as h/λ increases to >0.045, *PL* with a viscoelastic wave guiding layer increases faster than that with an ideal elastic one. From Fig. 24(a), Fig. 26(a) and Fig. 27(a), it can be found that both the viscoelastic wave guiding layer and viscous liquid cause considerable propagation loss, especially when most of the acoustic energy is confined in the guiding layer rather than in the surface layer of the substrate. Even for pure water of low viscosity, the Love wave penetration into the liquid induces comparable damping as in a viscoelastic polymer wave guiding layer. Through Fig. 24(a) and Fig. 26(a), the propagation loss *PL* for a Love wave biosensor in liquid with a viscoelastic wave guiding layer can be approximately calculated by adding up the losses caused by each single factor. The corresponding sensor response to a thin layer of mass loading is shown in Fig. 27(b). Compared with Fig. 26(b), both the mass sensitivity and propagation loss change show the similar variation tendencies: the mass sensitivity reaches its peak value around h/λ = 0.06 and the peak in propagation loss change curve is shifted to ~0.058. Similarly, the propagation loss change induced by the mass loading in this case can be approximately estimated by adding the *PL* change in Fig. 24(b) and Fig. 26(b), which indicates the linear-adding characteristic of propagation loss. For a Love wave biosensor in liquid with either an elastic wave guiding layer or a viscoelastic wave guiding layer, the maximum propagation velocity is obtained at h/λ = 0, and the optimal coupling coefficient and mass sensitivity are achieved at h/λ = 0.045 and 0.058, respectively. For a good combination of these performance parameters, the optimal range of normalized wave guiding layer thickness is suggested at the vicinity of h/λ = ~0.048. So, to parylene-C wave guiding layer, it should be ~1.5 μm.

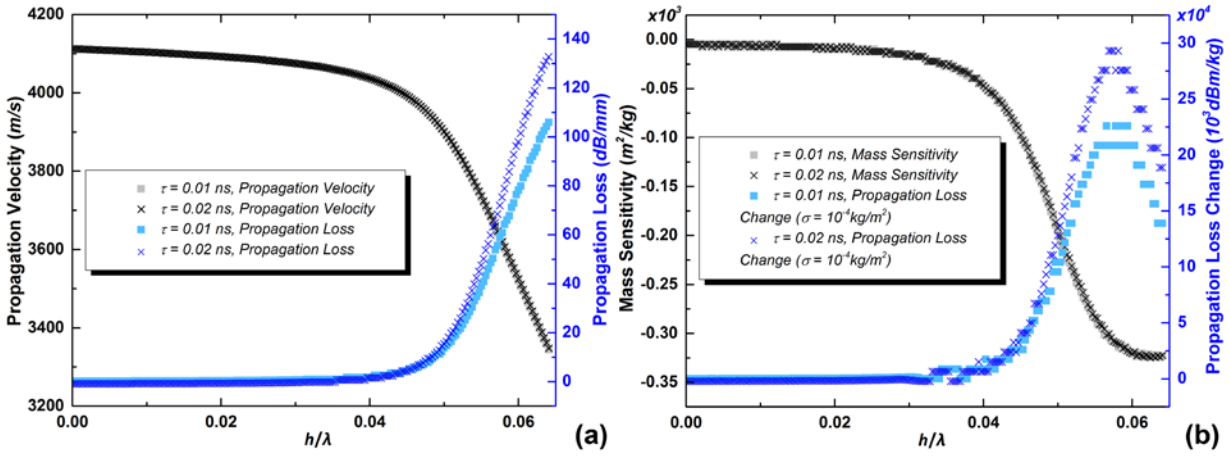

Figure 27. Love wave biosensor with a viscoelastic wave guiding layer in liquid: (a) propagation velocity and propagation loss (b) mass sensitivity and propagation loss change for a thin layer of mass loading ($\sigma = 10^{-4}\ kg/m^2$) attached on the surface of Love wave sensor

The above results show some similar variation patterns with previous studies by *McHale et al*, though the variation magnitudes are different [134, 135]. It is clear from the above modeling results that factors, such as the loss shear modulus of wave guiding layer, viscosity of liquid medium, have significant influence on the acoustic wave propagation loss. For a Love wave sensor, insertion loss is determined by the conversion loss during the electro-acoustic energy inter-conversion in the input and output IDTs, which is determined by the electromechanical coupling coefficient K^2 and the structure of IDTs, as well as the wave propagation loss in the acoustic wave pathway. Regardless of the IDT design, the numerical results reveal that with the wave guiding layer thickness increases initially, the propagation loss remains relatively small, and K^2 increases gradually, which results in an initial decrease in the insertion loss. In addition, since the propagation loss in vacuum is much smaller than that in liquid, the decrease in the insertion loss in vacuum is more noticeable as compared to that in liquid. As the layer thickness increases further, the propagation loss becomes significant and

exceeds the influence of K^2, leading to an increase in the insertion loss. The numerical results in the resonance frequency shift and insertion loss variation show the similar tendencies with other previous experimental results, though the magnitudes vary by some extent [48, 55, 127, 142]. In choosing the optimal thickness for the wave guiding layer, a compromise should be made between a low insertion loss and a high mass sensitivity. For a Love wave biosensor with an elastic wave guiding layer or a viscoelastic wave guiding layer, the optimal wave guiding layer thickness is found to be at the vicinity of h/λ = ~0.05 in vacuum, and ~0.048 in liquid (water).

5.3 A LOVE WAVE BIOSENSOR TO MONITOR THE CELL ADHESION PROCESS

As discussed in Session 1.1.1, during the past decades, interest in development of the cell-based biosensors has increased considerably. A variety of sensors have been developed as the cell-based biosensors, and some of them have been proven a great success and thus put into commercial production. The significant feature of cell-based biosensors is to use living cells as the detected objects or the receptors to other stimulus from surrounding environment [4]. With cells as the sensing elements, their basic physiological reactions to different external stimulus are observed, which can be widely applied in drug development, quality control and environment monitoring. Thus, as the crucial cellular behavior as introduced in Session 3.1.1, cell adhesion onto the sensing surface is a necessary prerequisite for the cell-based biosensor applications as well. As one of the most promising probing methods in biomedical research and diagnosis, a 36º *YX*-$LiTaO_3$ based Love wave sensor with a parylene-C wave guiding layer is adopted to monitor the adhesion process of cells.

5.3.1 Effect of Adherent Cells on the Sensor Response

From the theoretical model discussed in Session 2.4, a series of numerical results are obtained on a 36º *YX*-$LiTaO_3$ based Love wave biosensor. Similar parameters are adopted as in previous sessions. The period of Au/Ti IDTs is $\lambda = 32\ \mu m$, and the parylene-C film with the thickness h_1 is deposited on the surface of Au/Ti films as the wave guiding layer. In addition, with the cell culture medium as the liquid medium in computation which has the similar properties with pure water, the values of $\rho_M = 1000\ kg/m^3$, $\eta_M = 0.00102$ are used. The performance of the Love wave biosensors, such as resonance frequency or insertion loss, is affected by a series of factors in various degrees. In previous sessions, these factors were evaluated separately through a comprehensive theoretical analysis. When choosing the optimal thickness of wave guiding layer, a balance is suggested to be made among a large propagation velocity, a high coupling coefficient, a large mass sensitivity and a low propagation loss. For a Love wave biosensor with either an elastic wave guiding layer or a viscoelastic wave guiding layer, an optimal normalized guiding layer thickness is considered at the vicinity of h_1/λ = ~0.05 in vacuum, and ~0.048 in liquid (water). For parylene-C, the corresponding thickness should be 1.5~1.6 μm. Thus, in this session, a 36º *YX*-$LiTaO_3$ based Love wave biosensor with 1.6-μm parylene-C guiding layer is adopted for monitoring the adhesion process of cells.

In the meantime, from Eq. (73), (74), the response of the Love wave sensors also strongly depends on the density and viscoelasticity of adherent cells (ρ_P, c_P). In our previous work, the quartz TSM resonator was applied to characterize the viscoelastic properties of aging and young TSCs bounded on its surface. TSCs were isolated from both old and young rats, and allowed to grow to confluency on the surface of TSM resonators. The admittance spectrums of TSM resonators with adherent TSCs were acquired, and a series of complex shear modulus $G' + jG''$ as

well as the average thickness of TSC monolayer were calculated based on a two-layer-loading transmission line model (TLM). With the preset density of 1.00 g/cm^3, the viscoelasticity of aging and young TSCs are 21608 + 136209*j Pa* and 985 + 116582*j Pa*, respectively. According to the viscoelasticity theory shown in Eq. (89), (90), complex shear modulus $c_P = G' + jG''$ is dependent on the oscillation frequency ω. As G_0 = constant, $G' \infty f^{\gamma}$. When γ is assigned with 0.12, storage modulus G' of aging and young TSCs at 128 *MHz* is calculated as 29341 *Pa* and 1337 *Pa*, respectively. When γ = 0.14, G' turns out to be 30876 *Pa* and 1407 *Pa*. In addition, based on this frequency-dependent relation, in relatively low frequencies, $G'' \infty f^{\gamma}$ as G_0 = constant and viscous damping coefficient μ is ignored; and with frequency-dependent relation is eliminated at the high frequencies and μ becomes the dominant factor, $G'' \infty f$. However, as shown in Eq. (72), with a further increase in frequency, the loss shear modulus of soft materials cannot increase continuously. Similar results can be found in related experiments: when the measurement frequency increased over 100 *MHz*, there was a reverse decrease in the loss shear modulus of polymers [143, 144]. So, an approximation center value of converted viscoelasticity at a high frequency (~128 *MHz*) of 2000 + 100000*j Pa* is used for adherent cells in this session. The G' and G'' as statistical stiffness and viscosity of cell monolayer, can exhibit the characteristic viscoelasticity of individual cell in a group.

After the center value of cellular viscoelasticity of 2000 + 100000*j Pa* is determined, the propagation velocity υ and propagation loss *PL* for a Love wave sensor with adherent cells are calculated based on the theoretical model discussed in Chapter 2. In both Fig. 28 and Fig. 29 (pink dot), it can be seen that as the thickness of adherent cell layer h_2 increases, the propagation velocity υ increases, and the propagation loss *PL* decreases. Evident changes in υ and *PL* are observed in the early stage of an increase in cell layer thickness ($h_2 < 6$ *nm*). With h_2 increases

further to >10 *nm*, both v and *PL* tend to be stable without any more obvious variations. The peak value of propagation velocity v is obtained at h_2 = ~8 *nm*, leading to the maximum resonance frequency of a Love wave sensor in the adhesion process of cells with a shear modulus of 2000 + 100000*j Pa*.

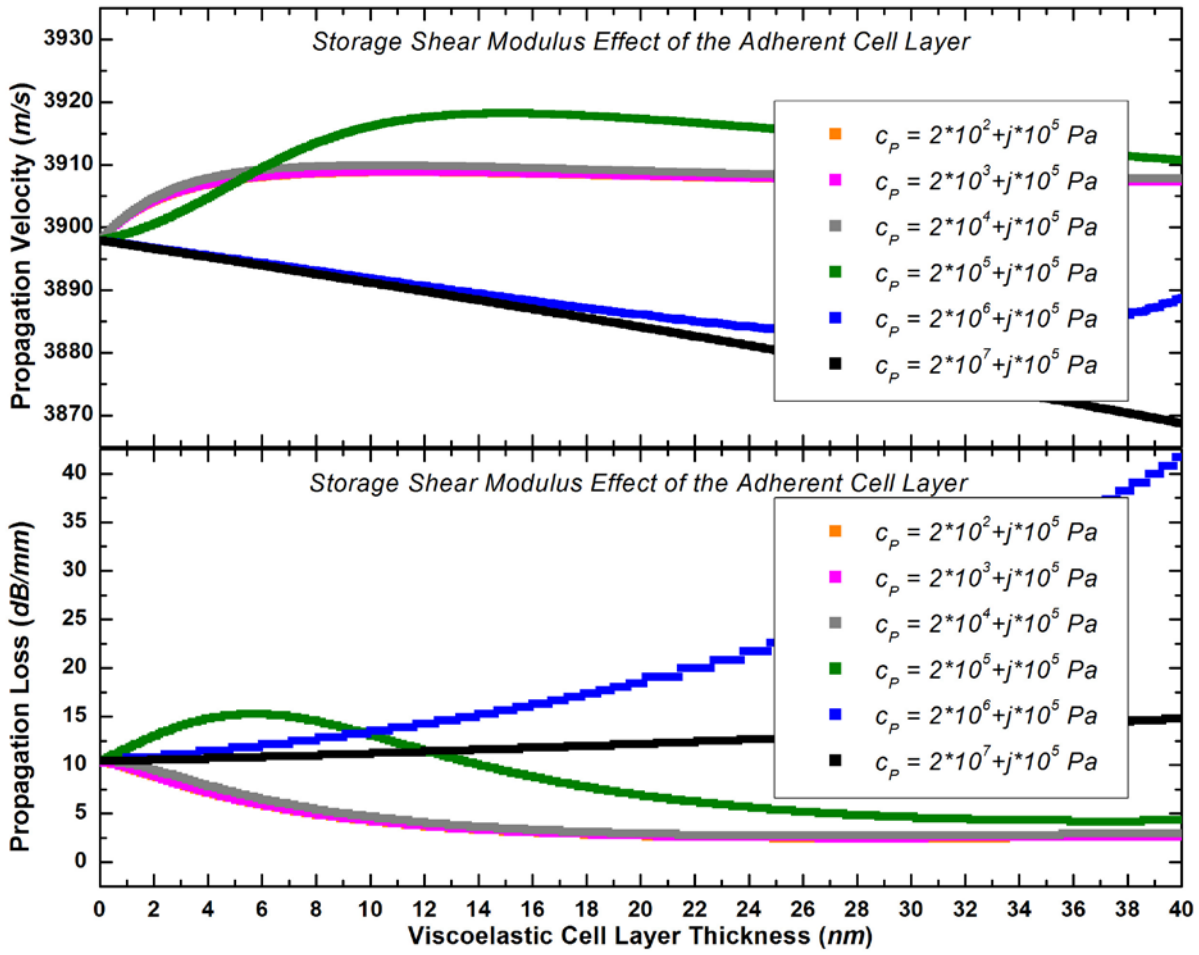

Figure 28. Propagation velocity and propagation loss of cell-based Love wave biosensor with a 1.6-μm parylene-C wave guiding layer: with the adherent cell layer of different storage shear modulus (loss shear modulus of 10^5 *Pa*)

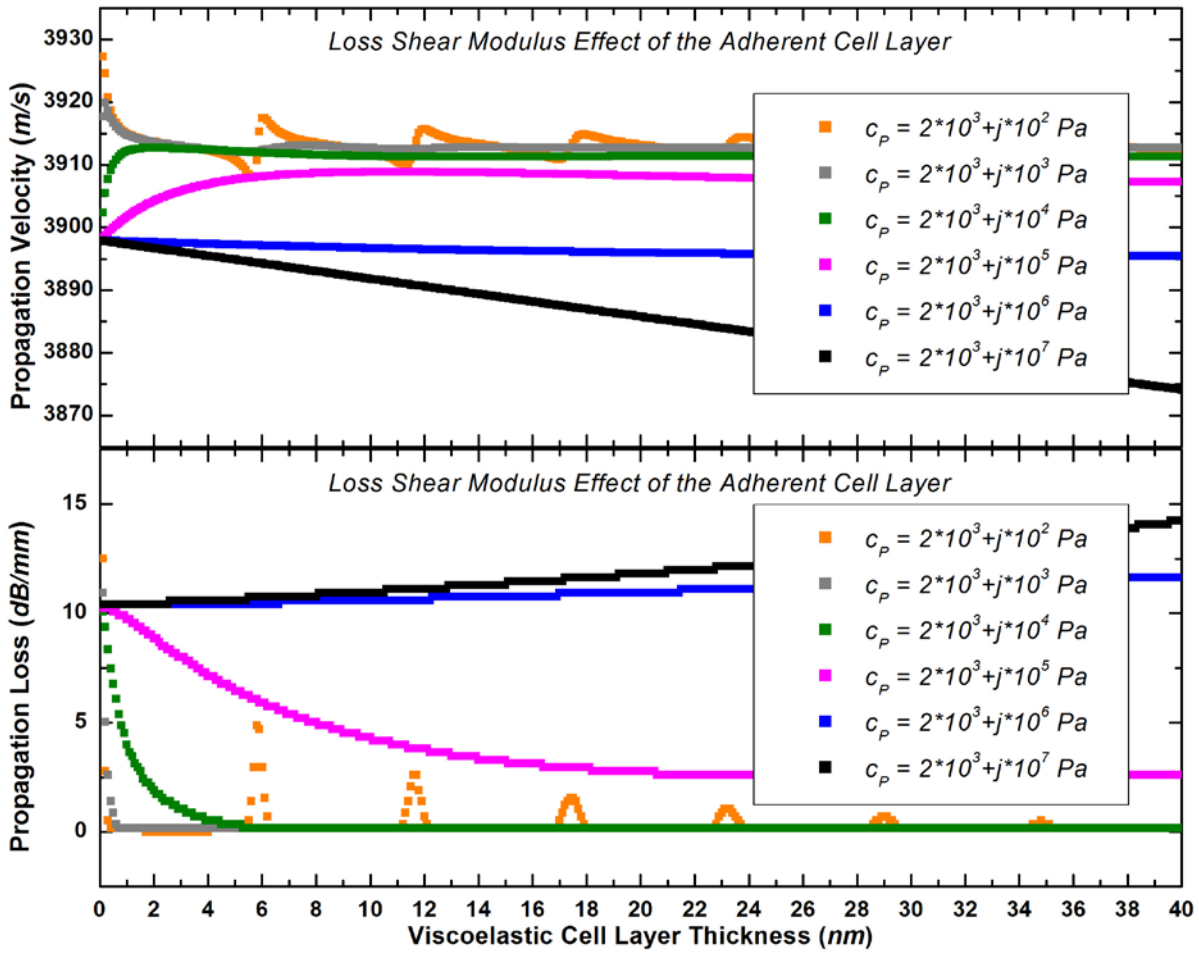

Figure 29. Propagation velocity and propagation loss of cell-based Love wave biosensor with a 1.6-μm parylene-C wave guiding layer: with the adherent cell layer of different loss shear modulus (storage shear modulus of 2×10^3 *Pa*)

Different variations in propagation velocity υ and propagation loss *PL* of Love wave sensors versus the adherent cell layer thickness h_2 can be caused by adherent cells of different storage or loss shear modulus. Fig. 28 shows a set of curves for the Love wave sensors with adherent cell layer of continuously varying storage modulus from 2×10^2 *Pa* to 2×10^7 *Pa* and fixed loss modulus 1×10^5 *Pa*. When the storage shear modulus of cell layer is small ($\leq2\times10^4$ *Pa*), the υ and *PL* curves do not show significant differences among different modulus values. With the storage shear modulus increases further, variations in υ and *PL* with respect to h_2 start

to show different tendencies. In case of the shear modulus $G' = 2\times10^5$ *Pa*, as the adherent cell layer thickness h_2 increases, propagation velocity υ increases gradually and then decreases, achieving its peak value at h_2 = ~14 *nm*; and propagation loss *PL* increases slightly and then decreases dramatically, with the peak value obtained at h_2 = ~6 *nm*. As the storage modulus of adherent cells ascends to 2×10^6 *Pa*, υ decreases and then increases with respect to h_2, and *PL* increases continuously. Until the storage shear modulus is 2×10^7 *Pa*, υ decreases and *PL* increases with an increase in h_2. Fig. 29 shows the curve sets of propagation velocity υ and propagation loss *PL* versus cell layer thickness h_2 for the cell layer of fixed storage modulus 2×10^3 *Pa* and continuously varying loss modulus from 1×10^2 *Pa* to 1×10^7 *Pa*. The results indicate that under the relatively small storage shear modulus (2×10^3 *Pa*), adherent cells of small loss shear modulus ($\leq1\times10^4$ *Pa*) cannot cause continues, stable variations in υ and *PL* of the Love wave sensors: a series of high-order resonance peaks are observed in case of the loss modulus $G'' = 1\times10^2$ *Pa* or 1×10^3 *Pa*; and in case of $G'' = 1\times10^4$ *Pa*, with an initial small growth in cell layer thickness h_2, υ ascends rapidly and *PL* descends. As the loss modulus increases further to $\geq1\times10^5$ *Pa*, variations in both propagation velocity υ and propagation loss *PL* become stable with respect to h_2. In case of the loss modulus $G'' = 1\times10^6$ *Pa* and 1×10^7 *Pa*, with the adherent cell layer thickness h_2 increases, υ decreases gradually and *PL* increases. Thus, the clear, stable, characteristic variations in propagation velocity υ and propagation loss *PL* of Love wave sensors can be observed when the storage and loss shear modulus of the adherent cell layer are in an appropriate range. The numerical results demonstrate the potential of Love wave sensors in providing useful quantitative measures on cellular viscoelasticity during the adhesion process, indicating an advisable method to real-time monitor the structural and mechanical properties of adherent cells under multiple physiological conditions.

5.3.2 Effect of Parylene-C Layer on the Sensor Response

In Fig. 28 and Fig. 29, an optimal thickness of 1.6 μm is adopted for parylene-C wave guiding layer. Fig. 30 shows the response of Love wave sensors with parylene-C wave guiding layers of various thicknesses in the adhesion process of cells with a shear modulus of $2000 + 100000j\ Pa$. Considering the parylene-C wave guiding layer as a pure elastic layer, it can be seen that both the propagation velocity υ and propagation loss PL versus the cell layer thickness h_2 exhibit the similar variation tendencies for the guiding layers of different thicknesses, though the variation ranges and magnitudes are different. As h_2 increases firstly, propagation velocity υ increases gradually and propagation loss PL decreases; and as h_2 increases further, both υ and PL tend to be stable. The results from the previous sessions indicate that for a Love wave sensor applied in a liquid medium, with the guiding layer thickness increases, the characteristic propagation velocity υ decreases and propagation loss PL increases. In Fig. 30, it can be found from the starting points of curves: in the beginning, with the parylene-C layer thickness increases ($\leq$1.0 μm), υ decreases slightly and its value is still >4000 m/s, and PL remains <2 dB/mm; and as the thickness increases further to $\geq$1.5 μm, υ decreases dramatically to <4000 m/s and PL increases to >5 dB/mm. In the meantime, the ending points of the two curve sets at h_2 = 40 nm keep the same variation tendencies as well. In addition, when the parylene-C layer is relatively thin ($\leq$1.0 μm), as the adherent cell layer thickness h_2 increases, the propagation velocity υ increases slightly, and propagation loss PL does not show any evident change. Until the parylene-C layer thickness increases to $\geq$1.5 μm, with an increase in h_2, υ increases and PL decreases dramatically. The differences in variation range and magnitude of propagation velocity υ and propagation loss PL can provide a new perspective to determine the optimal thickness of parylene-C wave guiding layer, which further validates the conclusions from previous sessions.

Even though with different variation ranges and magnitudes, it is important to note that for the adherent cell layer of $2000 + 100000j\ Pa$, both sets of υ and PL curves enter a plateau as the cell layer thickness h_2 is >20 nm. 20 nm is quite a small thickness, which can be attributed to the significant attenuation of Love waves in viscoelastic cell layer. From this perspective, when applying the Love wave sensor to monitor the adhesion process of cells, the sensor response will be primarily induced by the initial interaction between attached cells and the substrate during the early stage of cell adhesion process. The initial formation of the adherent cell layer can result in a reduction in propagation loss PL.

In comparison, the adhesion process of TSCs was also monitored by TSM resonators in previous work. Admittance spectrums of TSM resonators with TSC suspensions were acquired, and the corresponding resonance frequencies were extracted from them. In the beginning, as a great number of TSCs fell down and attached to the electrodes, the resonance frequency shift decreased sharply. With more and more TSCs finished attachment, started to spread and formed focal adhesions, the viscoelasticity of attached cells changed accordingly, and the resonance frequency shift of TSM resonators increased and then decreased again. Compared with TSM resonators, the trigger of Love wave sensor response is primarily limited to the formation of bonds between cells and the substrate. Attributed to a larger decay distance of acoustic wave penetration into the liquid medium, the response of TSM resonators may be affected by more unexpected surrounding factors. The Love wave sensor exhibits high sensitivity to surface perturbations, especially bonds formed within the relatively short distance from the surface, indicating their potential on investigating subtle interactions between cell membrane and the substrate involved in a variety of cellular activities.

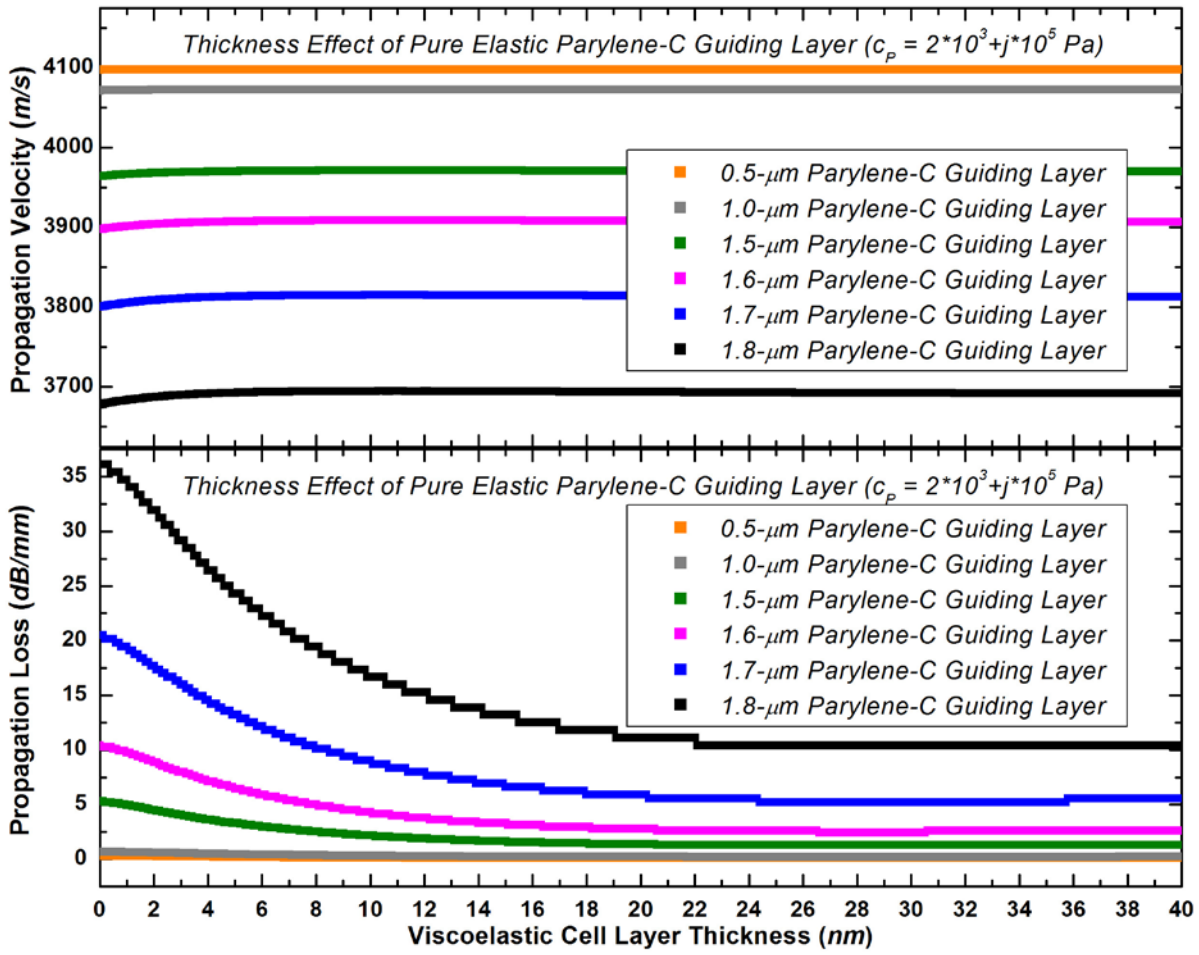

Figure 30. Propagation velocity and propagation loss of cell-based Love wave biosensor with a pure elastic parylene-C wave guiding layer of different thicknesses ($c_P = 2\times10^3 + j\times10^5$ *Pa*)

In addition, in the discussions above, the parylene-C wave guiding layer is considered as a pure elastic layer. However, as a viscoelastic polymer, the viscous effect of parylene-C layer should be taken into account as well. Propagation velocity v and propagation loss *PL* versus the adherent cell layer thickness h_2 is shown in Fig. 31 for a Love wave sensor with either an elastic wave guiding layer or a viscoelastic wave guiding layer. Both the propagation velocity v and propagation loss *PL* show the quite similar variation tendencies for an elastic wave guiding layer and a viscoelastic wave guiding layer: with the adherent cell layer thickness h_2 increases, v

increases rapidly and then decreases slightly, and *PL* decreases continuously and tends to be stable. As the relaxation time τ increases from 0 (for the pure elastic case) to 0.02 *ns*, the curve of the propagation velocity υ shifts to a higher velocity range, and propagation loss *PL* moves to a larger loss zone, leading to an increase in both resonance frequency and insertion loss of Love wave sensors. The results indicate that for a Love wave sensor with the wave guiding layer of certain thickness, the viscosity of guiding layer only has limited influence in the change range of υ and *PL*, but not their variation tendency.

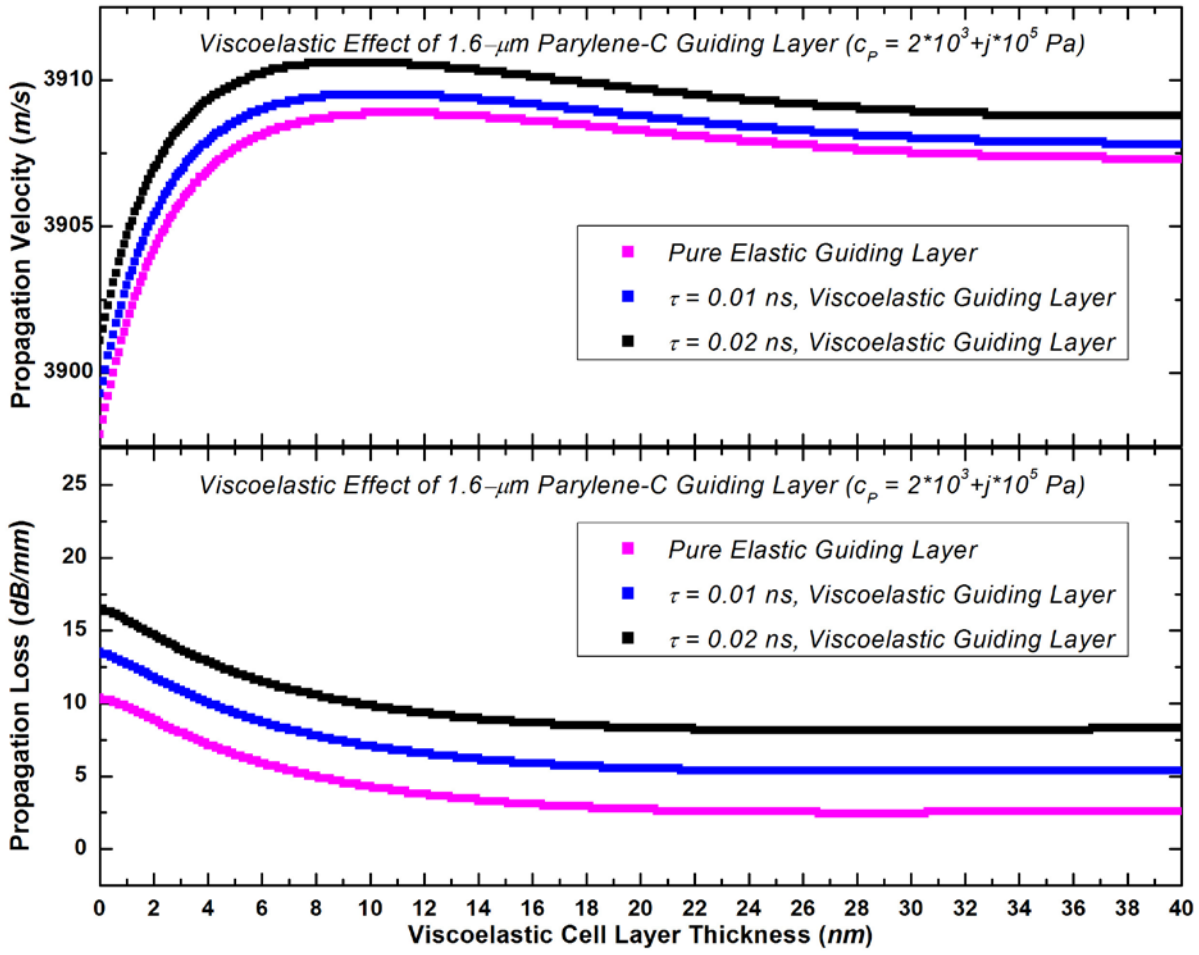

Figure 31. Propagation velocity and propagation loss of cell-based Love wave biosensor with 1.6-μm pure elastic and viscoelastic parylene-C wave guiding layers ($c_P = 2\times10^3 + j\times10^5\ Pa$)

5.4 CONCLUSIONS

In this chapter, a theoretical model is developed for the 36º *YX*-$LiTaO_3$ based Love mode SAW sensor with a parylene-C wave guiding layer. From the theoretical modeling, Love wave propagation in different layers, including the wave guiding layer, adherent cell layer and liquid medium are described. For Love mode SAW sensor with either an elastic or a viscoelastic wave guiding layer, the effects of wave guiding layer thickness and liquid medium on the effective electroemechanical coupling coefficient K^2, the propagation loss *PL*, as well as the mass sensitivity of the sensor in response to a thin layer of mass loading are investigated systematically based on this model. The results demonstrate that the maximum propagation velocity occurs at $h/\lambda = 0$; and the optimal coupling coefficient and mass sensitivity can be obtained at $h/\lambda = 0.045$ and $h/\lambda = \sim 0.06$ in vacuum or ~0.058 in liquid (water), respectively. For a good combination of all these performance parameters, it is suggested that the optimal wave guiding layer thickness in a Love wave sensor is at the vicinity of $h/\lambda = \sim 0.05$ in vacuum, and ~0.048 in liquid (water). In addition, this Love wave sensor is applied as a cell-based biosensor to monitor the adhesion process of cells. The effects of viscoelastic cell layer and wave guiding layer on both the propagation velocity υ and propagation loss *PL* are investigated. The numerical results indicate that the adherent cells of various storage or loss shear modulus in certain range can induce evident, characteristic variations in υ and *PL*, revealing the potential of Love wave sensors in providing useful quantitative measures on cellular mechanical properties. In comparison, the thickness and viscosity of parylene-C wave guiding layer have limited influence in the changes of υ and *PL* of Love wave sensors. Compared with TSM resonator, the response of Love wave sensor to the cell adhesion is primarily induced by the formation of bonds between

cells and the substrate. The theoretical model proposed in this study is validated for designing a Love wave biosensor, which can contribute to the Love wave sensor applications.

6.0 A SENSITIVITY-ENHACED LOVE-MODE ACOUSTIC WAVE BIOSENSOR WITH A PHONONIC WAVE GUIDING LAYER

In this chapter, a Love wave sensor with phononic parylene-C wave guiding layer is proposed, where arrays of a different material (filling material) are fabricated on the surface of parylene-C films. The effects of the structural design parameters (period length and period number) and the filling material's properties (density and elasticity) on the stop band of phononic structure are investigated. The results illustrate that with specific combination of related parameters, only the acoustic waves at the vicinity of resonance frequency can propagate through the sensing area of Love wave sensor, when signals of other frequencies are stopped by the phononic patterns. The numerical results from both analytical solution and finite element method (FEM) can reach good agreement with each other, indicating a potential Love wave sensor with high sensitivity and reliability in the cell biology applications.

6.1 INTRODUCTION

Photonic crystals are periodic optical structures, which have a band gap that can forbid the propagation of light in a certain frequency range. Photonic crystals are an attractive sensing platform as they can provide strong light confinement. A wide range of photonic crystal sensing devices has been reported recently [145, 146]. Phononic crystals are periodic composite

materials with an important structural feature; periodic scattering centers whose elastic property is different from a homogeneous matrix surround these scattering centers. Similar to the optical properties in photonic crystals, acoustic waves in certain frequencies cannot propagate through this kind of structure with periodic scattering centers (stop band), thus providing an advisable platform for noise signal filtering [147, 148]. In 1993, Kushwaha *et al* firstly proposed a "phononic" band gap of the periodic elastic composites - a repetitive structure composed of two materials with different elastic properties [149]. It was indicated that quite a large contrast of the elastic properties can realize a full phononic gap; and in the meantime, this acoustic band structure of periodic elastic composites is possible in the presence of a low density of state rather than a full band gap as well. Then in 1998, Montero *et al* and Sanchez-Perez *et al* presented their experimental observations of the phononic band gap in periodic elastic composites, proving the existence of phononic crystals [150, 151]. So far, a number of studies have been explored on the theoretical calculation and experimental observations of phononic crystals. The researchers have made considerable progress on the theoretical analysis of the band gap formation, defect states, and the wave guiding of phononic structure [152-158].

Recently, as the interest in applications of acoustic wave sensors increases continuously, the acoustic wave sensors employing the phoninic structure was studied. Some studies reported that the acoustic wave sensor utilized specific transmission windows within the band gap to determine properties of materials (liquid in most cases) that build the phononic crystals [159-162]. The sensitivity to variations in acoustic wave phase velocity and density of liquid confined in grooves has been proven to be much higher than that in traditional measurements [163]. However, for most reported applications, acoustic waves are propagating in bulk and plate, or in Rayleigh mode, and the application of Love wave sensor with a phononic structure is relatively

limited. Love mode SAW sensor is a promising tool in fundamental biology and biomedical engineering. The Love wave sensor can detect a given chemical or biochemical reagent in liquid on its surface in a non-invasive, simple and quantitative manner, even in a low amount. This type of sensor can be widely applied not limited in environment monitoring and toxicity testing, but also in drug screening, food industry and anti-bioterrorism practice. Presently, although previous research reported some structural and functional optimization concerning the Love wave sensor, more efforts need be devoted to improve the sensor performance in measurements and applications. Liu *et al* presented a Love wave band gap through a microfabricated phononic structure consisting of a 2-dimensional periodically etched silica film on the quartz crystal [164]. Also, Li *et al* reported an improved insertion loss and an increased sensor sensitivity of a Love wave biosensor by 2-dimensional microcavities on the quartz substrate [165]. Besides, Cular *et al* studied the effect of microcavities on the $LiTaO_3$ crystal substrate on the sensor sensitivity through FEM simulation [166]. Nevertheless, in order to improve the performance of Love wave sensor, some of those designs cannot be carried out in experiments easily, and some are lacking the corresponding theoretical analysis to guide the design optimization. Based on a mature theoretical model, the theoretical calculation should be conducted accordingly to provide the optimal structural design parameters for the Love wave biosensor with a high sensitivity and reliability.

6.2 PARAMETER OPTIMIZATION BY THEORETICAL MODEL ANALYSIS

6.2.1 Theoretical Model and Analysis Methods

As in Session 2.2.1 and Session 2.4.1, in order to analyze the acoustic wave propagation in a parylene-C-based phononic wave guiding layer, a Cartesian coordinate system x_1, x_2, and x_3 is established, where x_1-axis is parallel to the direction of SH-SAW propagation, x_2-axis is in the polarization direction and x_3-axis is perpendicular to the surface of piezoelectric crystal substrate. The substrate occupies the domain of $x_3 \leq 0$, which is considered semi-infinite. The wave guiding layer occupies the domain of $0 \leq x_3 \leq h$. Fig. 32 schematically presnets the basic structure of a phononic wave guiding layer on the 36˚ *YX*-$LiTaO_3$ piezoelectric crystal substrate. The wave guiding layer is composed of two kinds of materials, the base material (A) and filling material (B). The period length of the phononic patterns is $d = h_A + h_B$, where the length of material A and B are respectively h_A and h_B. The period number is set as n. The base material (A) is parylene-C. Two kinds of materials are adopted as the filling materials (B), SiO_2 and ZnO. As discussed above, SiO_2 and ZnO films have been widely used as wave guiding layers in Love wave sensors. They are easy to prepare, and have relatively good biocompatibility, which is important for cell-based biosensor applications. Material properties adopted in the calculation are listed as follows: parylene-C, $c_{44} = 0.985\ GPa$, $\rho = 1298\ kg/m^3$; SiO_2, $c_{44} = 25\ GPa$, $\rho = 2200\ kg/m^3$ [138]; ZnO, $c_{44} = 36\ GPa$, $\rho = 5720\ kg/m^3$ [139].

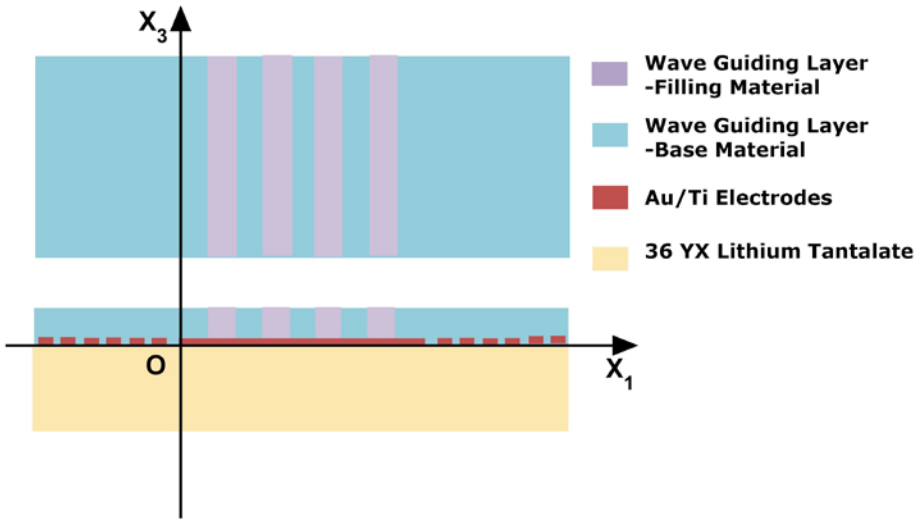

Figure 32. Schematic diagram of a Love wave sensor with a phononic wave guiding layer

A. Love Wave Propagation in Phononic Wave Guiding Layer

For 36° *YX*-$LiTaO_3$ substrate, the predominant component of surface acoustic waves has a shear horizontal polarization along the propagation direction x_1. In the phononic wave guiding layer, the density and elastic stiffness of the base material (A) and filling material (B) are set to be ρ_A, ρ_B and c_A, c_B respectively. Ignoring the variations of the particle movement along the x_3-axis, the corresponding particle displacement along x_2-axis u_{iA}, u_{iB} in the ith period have a simplified form as follows:

$$\begin{aligned} u_{iA} &= (M_{iA}e^{jk_A x_1} + N_{iA}e^{-jk_A x_1})e^{j\omega t} \\ u_{iB} &= (M_{iB}e^{jk_B x_1} + N_{iB}e^{-jk_B x_1})e^{j\omega t} \end{aligned} \tag{91}$$

where the wave number $k = k_0 - j\alpha = \omega/\upsilon - j\alpha$ ($\alpha > 0$), υ is the propagation velocity, α is the attenuation factor of wave propagation ($\alpha << 1$ for pure elastic wave guiding layer), and

$$\begin{aligned} k_A &= (c_A / \rho_A)^{1/2} \\ k_B &= (c_B / \rho_B)^{1/2} \end{aligned} \tag{92}$$

i is assigned with from 1 to n, and n is the repeated period number. M_{iA}, M_{iB}, N_{iA}, N_{iB} are the coefficients to be determined by the boundary conditions. From the particle displacement, the stress on x_2- x_3 contact plane along x_2-axis in wave guiding layer can be calculated as

$$\begin{aligned} T_{iA} &= jk_A c_A (M_{iA} e^{jk_A x_1} - N_{iA} e^{-jk_A x_1}) e^{j\omega t} \\ T_{iB} &= jk_B c_B (M_{iB} e^{jk_B x_1} - N_{iB} e^{-jk_B x_1}) e^{j\omega t} \end{aligned} \tag{93}$$

There are a series of undetermined coefficients (M_{iA}, M_{iB}, N_{iA}, N_{iB}) in u_{iA}, u_{iB} expressions. For the phononic patterns with the period number of n, $4n$ undetermined coefficients need be determined though $4n$ independent boundary relations. Assuming

$$\begin{aligned} &\delta_{iA} = e^{-jk_A(ih_A+(i-1)h_B)}, \bar{\delta}_{iA} = e^{-jk_A(ih_A+ih_B)}, \delta_{iB} = e^{-jk_B(ih_A+(i-1)h_B)}, \bar{\delta}_{iB} = e^{-jk_B(ih_A+ih_B)} \\ &\lambda_A = jk_A c_A, \lambda_B = jk_B c_B \end{aligned} \tag{94}$$

where h_A, h_B are the length of basic material and filling material strips. The period length of phononic structure $d = h_A + h_B$, and usually $h_A = h_B$. Based on the continuity of displacement and shear stress at the contact interfaces,

$$\begin{bmatrix} 1 & 1 & 0 & 0 & 0 & 0 & 0 & ... & 0 & 0 \\ \delta_{1A} & \delta_{1A} & -\delta_{1B} & -\delta_{1B} & 0 & 0 & 0 & ... & 0 & 0 \\ \lambda_A\delta_{1A} & -\lambda_A\delta_{1A} & -\lambda_B\delta_{1B} & \lambda_B\delta_{1B} & 0 & 0 & 0 & ... & 0 & 0 \\ 0 & 0 & \bar{\delta}_{1B} & -\bar{\delta}_{1B} & -\bar{\delta}_{1A} & \bar{\delta}_{1A} & 0 & ... & 0 & 0 \\ 0 & 0 & \lambda_B\bar{\delta}_{1B} & -\lambda_B\bar{\delta}_{1B} & -\lambda_A\bar{\delta}_{1A} & \lambda_A\bar{\delta}_{1A} & 0 & ... & 0 & 0 \\ 0 & 0 & 0 & 0 & \delta_{2A} & \delta_{2A} & -\delta_{2B} & ... & 0 & 0 \\ 0 & 0 & 0 & 0 & \lambda_A\delta_{2A} & -\lambda_A\delta_{2A} & -\lambda_B\delta_{2B} & ... & 0 & 0 \\ ... & ... & ... & ... & ... & ... & ... & ... & ... & ... \\ 0 & 0 & 0 & 0 & 0 & 0 & 0 & ... & -\lambda_B\delta_{nB} & \lambda_B\delta_{nB} \\ 0 & 0 & 0 & 0 & 0 & 0 & 0 & ... & \lambda_B\bar{\delta}_{nB} & -\lambda_B\bar{\delta}_{nB} \end{bmatrix}$$

$$\begin{bmatrix} M_{1A} \\ N_{1A} \\ M_{1B} \\ N_{1B} \\ M_{2A} \\ N_{2A} \\ M_{2B} \\ ... \\ M_{nB} \\ N_{nB} \end{bmatrix} = \begin{bmatrix} S_1 + S_2 \\ 0 \\ 0 \\ 0 \\ 0 \\ 0 \\ 0 \\ ... \\ 0 \\ 0 \end{bmatrix} \tag{95}$$

By solving the above matrix equation, the acoustic wave equations in the periodic composite wave guiding layer are obtained. As a result, the transmitted wave equation through the phononic wave guiding layer can be calculated under a series of frequencies.

B. Transmission Line Model for Phononic-crystal Patterned Wave Guiding Layer

With the transmission of acoustic waves through a phononic crystal at frequencies within the band gap, the calculation of a one-dimensional arrangement is much simpler and can be done analytically [163]. Using boundary conditions (internal force and linear velocity) between different layers, transmission line model (TLM) can be described as Fig. 6, and the corresponding transfer matrix is given as follows:

$$\begin{bmatrix} F_1 \\ \upsilon_1 \end{bmatrix} = [B_1]\cdot[B_2]\cdot\ldots\cdot[B_{n-1}]\cdot[B_n]\cdot\begin{bmatrix} F_{n+1} \\ \upsilon_{n+1} \end{bmatrix}$$
$$\begin{bmatrix} F_n \\ \upsilon_n \end{bmatrix} = [B_n]\cdot\begin{bmatrix} F_{n+1} \\ \upsilon_{n+1} \end{bmatrix} = \begin{bmatrix} \cos\alpha_n^L & jZ_n^L \sin\alpha_n^L \\ j\sin\alpha_n^L / Z_n^L & \cos\alpha_n^L \end{bmatrix}\cdot\begin{bmatrix} F_{n+1} \\ \upsilon_{n+1} \end{bmatrix} \quad (54)$$

where

$$Z_n^L = A\sqrt{\rho_n c_n}$$
$$\alpha_n^L = \omega h_n \sqrt{\rho_n / c_n} \quad (55)$$

ρ_n, c_n are the density and elastic stiffness of loading layer, respectively, and h_n is the thickness. Defining $Z_i = F_i/v_i$ (i = 1, 2, …, n), with F_{n+1} = 0 as the free surface, the equivalent impedance after the nth period is as that

$$Z_n = jZ_n^L \tan(\alpha_n^L) = jZ_n^L \tan(\omega h_n \sqrt{\rho_n / c_n}) \quad (96)$$

In similarity, setting

$$Z_i^S = jZ_i^L \tan(\alpha_i^L) = jZ_i^L \tan(\omega h_i \sqrt{\rho_i / c_i}), i = 1, 2, ..., n \quad (97)$$

and the equivalent impedance after the ith period can be calculated through

$$Z_{i-1} = Z_{i-1}^{L\,2} \frac{Z_i + Z_{i-1}^S}{Z_{i-1}^{L\,2} + Z_i Z_{i-1}^S} = Z_{i-1}^L \frac{jZ_i^L \tan(\alpha_i^L) + jZ_{i-1}^L \tan(\alpha_{i-1}^L)}{Z_{i-1}^L - Z_i^L \tan(\alpha_i^L)\tan(\alpha_{i-1}^L)}, i = 2, ..., n-1, n \quad (98)$$

The calculations of TLM can lead to an effective acoustic impedance, Z_{eff} of the phononic wave guiding layer generated from all layers and the acoustic impedance at the outer port. Reflection and transmission coefficients R, T can be calculated replacing the phononic wave guiding layer by a virtual semi-infinite material with the acoustic impedance Z_{eff} [75]:

$$R = \frac{Z_2 - Z_{eff}}{Z_2 + Z_{eff}}, T = \frac{2Z_2}{Z_2 + Z_{eff}} \tag{99}$$

6.2.2 Numerical Results and Discussions

Based on the theoretical models of 1-dimensional phononic materials introduced in previous session, the corresponding numerical results are obtained for a parylene-C-based wave guiding layer. Related material properties are set in the calculation as well. From the acoustic wave propagation equations in a phononic wave guiding layer, the magnitude of transmitted waves can be obtained; and from the TLM, the effective acoustic impedance of phononic structure in the wave guiding layer is calculated. Through either way, the corresponding band gap of phononic wave guiding layer can be acquired. Taking the filling material of ZnO as an example, the band structure near the resonance frequency is calculated by the two models as shown in Fig. 33 and Fig. 34. Fig. 33 is the amplitude of transmitted waves through the parylene-C/ZnO phononic wave guiding layer. The period length is chosen as 11 μm and the period number is set to be 5, 10, 15 and 20 in order. Evident upper and lower cutoff frequencies can be seen from the transmitted wave amplitude curves, where the amplitude of transmitted waves turns to be zero sharply. For different period number, the upper and lower cutoff frequencies are relatively consistent as 119 *MHz* and 128 *MHz*, respectively. As the period number is increased, the number of amplitude peaks within the pass band (119 ~ 121 *MHz*) presents a linear increase accordingly.

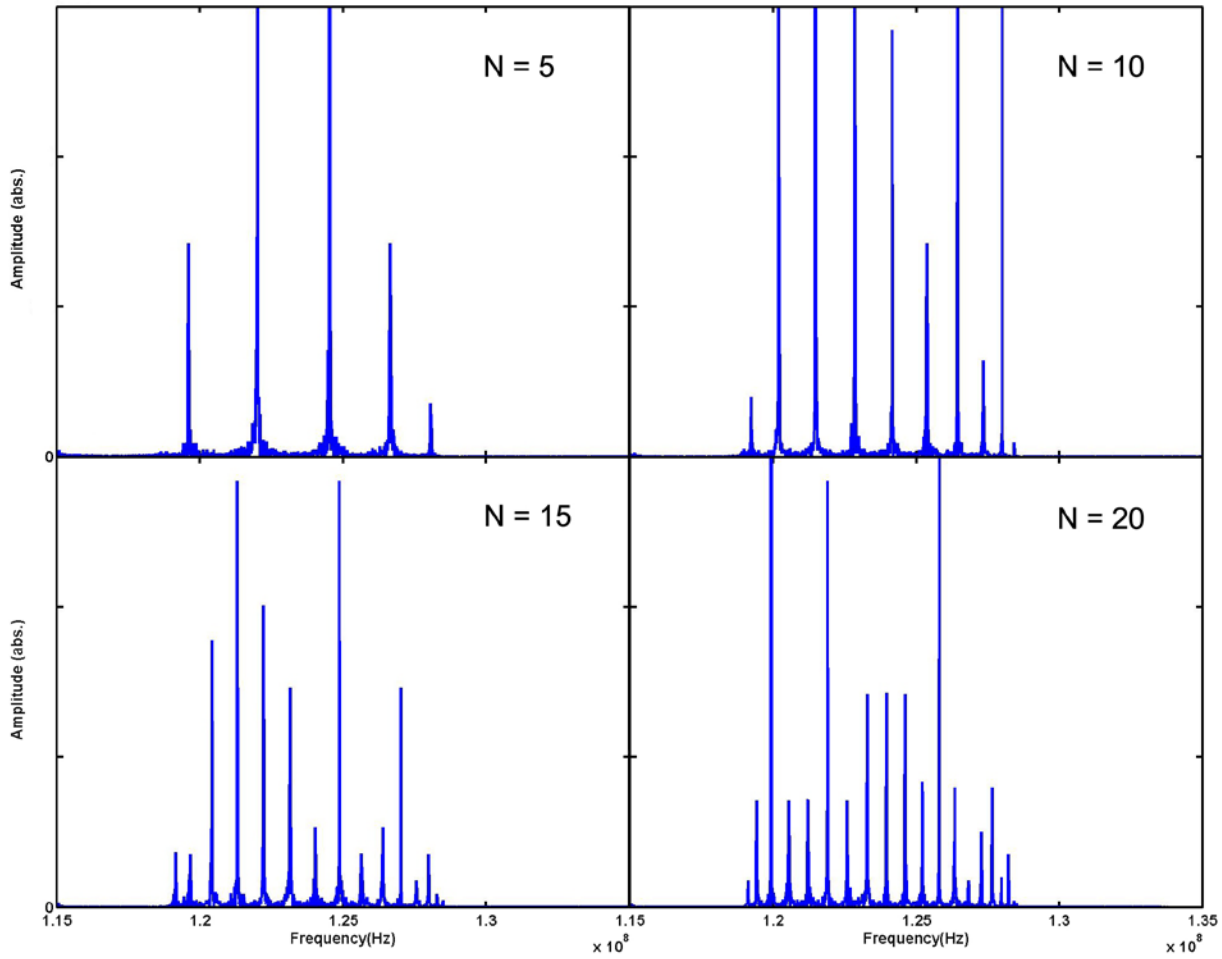

Figure 33. Amplitude of transmitted waves through parylene-C/ZnO phononic wave guiding layer

In the meantime, the effective acoustic impedance of the parylene-C/ZnO phononic wave guiding layer with different period number is shown in Fig. 34. In similarity, relatively stable cutoff frequencies can be acquired from the effective impedance curves. Fig. 35 illustrates the upper (red line) and lower (blue line) cutoff frequencies for the phononic patterns with varied period number of 5, 10, 15 and 20, which are extracted from Fig. 34. There is no significant difference among these cutoff values, leading to a relatively consistent pass band ranging from 119.2 *MHz* to 128.4 *MHz*. It can be found that the cutoff frequencies from the two models, the

acoustic wave propagation model and TLM, can reach good agreement with each other, proving the validity of theoretical calculation.

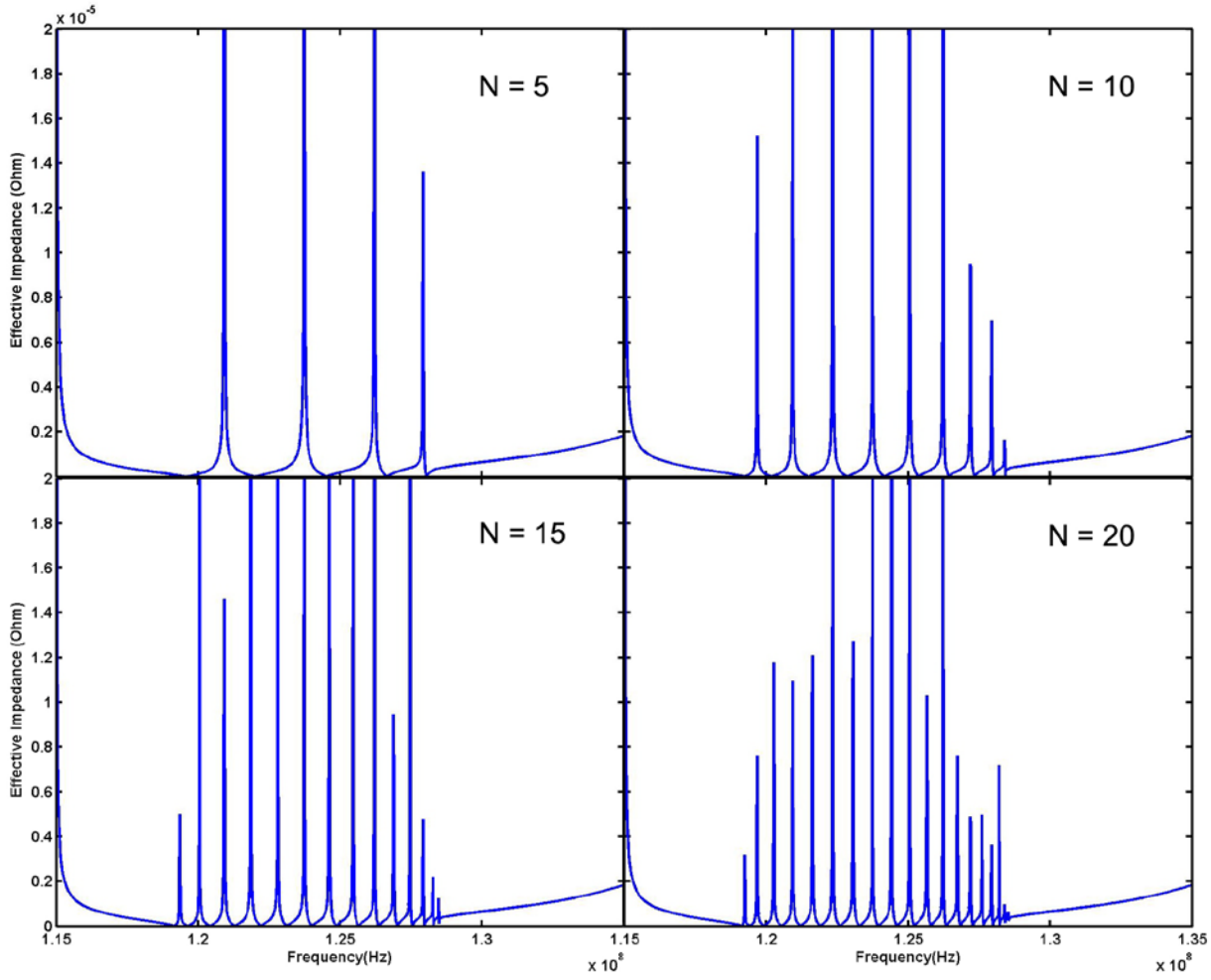

Figure 34. Effective impedance of parylene-C/ZnO phononic wave guiding layer

From the discussion above, it can be seen that along with the period number increases, there are no evident variations in the cutoff frequencies. Besides, the effect of period length on the stop band is analyzed for the parylene-C-based phononic wave guiding layer, and the period number of 10 is adopted as a typical example. Fig. 36 presents the upper and lower cutoff

frequencies of the parylene-C/ZnO and parylene-C/SiO_2 phononic wave guiding layers with varied period lengths. For both two types of wave guiding layers, the upper and lower cutoff frequencies are decreased with an increase in period length. As the period length increases, pass bands are shifted to the lower frequency ranges; however, the pass band width is relatively consistent. For the parylene-C/ZnO phononic structure, when the half period length ($h_A = h_B = d/2$) increases from 1.0 μm to 1.2 μm, the pass band is gradually shifted from 131.1 ~ 141.2 *MHz* to 110.1 ~ 117.3 *MHz*, with a slightly decreased band width from ~10.1 *MHz* to ~7.2 *MHz*. Similarly, with SiO_2 films as the filling material, the pass band is shifted to a lower frequency range along with an increase in the half period length, and the pass band width keeps stable around 10 *MHz*.

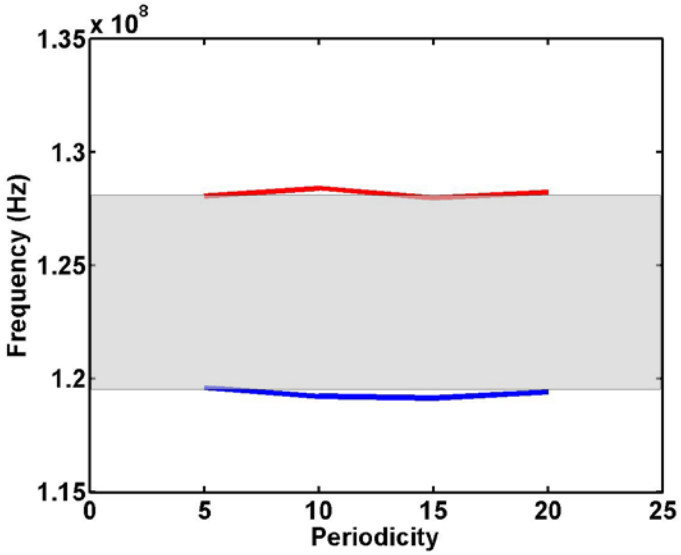

Figure 35. Band structure of parylene-C/ZnO phononic wave guiding layer with different period number

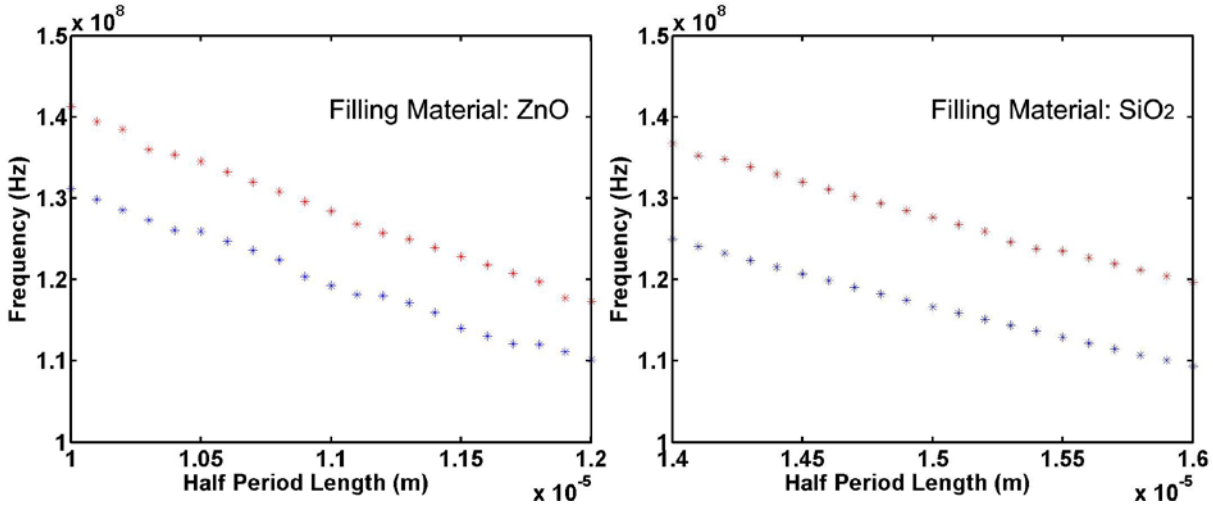

Figure 36. Band structure of phononic wave guiding layer with different period lengths

As discussed in Chapter 5, with parylene-C wave guiding layer of normalized thickness around 0.48, the Love wave sensor can obtain an optimization of a high coupling coefficient, a low propagation loss and a high mass sensitivity. With the wave length λ = 32 μm, the thickness of parylene-C films should be 1.5 ~ 1.6 μm. In this case, the propagation velocity is ~4000 *m/s*, and the corresponding resonance frequency is ~125 *MHz*. As a result, the target center frequency, which should deviate from the stop band, is 125 *MHz*. In order to obtain the optimal period length for both the filling materials ZnO and SiO_2, the relation between the period length and stop band is investigated as shown in Fig. 36. The numerical results indicate that for the filling material ZnO with a half period length $d/2$ = 11 μm or SiO_2 with 15 μm, the signals other than at the vicinity of operation frequency (120 ~ 125 *MHz*) would be stopped by the phononic structure in the wave guiding layer. By non-operation signal filtering, the sensitivity of Love wave sensor can be enhanced accordingly. In next session, FEM simulation in ANSYS is conducted to validate the noise signal filtering through the phononic wave guiding layer, where $h_A = h_B$ = 11 μm and $h_A = h_B$ = 15 μm are set respectively for ZnO and SiO_2.

6.3 PARAMETER OPTIMIZATION BY FINITE ELEMENT ANALYSIS

6.3.1 Theoretical Model and Analysis Methods

In order to prove the theoretical models introduced in previous sessions, the 3-dimensional (3D) finite element model is created in ANSYS to study the wave propagation characteristics as well as its frequency response. The transient response of a phononic wave guiding layer to a cosine input applied at one end of the layer is investigated. The model is developed for the phononic parylene-C-based wave guiding layer, which is $20\lambda \sim 30\lambda$ long (wave length $\lambda = 32\ \mu m$), $\lambda/8$ wide, and $\sim 0.048\lambda$ thick, with phononic structure starting from the left end ($x = 0$) with a periodicity of (period length) × (period number), as shown in Fig. 38. The optimal period length is depending on the theoretical calculation results in previous sessions: for different filling materials, the optimal period length is changed. Following the phononic structure, an extended paryelen-C film is added in order to absorb the transmitted waves through the phononic wave guiding layer. Hexahedron finite elements are used throughout the model with six degrees of freedom, especially the particle displacements in x, y, and z directions. In a Love wave sensor, the acoustic wave propagation in wave guiding layer varies with x_3 in the form of $\exp(\pm jk\beta x_3)$. In order to include this term effect, elements are formed to ensure highest density along the thickness direction of the wave guiding layer as shown in the inert of Fig. 37.

The numerical simulations are initiated with a cosine input signal applied at the left end of the wave guiding layer. As discussed above, when the parylene-C films is 1.6 μm, the propagation velocity is ~4000 *m/s*, and the corresponding resonance frequency is ~125 *MHz* with $\lambda = 32\ \mu m$. The time step is 1.0 *ns*, and the particle motion simulation is conducted for 300 *ns*.

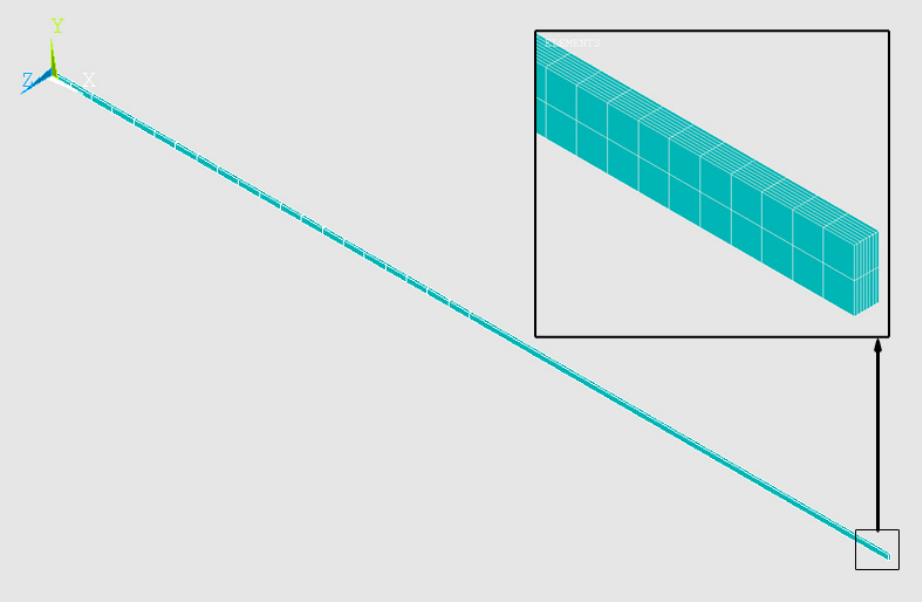

Figure 37. Schematic diagram of a phononic wave guiding layer with periodicity of 10 (the insert is the right end of meshed wave guiding layer)

6.3.2 Numerical Results and Discussions

Based on the FEM model presented in previous session, the corresponding numerical results are obtained. Assuming the filling material of ZnO with different period number 5, 10, 15 and 20, the amplitude of transmitted waves through the phononic wave guiding layer is shown in Fig. 38. For different period number, the acoustic vibration at a frequency of 125 *MHz* can be transmitted through the parylene-C/ZnO phononic structure successfully, which has good agreement with the TLM theoretical calculation above. The particle movement is enhanced gradually as the time is going on, when more vibration energy is transferred onto it. With an increase in period number, the time to obtain the target amplitude rises gradually. As a result, through the same time period,

the movement amplitude of parylene-C particles following the phononic structure at the end point is decreased accordingly.

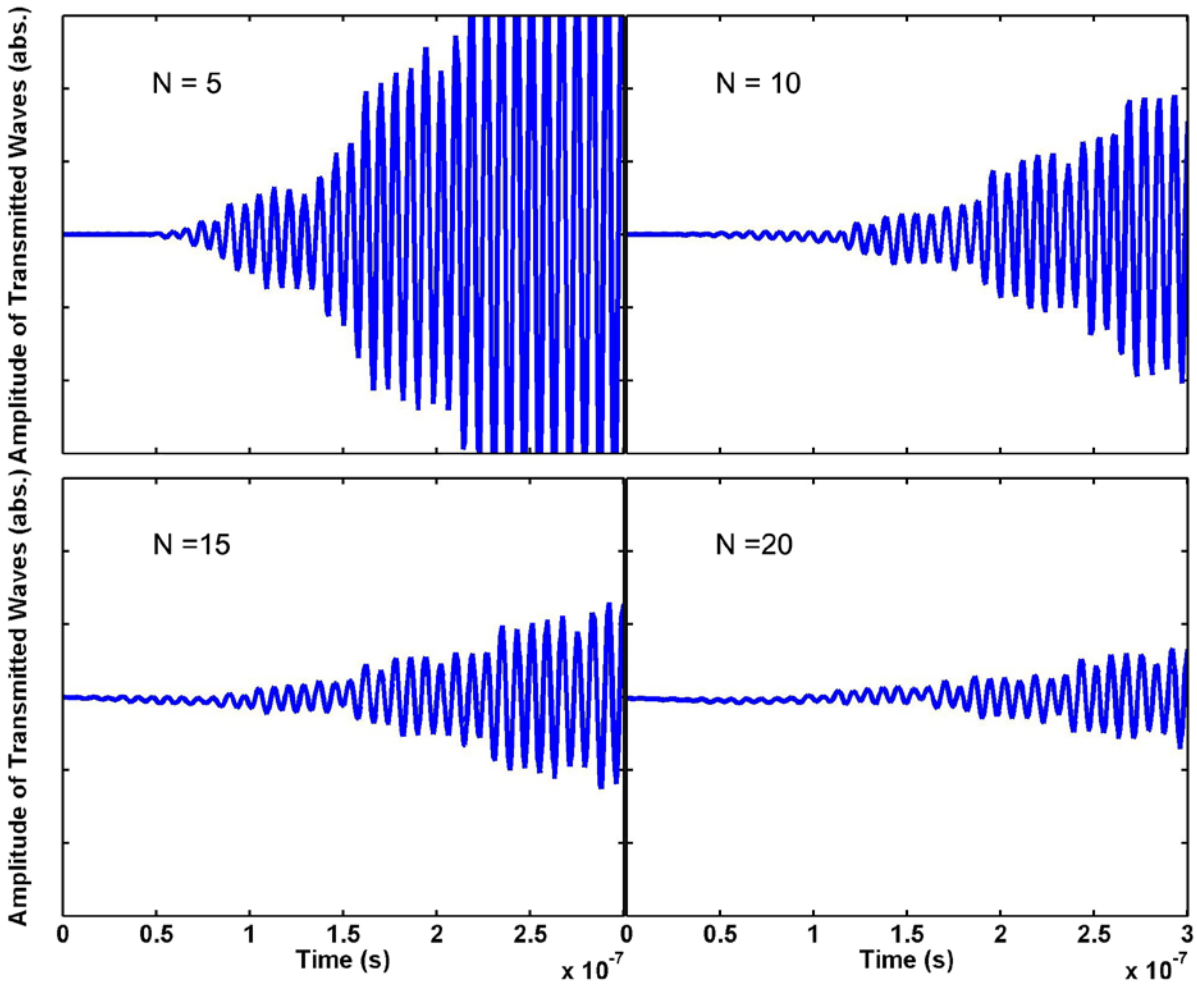

Figure 38. Amplitude of transmitted waves through parylene-C/ZnO phononic wave guiding layer with different periodicities

As indicated in Session 6.2.2, for the filling material of ZnO, the optimal period length is considered to be ~11 μm by the theoretical calculation. Thus, with 11 μm as the length of base and filling materials, the amplitude of transmitted waves at different excitation frequencies is

shown in Fig. 39. For a series of excitation frequencies, the particle movement following the phononic structure in the wave guiding layer presents different variation tendencies. When the excitation frequency is 120 or 125 *MHz*, the movement amplitude increases continuously; and after a certain time, the final vibration amplitude is significantly enhanced compared with the particle movement at other frequencies. It can be seen that when the excitation frequency is out of the pass band, there is no continuous increase tendency in the particle movement amplitude. Therefore, the transmitted waves at non-operation frequencies cannot propagate through the phononic structure successfully when the operation signals will keep the original characteristics through the entire phononic wave guiding layer. The numerical results from both the analytical method (acoustic wave propagation model and TLM) and FEM have good agreement with each other.

In addition, for the filling material of SiO_2, the optimal period length is chosen to be ~15 μm by the theoretical modeling. Fig. 40 presents the transmitted wave amplitude at a series of excitation frequencies for the parylene-C/SiO_2 phononic wave guiding layer with $h_A = h_B = 15$ μm. In similarity to the parylene-C/ZnO phononic wave guiding layer, when the acoustic waves are at a frequency of 120 or 122.5 *MHz*, the movement amplitude of particles can increase gradually, which means a continuous energy transferring through the phononic structure in the wave guiding layer; when the acoustic waves are at the frequency out of the specific pass band, the parylene-C particles following the phononic structure cannot achieve a considerable vibration amplitude but limited within a relatively small range. It is proven again that with the phononic structure in the wave guiding layer, acoustic waves at certain frequencies will be stopped, which provides an advisable way for non-operation frequency signal filtering and increase the Love wave sensor sensitivity accordingly.

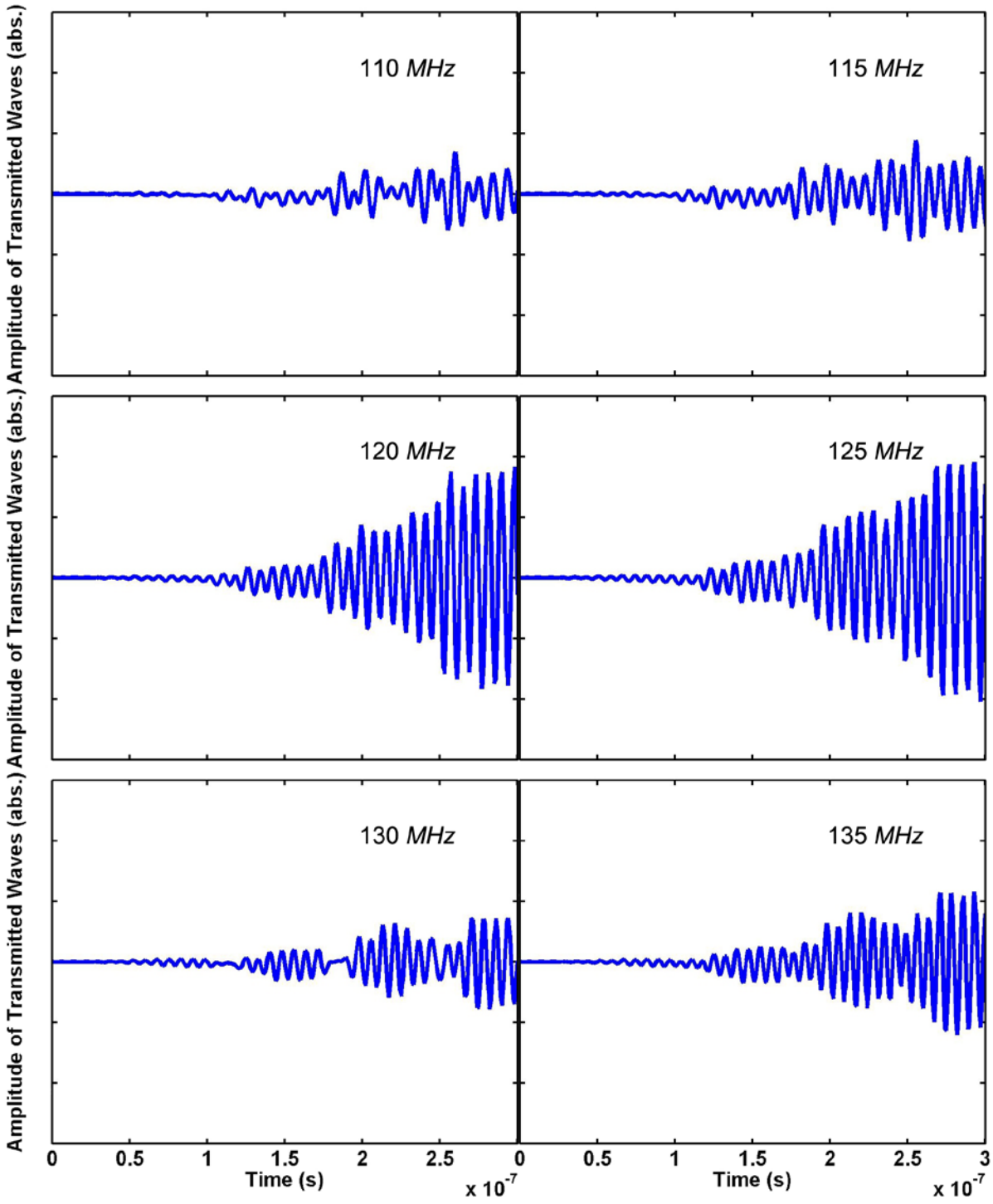

Figure 39. Amplitude of transmitted waves through parylene-C/ZnO phononic wave guiding layer under different frequencies

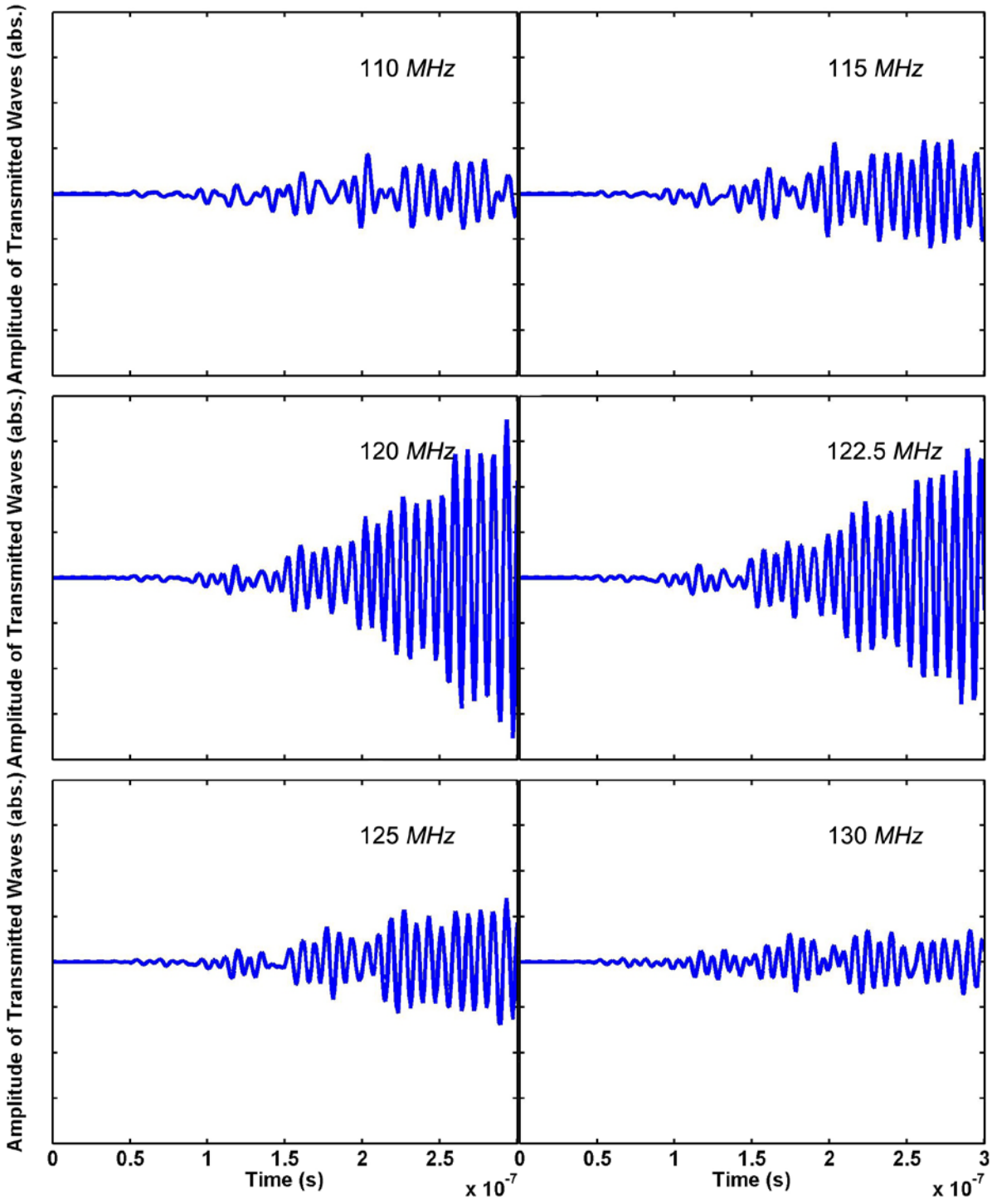

Figure 40. Amplitude of transmitted waves through parylene-C/SiO_2 phononic wave guiding layer under different frequencies

6.4 CONCLUSIONS

In this chapter, a Love mode SAW sensor with phononic parylene-C wave guiding layer is proposed, where arrays of filling materials (ZnO or SiO_2 films) are fabricated on the surface of parylene-C films. For different filling materials with various density and elasticity, the effects of related structural design parameters (period length and period number of phononic structure) on the stop band of Love wave sensor are investigated. As the period number is varied, there is no obvious change in the cutoff frequencies; however, along with the period length increases, both the upper and lower cutoff frequencies are shifted to lower frequency points, and the pass band width is relatively consistent. The numerical results indicate that for filling material ZnO with a periodicity of 11 μm or SiO_2 with 15 μm, only the signals at the vicinity of operation frequency of Love wave sensor can go through the sensing area, when others are stopped by the phononic structure, which could enhance the sensor sensitivity accordingly. The numerical results from both analytical calculation (acoustic wave propagation model and TLM) and FEM reach good agreement, indicating a potential design with high sensitivity and reliability for a cell-based Love wave biosensor.

7.0 CONCLUDING REMARKS

As a multidisplinary project of mechanical engineering and cell mechano-biology, this research focuses on the acoustic wave sensors for biomechanical and biological characterization of cells. Based on different piezoelectric single crystals, the acoustic wave sensors are applied as the cell-based biosensors, to investigate the cell behaviors in varied physiological processes, in form of resonators or passive devices. Two types of acoustic wave sensors are studied in-depth, the TSM resonator and Love wave sensor. The future research work will focus on the novel biosensor design, fabrication and implementation, signal processing, stability control, selectivity and sensitivity improvement. Sensor design can be integrated with additive manufacturing techniques, for the establishment of an effective and robust biosensor system.

7.1 RESEARCH SUMMERY

Acoustic wave sensors have been used extensively for semi-quantitative and quantitative measurements due to their non-invasive, real-time, long-time stable and easy connectable features. In this research, two kinds of acoustic wave sensors, the TSM resonator and the Love mode SAW sensor are studied in depth as cell-based biosensors. As the most widely used acoustic wave sensor, the quartz TSM resonator is applied to characterize viscoelastic properties of TSCs and platelets. An explicit relation is established between the structural and mechanical

properties of cells (complex shear modulus $G' + jG''$ & average thickness h) and the electrical response of TSM resonator, thus providing useful quantitative measures on cell states. Compared with TSM resonator, the Love wave sensor was reported to perform extreme sensitivity to certain surface perturbations within the relatively short distance of ~50 *nm* from the surface. A 36˚ *YX*-$LiTaO_3$ based Love wave sensor with a parylene-C wave guiding layer is adopted as a cell-based biosensor. A theoretical model is proposed to describe the Love wave propagation in the wave guiding layer and adherent cell layer, and penetration into the liquid medium. Based on this model, the sensor response to the adhesion process of cells are obtained, indicating that the adherent cell layer of varied shear modulus can induce characteristic variations in propagation velocity v and propagation loss *PL*. In addition, a Love wave sensor with a phononic wave guiding layer is introduced. The numerical results from both analytical solution and FEM show that with specific combination of the structural design parameters (period length and period number) and filling material's properties (density and elasticity), the acoustic wave propagation in vicinity of working frequency can be stopped by the phononic patterns, and the sensitivity of Love wave sensor is increased accordingly. Both two kinds of acoustic wave sensors present their potential as the cell-based biosensors, indicating advisable techniques for investigating cell biology in general and certain physiological processes in particular. The primary contributions of this dissertation are listed as follows:

(1) An extension application of TSM resonator is proposed to characterize the viscoelastic properties of cells. An overall increase in both stiffness and viscosity is observed by TSM resonator during aging process of tendon stem/progenitor cells, which could be associated with the dense cytoskeleton organization. In addition, changes in viscoelasticity and average thickness of platelets monitored by TSM resonator provide useful quantitative measures on platelet states

during activation process. By structural and mechanical properties characterization, the corresponding states of cells in a certain physiological process can be investigated from the response of TSM resonators.

(2) An explicit relation between the cell states and electrical response of TSM resonator is established through the viscoelasticity characterization. Compared with previous research using the TSM resonator as a cell-based biosensor, the TSM resonator in this dissertation is indicated as an advisable and reliable tool to extract mechanical properties of cells as a biophysical marker.

(3) Theoretical expression for the decay length of Love wave penetration into the liquid medium is obtained, proving a significantly decreased sensitive distance compared with TSM resonator. Based on theoretical calculation, the decay length δ for the Love wave penetration into water is given in order of ~50 *nm*, which presents high consistency with experimental observations.

(4) A comprehensive evaluation method is proposed to obtain the optimal wave guiding layer thickness for a Love wave biosensor based on theoretical analysis and calculation. For a good combination of a high electromechanical coupling coefficient, a low propagation loss and a high mass sensitivity, it is suggested that the optimal wave guiding layer thickness in a 36º *YX*-$LiTaO_3$-based Love wave sensor is at the vicinity of h/λ = ~0.05 in vacuum, and ~0.048 in liquid (water).

(5) The response of Love wave biosensor to the adhesion process of cells is obtained based on theoretical analysis. The numerical results indicate that the adherent cells of various storage or loss shear modulus in certain range can induce evident, characteristic variations in propagation velocity υ and propagation loss *PL* of Love wave sensors. In comparison, the thickness and viscosity of parylene-C wave guiding layer have limited influence in the changes of υ and *PL*. Compared with the TSM resonator, the trigger of Love wave sensor response is primarily

induced by the initial interaction between the cells and substrate in the early stage of adherent cell layer formation .

(6) Based on theoretical simulation, a Love wave sensor with a phononic wave guiding layer is introduced for non-operation signal filtering and sensor sensitivity improvement. The numerical results indicate that for filling material ZnO with a periodicity of 11 μm or SiO_2 with 15 μm, only the signals at the vicinity of operation frequency can go through the sensing area, when others are stopped by the phononic structure, which could enhance the sensitivity of Love wave sensor accordingly.

7.2 FUTURE RESEARCH

The future research work will focus on novel biosensor design, fabrication and implementation, signal processing, stability control, selectivity and sensitivity improvement. Acoustic wave sensors have been used extensively for semi-quantitative and quantitative measurements. In addition to their general applications such as microbalance for mass sensing, acoustic wave sensors can be used in some innovative conditions as well, for example, cell-based biosensors. In this dissertation, a 36° *YX*-$LiTaO_3$ based Love wave sensor with a parylene-C wave guiding layer is studied in-depth theoretically, including its response as a cell-based biosensor to the adhesion process of cells and sensitivity improvement with a phononic guiding layer. In the future, both theoretical analysis and experimental measurement need be conducted for design and test of novel acoustic wave sensors. Through in-depth theoretical analysis and signal processing, useful information regarding the object's states can be extracted from the raw data of sensor system. In the meantime, reliable theoretical analysis can provide a solid platform for new features in

sensors. Furthermore, integration of different types of sensors is a possible way to achieve multiple quantitative measure sensing, for example, a combination of the acoustic wave sensor system and an electric impedance sensor system. An appropriate theoretical model and multiple-quantitative-measure criteria can be developed for applications in a series of relevant fields:

(1) Biological & Biomedical Applications. Acoustic wave sensors were applied for polymer characterization in previous studies. The real-time monitoring of material properties has a wide application on the material processing control, structure health monitoring, etc. Besides the traditional materials, acoustic wave sensors can also be used to analyze the soft biological materials, for example cells. The bulk or surface acoustic wave propagation is changed due to the thickness, density, modulus or the microstructure of object materials. Based on material characterization, a quantitative detection can be achieved on the physiological responses of cells or tissues under the biophysical and biochemical microconditions. In the meantime, the acoustic wave sensors can also be applied in toxicity testing and drug screening. Detection of nuclear, biological and chemical agents has extreme high demands not limited in environmental monitoring, but also in food industry and anti-bioterrorism practice. The cell group acts as a robust functional reporter of toxicity since it is very sensitive, even to a low amount of biological and chemical agents. By monitoring the response of cell behaviors in certain environments, the cell-based sensor system will have the capabilities of fast, easy and simultaneous measurements of a large number of possible contaminations or hazards, especially those unanticipated ones.

(2) Applications in Harsh Environments. Another acoustic wave sensor-related area is sensor technology for high-temperature and harsh environments. Currently, there is a continuing need for the development of fast, sensitive, rugged, reliable, and low-cost sensors for applications in harsh industrial environments found in metal processing and casting, automotive, aerospace and

aeronautics, energy and power industries. In response to this need, novel acoustic sensor systems that can be used in these extreme environments should be developed. A series of high-temperature piezoelectric single crystals were studied in previous studis. Strong candidates for the high-temperature piezoelectric applications include some non-traditional, newly-developed piezoelectric crystals, such as aluminum nitride (AlN), $YCa_4O(BO_3)_3$ (YCOB) and langasite family. Through theoretical modeling and experimental measuring, appropriate piezoelectric substrates can be adopted for acoustic wave sensors in high-temperature and harsh environmental applications. And wireless and passive surface acoustic wave sensors will be developed for various applications (gas, strain, and temperature sensors) in harsh environments in the future research.

Recently, there is an increasing interest in additive manufacturing that is able to accomplish some specific 3-dimensional (3D) structures, which otherwise cannot be realized through traditional manufacture techniques. Especially, 3D printing makes the fabrication of biochips with complex structures come true, which could meet those special needs required by living cells. The 3D-printed biochips with surface treatment can be assembled in the corresponding sensor system, like an acoustic wave sensor system, thus investigating some complicated cellular activities. Micro/nanofabrication technology allows the miniaturization of sensors, and the microfluidics gives rise to the powerful techniques in controlling and measuring biological processes on the micro- & nano-scale. The lab-on-a-chip sensors can be developed for automated and fast sensing applications. Through sensor systems with 3D biochips, in-depth detection of the complicated physiological processes is possible, which is of great benefits for a variety of research and applications in practice.

BIBLIOGRAPHY

[1] Ballantine, D.S., et al., *Acoustic Wave Sensor: Theory, Design, and Physico-Chemical Applications*. 1997: Academic Press.

[2] Collings, A.F. and F. Caruso, Biosensors: Recent Advances. *Reports on Progress in Physics*, 1997. 60: p. 1397-1445.

[3] Amano, Y. and Q. Cheng, Detection of Influenza Virus: Traditional Approaches and Development of Biosensors. *Analytical and Bioanalytical Chemistry*, 2005. 381: p. 156-164.

[4] Wang, P. and Q. Liu, *Cell-Based Biosensors: Principles and Applications*. 2010: Artech House.

[5] Hardin, J., G. Bertoni, and L.J. Kleinsmith, *Becker's World of the Cell*. 2012: Pearson Education.

[6] Suresh, S., Biomechanics and Biophysics of Cancer Cells. *Acta Biomaterialia*, 2007. 3: p. 413-438.

[7] Alcaraz, J., et al., Microrheology of Human Lung Epithelial Cells Measured by Atomic Force Microscopy. *Biophysical Journal*, 2003. 84(3): p. 2071-2079.

[8] Mahaffy, R.E., et al., Quantitative Analysis of the Viscoelastic Properties of Thin Regions of Fibroblasts Using Atomic Force Microscopy. *Biophysical Journal*, 2004. 86(3): p. 1777-1793.

[9] Smith, B.A., et al., Probing the Viscoelastic Behavior of Cultured Airway Smooth Muscle Cells with Atomic Force Microscopy: Stiffening Induced by Contractile Agonist. *Biophysical Journal*, 2005. 88(4): p. 2994-3007.

[10] Kuznetsova, T.G., et al., Atomic Force Misroscopy Probing of Cell Elasticity. *Micron*, 2007. 38: p. 824-833.

[11] Thoumine, O. and A. Ott, Time Scale Dependent Viscoelastic and Contractile Regimes in Fibroblasts Probed by Microplate Manipulation. *Journal of Cell Science*, 1997. 110: p. 2109-2116.

[12] Beil, M., et al., Sphingosylphosphorylcholine Regulates Keratin Network Architecture and Visco-elastic Properties of Human Cancer Cells. *Nature Cell Biology*, 2003. 5(9): p. 803-811.

[13] Fernández, P., P.A. Pullarkat, and A. Ott, A Master Relation Defines the Nonlinear Viscoelasticity of Single Fibroblasts. *Biophysical Journal*, 2006. 90(10): p. 3796-3805.

[14] Khurana, S., et al., Monitoring Platelet Glycoprotein IIbIIIa-Fibrin Interaction with Tissue Factor-Activated Thromboelastography. *Journal of Laboratory and Clinical Medicine*, 1997. 130(4): p. 401-411.

[15] Shore-Lesserson, L., et al., Thromboelastography-Guided Transfusion Algorithm Reduces Transfusions in Complex Cardiac Surgery. *Cardiovasular Anesthesia*, 1999. 98: p. 312-319.

[16] Michelson, A.D., Methods for the Measurement of Platelet Function. *American Journal of Cardiology*, 2009. 103(3): p. 20A-26A.

[17] Bausch, A.R., et al., Local Measurements of Viscoelastic Parameters of Adherent Cell Surfaces by Magnetic Bead Microrheometry. *Biophysical Journal*, 1998. 75(4): p. 2038-2049.

[18] Bausch, A.R., W. Moller, and E. Sackmann, Measurement of Local Viscoelasticity and Forces in Living Cells by Magnetic Tweezers. *Biophysical Journal*, 1999. 76: p. 573-579.

[19] Fabry, B., et al., Scaling the Microrheology of Living Cells. *Physical Review Letters*, 2001. 87(14): p. 148102-1-4.

[20] Li, J., et al., Monitoring of Integrin-Mediated Adhesion of Human Ovarian Cancer Cells to Model Protein Surfaces by Quartz Crystal Resonators: Evaluation in the Impedance Analysis Mode. *Biosensors and Bioelectronics*, 2005. 20: p. 1333-1340.

[21] Marx, K.A., et al., Quartz Crystal Microbalance Biosensor Study of Endothelial Cells and their Extracellular Matrix Following Cell Removal: Evidence for Transient cellular Stress and Viscoelastic Changes during Detachment and the Elastic Behavior of the Pure Matrix. *Analytical Biochemistry*, 2005. 343: p. 23-34.

[22] Li, F., J.H.-C. Wang, and Q.-M. Wang, Monitoring Cell Adhesion by Using Thickness Shear Mode Acoustic Wave Sensors. *Biosensors and Bioelectronics*, 2007. 23: p. 42-50.

[23] Tan, L., et al., Dynamic Measurement of the Surface Stress Induced by the Attachment and Growth of Cells on Au Electrode with a Quartz Crystal Microbalance. *Biosensors and Bioelectronics*, 2009. 24: p. 1603-1609.

[24] Wegener, J., A. Janshoff, and H.-J. Galla, Cell Adhesion Monitoring Using a Quartz Crystal Microbalance: Comparative Analysis of Different Mammalian Cell Lines. *European Biophys Journal*, 1998. 28: p. 26-37.

[25] Wegener, J., et al., Analysis of the Composite Response of Shear Wave Resonators to the Attachment of Mammalian Cells. *Biophysical Journal*, 2000. 78: p. 2821-2833.

[26] Reyes, P.I., et al., ZnO Nanostructure-Modified QCM for Dynamic Monitoring of Cell Adhesion and Proliferation. *Biosensors and Bioelectronics*, 2013. 41: p. 84-89.

[27] Hook, F., et al., The Dissipative QCM-D Technique: Interfacial Phenomena and Sensor Applications for Sensors Biomembranes Living Cells and Polymers. *IEEE International Frequency Control Symposium Proceedings*, 1999: p. 966-972.

[28] Andersson, M., et al., Quartz Crystal Microbalance with Dissipation Monitoring (QCM-D) for Real Time Measurements of Blood Coagulation Density and Immune Complement Activation on Artificial Surfaces. *Biosensors and Bioelectronics*, 2005. 21: p. 79-86.

[29] Lord, M.S., et al., Monitoring Cell Adhesion on Tantalum and Oxidized Polystyrene Using a Quartz Crystal Microbalance with Dissipation. *Biomaterials*, 2006. 27: p. 4529-4537.

[30] Fatisson, J., F. Azari, and N. Tufenkji, Real-Time QCM-D Monitoring of Cellular Responses to Different Cytomorphic Agents. *Biosensors and Bioelectronics*, 2011. 26: p. 3207-3212.

[31] Lucklum, R., et al., Determination of Complex Shear Modulus with Thickness Shear Mode Resonators. *Journal of Physics D: Applied Physics*, 1997. 30: p. 346-356.

[32] Lucklum, R. and P. Hauptmann, Transduction Mechanism of Acoustic-Wave Based Chemical and Biochemical Sensors. *Measurement Science and Technology*, 2003. 14: p. 1854-1864.

[33] Hossenlopp, J., et al., Characterization of Epoxy Resin (SU-8) Film Using Thickness-Shear Mode (TSM) Resonator under Various Conditions. *Journal of Polymer Science B: Polymer Physics*, 2004. 42: p. 2373-2384.

[34] Jimenez, Y., et al., A Contribution to Solve the Problem of Coating Properties Extraction in Quartz Crystal Microbalance Applications. *IEEE Transactions on Ultrasonics, Ferroelectrics, and Frequency Control*, 2006. 53: p. 1057-1072.

[35] Herrmann, F., et al., Microacoustic Sensors for Liquid Monitoring. *Sensors Update*, 2001. 9(1): p. 105-160.

[36] Saitakis, M., A. Tsortos, and E. Gizeli, Probing the Interaction of a Membrane Receptor with a Surface-Attached Ligand using Whole Cells on Acoustic Biosensors. *Biosensors and Bioelectronics*, 2010. 25: p. 1688-1693.

[37] Moll, N., et al., A Love Wave Immunosensor for Whole E. coli Bacteria Detection Using an Innovative Two-Step Immobilisation Approach. *Biosensors and Bioelectronics*, 2007. 22(9–10): p. 2145-2150.

[38] Bisoffi, M., et al., Detection of Viral Bioagents Using a Shear Horizontal Surface Acoustic Wave Biosensor. *Biosensors and Bioelectronics*, 2008. 23(9): p. 1397-1403.

[39] Kalantar-Zadeh, K., et al., Novel Love Mode Surface Acoustic Wave Based Immunosensors. *Sensors and Actuators B*, 2003. 91(1–3): p. 143-147.

[40] Tamarin, O., et al., Real Time Device for Biosensing: Design of a Bacteriophage Model Using Love Acoustic Waves. *Biosensors and Bioelectronics*, 2003. 18(5–6): p. 755-763.

[41] Gaso, M.I.R., et al., Love Wave Biosensors: A Review, in *State of the Art in Biosensors - General Aspects*. 2013: InTech.

[42] White, R.M., Surface Elastic Waves. *Proceedings of the IEEE*, 1970. 58(8): p. 1238-1276.

[43] Gizeli, E., Design Considerations for the Acoustic Waveguide Biosensor. *Smart Materials and Structures*, 1997. 6: p. 700-706.

[44] Bender, F., R.W. Cernosek, and F. Josse, Love-Wave Biosensors Using Cross-Linked Polymer Waveguides on $LiTaO_3$. *Electronics Letters*, 2000. 36(19): p. 1672-1673.

[45] Harding, G.L., et al., Love Wave Acoustic Immunosensor Operating in Liquid. *Sensors and Actuators A*, 1997. 61(1–3): p. 279-286.

[46] Wang, Y., et al., Love Wave Hydrogen Sensors Based on ZnO Nanorod Film 36YX-$LiTaO_3$ Substrate Structures Operated at Room Temperature. *Sensors and Actuators B*, 2011. 158: p. 97-103.

[47] Branch, D.W. and S.M. Brozik, Low-Level Detection of a Bacillus Anthracis Simulant Using Love-Wave Biosensors on 36°YX $LiTaO_3$. *Biosensors and Bioelectronics*, 2004. 19(8): p. 849-959.

[48] Gizeli, E., et al., Sensitivity of the Acoustic Waveguide Biosensor to Protein Binding as a Function of the Waveguide Properties. *Biosensors and Bioelectronics*, 2003. 18: p. 1399-1406.

[49] Matatagui, D., et al., Array of Love-Wave Sensors Based on Quartz/Novolac to Detect CWA Simulants. *Talanta*, 2011. 85: p. 1442-1447.

[50] Lange, K., S. Grimm, and M. Rapp, Chemical Modification of Parylene C Coatings for SAW Biosensors. *Sensors and Actuators B*, 2007. 125: p. 441-446.

[51] Chang, T.Y., et al., Cell and Protein Compatibility of Parylene-C. *Langmuir*, 2007. 23: p. 11718-11725.

[52] Atashbar, M.Z., et al., 3D FE Simulation of H2 SAW Gas Sensor. *Sensors and Actuators B*, 2005. 111-112: p. 213-218.

[53] Cular, S., S.K.R.S. Sankaranarayanan, and V.R. Bhethanabotla, Enhancing Effects of Microcavities on Shear-Horizontal Surface Acoustic Wave Sensors: A Finite Element Simulation Study. *Applied Physics Letters*, 2008. 92: p. 244104-1-3.

[54] Liu, J. and S. He, Theoretical Analysis on Love Waves in a Layered Structure with a Piezoelectric Substate and Multiple Elastic Layers. *Journal of Applied Physics*, 2010. 107: p. 073511-1-8.

[55] Liu, J., et al., Properties of Love Waves in a Piezoelectric Layered Structure with a Viscoelastic Guiding Layer. *Smart Materials and Structures*, 2013. 22: p. 125034-1-8.

[56] Cook, R.K. and P.G. Weissler, Piezoelectric Constants of Alpha- and Beta-Quartz at Various Temperatures. *Physical Review*, 1950. 80(4): p. 712-717.

[57] Salt, D., *Hy-Q Handbook of Quartz Crystal Devices*. 1987: Van Nostrand Reinhold (UK).

[58] Mason, W.P., *Piezoelectric Crystals and Their Application to Ultrasonics*. 1950: D. Van Nostrand Company.

[59] Danoyan, Z.N. and G.T. Piliposian, Surface Electro-Elastic Love Waves in a Layered Structure with Piezoelectric Substrate and a Dielectric Layer. *International Journal of Solids and Structures*, 2007. 44: p. 5829-5847.

[60] Smith, R.T. and F.S. Welsh, Temperature Dependence of the Elastic, Piezoelectric, and Dielectric Constants of Lithium Tantalate and Lithium Niobate. *Journal of Applied Physics*, 1971. 42: p. 2219-2230.

[61] Nakamura, K., M. Kazumi, and H. Shimizu, SH-Type and Rayleigh-Type Surface Waves on Rotated Y-Cut $LiTaO_3$. *Ultrasonics Symposium Proceedings*, 1977: p. 819-822.

[62] Dyke, K.S.V., The Piezo-Electric Resonator and Its Equivalent Network. *Proceedings of the Institute of Radio Engineers*, 1928. 16: p. 742-764.

[63] Mason, W.P., *Electromechanical Transducers and Wave Filters*. 1948: D. Van Nostrand Company.

[64] Uchino, K., *Ferroelectric Devices*. 2000: Marcel Dekker.

[65] Jakoby, B. and M.J. Vellekoop, Properties of Love Waves: Applications in Sensors. *Smart Materials and Structures*, 1997. 6: p. 668-679.

[66] Lange, K., B.E. Rapp, and M. Rapp, Surface Acoustic Wave Biosensors: A Review. *Analytical and Bioanalytical Chemistry*, 2008. 391: p. 1509-1519.

[67] Rocha-Gaso, M.-I., et al., Surface Generated Acoustic Wave Biosensors for the Detection of Pathogens: A Review. *Sensors*, 2009. 9: p. 5740-5769.

[68] Campbell, J.J. and W.R. Jones, A Method for Estimating Optimal Crystal Cuts and Propagation Directions for Excitation of Piezoelectric Surface Waves. *IEEE Transactions on Sonics and Ultrasonics*, 1968. SU-15(4): p. 209-217.

[69] Takayanagi, A., K. Yamanouchi, and K. Shibayama, Piezoelectric Leaky Surface Wave in $LiNbO_3$. *Applied Physics Letters*, 1970. 17(5): p. 225-227.

[70] Drafts, B., Acoustic Wave Technology Sensors. *IEEE Transactions on Microwave Theory and Techniques*, 2001. 49(4): p. 795-802.

[71] Andle, J.C. and J.F. Vetelino, Acoustic Wave Biosensors. *Sensors and Actuators A*, 1994. 44: p. 167-176.

[72] Vives, A.A., *Piezoelectric Transducers and Applications*. 2008: Springer-Verlag Berlin Heidelberg.

[73] Janshoff, A. and C. Steinem, Piezoelectric Sensors. *Springer Series on Chemical Sensors and Biosensors*, ed. O. S.Wolfbeis. Vol. 5. 2007: Springer-Verlag Berlin Heidelberg.

[74] Bandey, H.L., et al., Modeling the Response of Thickness-Shear Mode Resonators under Various Loading Conditions. *Analytical Chemistry*, 1999. 71(11): p. 2205-2214.

[75] Auld, B.A., *Acoustic Fields and Waves in Solids*. 1973: John Wiley and Sons.

[76] Kovacs, G. and A. Venema, Theoretical Comparison of Sensitivities of Acoustic Shear Wave Modes for (Bio)chemical Sensing in Liquids. *Applied Physics Letters*, 1992. 61(6): p. 639-641.

[77] Kino, G.S., *Acoustic Waves: Devices, Imaging, and Analog Signal Processing*. 2000: Englewood Cliffs: Prentice-Hall.

[78] Cady, W.G., *Piezoelectricity: An Introduction to the Theory and Applications of Electromechanical Phenomena in Crystals*. 1964: New York: Dover.

[79] Qin, L., et al., Characterization of Polymer Nanocomposite Films Using Quartz Thickness Shear Mode (TSM) Acoustic Wave Sensor. *Sensors and Actuators A*, 2007. 136: p. 111-117.

[80] Kovacs, G., et al., A Love Wave Sensor for BioChemical Sensing in Liquids. S*ensors and Actuators A*, 1994. 43: p. 38-43.

[81] Yamanouchi, K. and K. Shibayama, Propagation and Amplification of Rayleigh Waves and Piezoelectric Leaky Surface Waves in $LiNbO_3$. *Journal of Applied Physics*, 1972. 43: p. 856-862.

[82] Ginsberg, M.H., X. Du, and E.F. Plow, Inside-out Integrin Signalling. *Current Opinion in Cell Biology*, 1992. 4: p. 766-771.

[83] Murphy-Ullrich, J.E., The De-adhesive Activity of Matricellular Proteins: Is Intermediate Cell Adhesion an Adaptive State? *The Journal of Clinical Investigation*, 2001. 107(7): p. 785-790.

[84] Lui, P.P.Y. and K.M. Chan, Tendon-Derived Stem Cells (TDSCs): From Basic Science to Potential Roles in tendon Pathology and Tissue Engineering Applications. *Stem Cell Reviews and Reports*, 2011. 7: p. 883-897.

[85] Lui, P.P.Y., Identity of Tendon Stem Cells: How Much do We Know? *Journal of Cellular and Molecular Medicine*, 2013. 17(1): p. 55-64.

[86] Zhang, J. and J.H.-C. Wang, Characterization of Differential Properties of Rabbit Tendon Stem Cells and Tenocytes. *BMC Musculosskeletal Disorder*, 2010. 11: p. 10-20.

[87] Zhang, J., et al., Differential Properties of Human ACL and MCL Stem Cells May be Responsible for Their Differential Healing Capacity. *BMC Musculosskeletal Disorder*, 2011. 9: p. 68-1-14.

[88] Butler, D.L., et al., Functional Tissue Engineering for Tendon Repair: A Multidisciplinary Strategy Using Mesenchymal Stem Cells Bioscaffolds and Mechanical Stimulation. *Journal of Orthopaedic Research*, 2008. 26(1): p. 1-9.

[89] Altman, G., et al., Cell Differentiation by Mechanical Stress. *FASEB Journal*, 2002. 16(2): p. 270-272.

[90] Zhang, J. and J.H.-C. Wang, Mechanobiological Response of Tendon Stem Cells: Implications of Tendon Homestasis and Pathogenesis of Tendinopathy. *Journal of Orthopaedic Research*, 2010. 28(5): p. 639-643.

[91] Rui, Y.F., et al., Mechanical Loading Increased BMP-2 Expression Which Promoted Osteogenic Differentiation of Tendon-Derived Stem Cells. *Journal of Orthopaedic Research*, 2011. 29(3): p. 390-396.

[92] Tuite, D.J., P.A.F.H. Renstrom, and M. O'Brien, The Aging Tendon. *Scandinavian Journal of Medicine and Science in Sports*, 1996. 7: p. 72-77.

[93] Zhou, Z., et al., Tendon-Derived Stem Progenitor Cell Aging Defective Self-Renewal and Altered Fate. *Aging Cell*, 2010. 9: p. 911-915.

[94] Li, Q.S., et al., AFM Indentation Study of Breast Cancer Cells. *Biochemical and Biophysical Research Communications*, 2008. 374: p. 609-613.

[95] Srivastava, A. and G. Krishnamoorthy, Cell Type and Spatial Location Dependence of Cytoplasmic Viscosity Measured by Time-Resolved Fluorescence Microscopy. *Archives of Biochemistry and Biophysics*, 1997. 340(2): p. 159-167.

[96] Burridge, K., et al., Focal Adhension-Transmambrance Junctions between the Extracellular Matrix and the Cytoskeleton. *Annual Reviews of Cell Biology*, 1988. 4: p. 487-525.

[97] Fischer, H., I. Polikarpov, and A. Craievish, Average Protein Density is a Molecular-Weight-Dependent Function. *Protein Science*, 2004. 13: p. 2825-2828.

[98] Wang, E. and D. Gundersen, Increased Organization of Cytoskeleton Accompanying the Aging of Human Fibroblasts in Vitro. *Experimental Cell Research*, 1984. 154: p. 191-202.

[99] Nishio, K., et al., Senescence and Cytoskeleton: Overproduction of Vimentin Induces Senescent-like Morphology in Human Fibroblasts. *Histochemistry and Cell Biology*, 2001. 116: p. 321-327.

[100] Nishio, K. and A. Inoue, Senescence-Associated Alterations of Cytoskeleton: Extraordinary Production of Vimentin that Anchors Cytoplasmic P53 in Senescent Human Fibroblasts. *Histochemistry and Cell Biology*, 2005. 123: p. 263-273.

[101] Schulze, C., et al., Stiffening of Human Skin Fibroblasts with Aging. *Biophysical Journal*, 2010. 99: p. 2434-2442.

[102] Park, S., et al., Cell Motility and Local Viscoelasticity of Fibroblasts. *Biophysical Journal*, 2005. 89(6): p. 4330-4342.

[103] Bicknese, S., et al., Cytoplasmic Viscosity Near the Cell Plasma Membrance-Measurement by Evanescent Field Frequency-Domain Microfluorimetry. *Biophysical Journal*, 1993. 65: p. 1272-1282.

[104] Michelson, A.D., *Platelets*. 2002: Elsevier.

[105] Semple, J.W., J.E.I. Jr, and J. Freedman, Platelets and the Immune Continuum. *Nature Reviews*, 2011. 11: p. 264-274.

[106] Osemene, N.I., The Pharmacist's Role in Antiplatelet Therapy. *U.S. Pharmacist*, 2012. 37(2): p. 32-39.

[107] Foster, T.E., et al., Platelet-Rich Plasma: From Basic Science to Clinical Applications. *The American Journal of Sports Medicine*, 2009. 37(11): p. 2259-2272.

[108] Everts, P.A.M., et al., Platelet Rich Plasma and Platelet Gel: A Review. *The Journal of Extra-corporeal Technology*, 2006. 38(2): p. 174-187.

[109] Nikolidakis, D. and J.A. Jansen, The Biology of Platelet-Rich Plasma and Its Application in Oral Surgery: Literature Review. *Tissue Engineering: Part B*, 2008. 14(3): p. 249-258.

[110] Alsousou, J., et al., The Biology of Platelet-Rich Plasma and its Application in Trauma and Orthopaedic Surgery. *Journal of Bone and Joint Surgery*, 2009. 91-B(8): p. 987-996.

[111] Cazenave, J.-P., et al., Preparation of Washed Platelet Suspensions from Human and Rodent Blood. *Platelets and Megakaryocytes Methods in Molecular Biology*, 2004. 272: p. 13-28.

[112] Radmacher, M., et al., Measuring the Viscoelastic Properties of Human Platelets with the Atomic Force Microscope. *Biophysical Journal*, 1996. 70: p. 556-567.

[113] Ploehn, H.J. and C. Liu, Quantitative Analysis of Montmorillonite Platelet Size by Atomic Force Microscopy. *Industrial and Engineering Chemistry Research*, 2006. 45: p. 7025-7034.

[114] Hansson, K.M., et al., Surface Plasmon Resonance (SPR) Analysis of Coagulation in Whole Blood with Application in Prothrombin Time Assay. *Biosensors and Bioelectronics*, 1999. 14: p. 671-682.

[115] Hansson, K.M., et al., Surface Plasmon Resonance Detection of Blood Coagulation and Platelet Adhesion under Venous and Arterial Shear Conditions. *Biosensors and Bioelectronics*, 2007. 23: p. 261-268.

[116] Vikinge, T.P., et al., Comparison of Surface Plasmon Resonance and Quartz Crystal Microbalance in the Study of Whole Blood and Plasma Coagulation. *Biosensors and Bioelectronics*, 2000. 15: p. 605-613.

[117] Weber, N., H.P. Wendel, and J. Kohn, Formation of Viscoelastic Protein Layers on Polymeric Surface Relevant to Platelet Adhesion. *Journal of Biomedical Materials Research*, 2005. 72A(4): p. 420-427.

[118] Sinn, S., et al., Platelet Aggregation Monitoring with a Newly Developed Quartz Crystal Microbalance System as an Alternative to Optical Platelet Aggregometry. *Analyst*, 2010. 135: p. 2930-2938.

[119] Li, R. and Y. Sun, Surface Modification of Poly (styrene-b-(ethylene-co-butylene)-b-styrene) Elastomer and its Plasma Protein Adsorption by QCM-D. *Applied Surface Science*, 2014. 301: p. 300-306.

[120] Fatisson, J., Y. Merhi, and M. Tabrizian, Quantifying Blood Platelet Morphological Changes by Dissipation Factor Monitoring in Multilayer Shells. *Langmuir*, 2008. 24: p. 3294-3299.

[121] Fatisson, J., et al., Determination of Surface-Induced Platelet Activation by Applying Time-Dependency Dissipation Factor Versus Frequency Using Quartz Crystal Microbalance with Dissipation. *Interface*, 2011. 8: p. 988-997.

[122] Lord, M.S., et al., The Modulation of Platelet Adhesion and Activation by Chitosan through Plasma and Extracellular Matrix Proteins. *Biomaterials*, 2011. 32: p. 6655-6662.

[123] Kunze, A., C. Hesse, and S. Svedhem, Real-Time Monitoring of Surface-Confined Platelet Activation on TiO2. *Colloids and Surface B: Biointerfaces*, 2014. 116: p. 446-451.

[124] Savage, B., E. Saldivar, and Z.M. Ruggeri, Initiation of Platelet Adhesion by Arrest onto Fibrinogen or Translocation on von Willebrand Factor. *Cell*, 1996. 84: p. 289-297.

[125] Shattil, S.J., H. Kashiwagi, and N. Pampori, Integrin Signaling: The Platelet Paradigm. *Blood*, 1998. 91: p. 2645-2657.

[126] Wu, H., et al., Aging-Related Viscoelasticity Variation of Tendon Stem Cells (TSC) Characterized by Quartz Thickness Shear Mode (TSM) Resonators. *Sensors and Actuators B*, 2015. 210: p. 369-380.

[127] Bender, F., et al., On-Line Monitoring of Polymer Deposition for Tailoring the Waveguide Characteristics of Love-Wave Biosensors. *Langmuir*, 2004. 20: p. 2315-2319.

[128] Martin, S.J., et al., Characterization of SH Acoustic Plate Mode Liquid Sensors. *Sensors and Actuators A*, 1989. 20: p. 253-268.

[129] Jakoby, B. and M.J. Vellekoop, Viscosity Sensing Using a Love-Wave Device. *Sensors and Actuators A*, 1998. 68: p. 275-281.

[130] Herrmann, F., D. Hahn, and S. Buttgenbach, Seperate Determination of Liquid Density and Viscosity with Sagittally Corrugated Love-Mode Sensors. *Sensors and Actuators A*, 1999. 78: p. 99-107.

[131] Wang, Z., J.D.N. Cheeke, and C.K. Jen, Sensitivity Analysis for Love Mode Acoustic Gravimetric Sensors. *Applied Physics Letters*, 1994. 64: p. 2940-2942.

[132] Du, J., et al., A Study of Love-Wave Acoustic Sensors. *Sensors and Actuators A*, 1996. 56: p. 211-219.

[133] Kielczynski, P., Attenuation of Love Waves in Low-Loss. *Journal of Applied Physics*, 1997. 82(12): p. 5932-5937.

[134] McHale, G., M.I. Newton, and F. Martin, Theoretical Mass Sensitivity of Love Wave and Layer Guided Acoustic Plate Mode Sensors. *Journal of Applied Physics*, 2002. 91(12): p. 9701-9710.

[135] McHale, G., M.l. Newton, and F. Martin, Theoretical Mass, Liquid, and Polymer Sensitivity of Acoustic Wave Sensors with Viscoelastic Guiding Layers. *Journal of Applied Physics*, 2003. 93(1): p. 675-690.

[136] Zhang, X., et al., A Novel Sensitive Cell-Based Love Wave Biosensor for Marine Toxin Detection. *Biosensors and Bioelectronics*, 2016. 77: p. 573-579.

[137] Adler, E.L., SAW and Pseudo-SAW Properties Using Matrixs Methods. *IEEE Transactions on Ultrasonics, Ferroelectrics, and Frequency Control*, 1994. 41(6): p. 876-882.

[138] Teles, F.R.R. and L.P. Fonseca, Trends in DNA Biosensors. *Talanta*, 2008. 77: p. 606-623.

[139] Thompson, M., et al., Thickness-Shear-Mode Acoustic Wave Sensors in the Liquid Phase: A Review. *Analyst*, 1991. 116: p. 881-890.

[140] Lange, K., et al., A Surface Acoustic Wave Biosensor Concept with Low Flow Cell Volumes for Label-Free Detection. *Analytica Chemistry*, 2003. 75: p. 5561-5566.

[141] Liu, Q., et al., Cell-Based Biosensors and Their Application in Biomedicine. *Chemical Reviews*, 2014. 114: p. 6423-6461.

[142] Josse, F., F. Bender, and R.W. Cemosek, Guided Shear Horizontal Surface Acoustic Wave Sensors for Chemical and Biochemical Detection in Liquids. *Analytical Chemistry*, 2001. 73: p. 5937-5944.

[143] Hillman, A.R., A. Jackson, and S.J. Martin, The Problem of Uniqueness of Fit for Viscoelastic Films on Thickness-Shear Mode Resonator Surfaces. *Analytical Chemistry*, 2001. 73(3): p. 540-549.

[144] Hillman, A.R., I. Efimov, and K.S. Ryder, Time-Scale- and Temperature-Dependent Mechanical Properties of Viscoelastic Poly(3,4-ethylenedioxythiophene). *Journal of American Chemistry Society*, 2005. 127: p. 16611-16620.

[145] Skivesen, N., A. Tetu, and M. Kristensen, Photonic-Crystal Waveguide Biosensor. *Optics Express*, 2007. 15(6): p. 3169-3176.

[146] Lee, M. and P.M. Fauchet, Two-Dimensional Silicon Photonic Crystal Based Biosensing Platform for Protein Detection. *Optics Express*, 2007. 15(8): p. 4530-4535.

[147] Lucklum, R. and J. Li, Phononic Crystals for Liquid Sensor Applications. *Measurement Science and Technology*, 2009. 20: p. 124014-1-12.

[148] Olsson, R.H. and I. El-Kady, Microfabricated Phononic Crystal Devices and Applications. *Measurement Science and Technology*, 2009. 20: p. 012002-1-13.

[149] Hou, Z. and B.M. Assouar, Numerical Investigation of the Propagation of Elastic Wave Modes in a One-Dimensional Phononic Crystal Plate Coated on a Uniform Substrate. *Journal of Physics D: Applied Physics*, 2009. 42: p. 085103.

[150] Espinosa, F.R.M.d., E. Jimenez, and M. Torres, Ultrasonic Band Gap in a Periodic Two-Dimensional Composite. *Physical Review Letters*, 1998. 80(6): p. 1208-1211.

[151] Sanchez-Perez, J.V., et al., Sound Attenuation by a Two-Dimensional Array of Rigid Cylinders. *Physical Review Letters*, 1998. 80(24): p. 5325-5328.

[152] Liu, Z., et al., Locally Resonant Sonic Materials. *Science*, 2000. 289: p. 1734-1736.

[153] Sigalas, M.M. and N. Garcia, Theoretical Study of Three Dimensional Elastic Band Gaps with the Finite-Difference Time-Domain Method. *Journal of Applied Physics*, 2000. 87: p. 3122-3125.

[154] Wu, F., et al., Point Defect States in Two-Dimensional Phononic Crystals. *Physics Letters A*, 2001. 292: p. 198-202.

[155] Zhao, D., et al., Peculiar Transmission Property of Acoustic Waves in a One-Dimensional Layered Phononic Crystal. *Physica B*, 2007. 390: p. 159-166.

[156] Tanaka, Y., T. Yano, and S. Tamura, Surface Gudied Waves in Two-Dimensional Phononic Crystals. *Wave Motion*, 2007. 44: p. 501-512.

[157] Miyashita, T., Sonic Crystal and Sonic Wave-Guides. *Measurement Science and Technology*, 2005. 16: p. 47-63.

[158] Vasseur, J.O., et al., Waveguiding in Two-Dimensional Piezoelectric Phononic Crystal Plates. *Journal of Applied Physics*, 2007. 101: p. 114904-1-6.

[159] Zubtsov, M. and R. Lucklum, A Novel Method for Tuning the Band Gap Structure of 2D Phononic Crystals. *IEEE International Ultrasonics Symposium Proceedings*, 2010: p. 515-518.

[160] Ke, M., M. Zubtsov, and R. Lucklum, Sub-Wavelength Phononic Crystal Liquid Sensor. *Journal of Applied Physics*, 2011. 110: p. 026101-1-3.

[161] Lucklum, R., M. Ke, and M. Zubtsov, Two-Dimensional Phononic Crystal Sensor Based on a Cavity Mode. *Sensors and Actuators B*, 2012. 171-172: p. 271-277.

[162] Zubtsov, M., et al., 2D Phononic Crystal Sensor with Normal Incidence of Sound. *Sensors and Actuators A*, 2012. 186: p. 118-124.

[163] Lucklum, R., Phononic Crystal Sensor. *IEEE International Frequency Control Symposium Proceedings*, 2008: p. 85-90.

[164] Liu, T.-W., et al., Evidence of a Love Wave Bandgap in a Quartz Substrate Coated with a Phononic Thin Layer. *Applied Physics Letters*, 2014. 104: p. 181905.

[165] Li, S., et al., Achieving Lower Insertion Loss and Higher Sensitivity in a SAW Biosensor via Optimization of Waveguide and Microcavity Structures. *IEEE Sensors Journal*, 2017. 17(6): p. 1608-1616.

[166] Cular, S., S.K.R.S. Sankaranaraynana, and V.R. Bhethanabotla, Enhancing Effects of Microcavities on Shear-Horizontal Surface Acoustic Wave Sensors: A Finite Element Simulation Analysis. *Applied Physics Letters*, 2008. 92: p. 244104.